EFFECTS OF SURFACE CHEMISTRY AND SURFACE TOPOGRAPHY ON POLYETHER-ETHER-KETONE OSSEOINTEGRATION

A Dissertation
Presented to
The Academic Faculty

by

F. Brennan Torstrick

In Partial Fulfillment
of the Requirements for the Degree
Doctor of Philosophy in the
George W. Woodruff School of Mechanical Engineering

Georgia Institute of Technology
December 2017

EFFECTS OF SURFACE CHEMISTRY AND SURFACE TOPOGRAPHY ON POLYETHER-ETHER-KETONE OSSEOINTEGRATION

Approved by:

Dr. Robert Guldberg, PhD, Advisor
School of Mechanical Engineering
Georgia Institute of Technology

Dr. William Murphy, PhD
School of Biomedical Engineering
University of Wisconsin

Dr. Ken Gall, PhD
School of Mechanical Engineering & Materials Science
Duke University

Dr. Scott Boden, MD
School of Medicine
Emory University

Dr. Andrés García, PhD
School of Mechanical Engineering
Georgia Institute of Technology

Date Approved: November 10, 2017

ACKNOWLEDGEMENTS

I consider myself incredibly lucky to have stumbled into such a unique and gratifying graduate experience and I have many people to thank for helping me along the way.

First and foremost, I must thank my advisors, Bob Guldberg and Ken Gall. Without them, none of this work would have happened. I feel priviledged that they gave me the freedom and encouragement to explore new ideas and be independent, while also providing overall direction and critical insight to the project as a whole. The practical and translational mindset of Bob and Ken was also a large part of what attracted me to work with them when I first came to Georgia Tech. Having an end application in mind while conducting these studies was a great motivator. I also must thank my thesis committee – Scott Boden, Andrés García, and Bill Murphy. Each brought a unique perspective to the project and I sincerely thank them for volunteering their time to help.

Much of this work was done alongside my colleague, Nathan Evans. Through our lab work, conference trips and our time in the TI:GER program, Nathan was always a source of encouragement. He was always willing to volunteer his time to help and I particularly enjoyed our conversations speculating on what crazy idea to try next. Alongside Nathan, I want to also thank the rest of our TI:GER team: Anne Hewitt, Matt Kroge and Brad Schweizer. We had a great team and I thoroughly enoyed all of the time we spent together going to business plan competitions and delving into the entrepreneurial facets of my research project.

I also want to thank everyone in the Guldberg lab. Everyone has such a diverse skill set that someone was bound to know the answer to any questions that I had. Getting through surgeries would also not have been possible without everyone joining in to help. Thank you in particular to Angela Lin, Laxmi Krishnan, and Nick Willett for dedicating your time to helping me get up to speed on surgical techniques along with general advice and guidance. Of course, everyone knows the lab would have burned down in an instant without Hazel Stevens. I want to thank her in particular for all of her help walking me through various cell culture techniques.

Many thanks also go to everyone at Vertera and MedShape. To Allen Chang, Stephen Laffoon, Mateo Garcia, Ken Dupont, and the rest of the engineering and R&D teams at both companies for putting up with my endless questions and always being willing to go out of their way to show me just enough of how to do something to not kill myself, and then letting me figure out the rest. Who knows how many tools I've broken or parts I've ruined, but those are where I've learned the most. Thanks to Tim Nash for showing me where the rubber meets the road with this project. He probably doesn't think it, but his tidbits of information every now and then combined with his crash course in spine surgery went a long way for me to be able to realize the impact of the work that I was doing. And also a special thank you to Chris Lee. He was always there to provide critical insight into study design and helped troubleshoot when things went awry. Chris provided a constant reminder that my work meant something and always helped me see the forest from the trees. Last but not least, Dave Safranski was also always there to help troubleshoot and brainstorm crazy ideas, for which I am very thankful. He always made sure that I was thinking critically about what I was doing and made sure that I was proving it.

And finally, thank you to my family, especially my mother, father, and brother, for always supporting me through this time and providing a place to escape to every now and then to take my mind off of things. I could not have done this without them.

TABLE OF CONTENTS

LIST OF TABLES

LIST OF FIGURES

LIST OF SYMBOLS AND ABBREVIATIONS

2D	Two-dimensional
3D	Three-dimensional
ACDF	Anterior Cervical Fusion and Discectomy
AFM	Atomic Force Microscopy
A_{LB}	Load-bearing area
ALD	Atomic Layer Deposition
ALP	Alkaline Phosphatase
ANOVA	Analysis of Variance
A-P	Anterior-Posterior
APORE	Pore area
ASTM	American Society for Testing and Materials
AT	Total Area
BIC	Bone-implant Contact
BMI	Body Mass Index
BV	Bone Volume
CI	Confidence Interval
CT	Computed tomography
DBM	Demineralized bone matrix
DNA	Deoxyribonucelic Acid
EDS	Energy-dispersive X-ray Spectroscopy
EdU	5-ethynyl-2'-deoxyuridine
ELISA	Enzyme linked Immunosorbent Assay

EMG	Electromyelogram
FBS	Fetal Bovine Serum
FDA	Food and Drug Administration
GPC	Gel Permeation Chromotography
HA	Hydroxyapatite
HEK	Human Embryonic Kidney Cells
HCUP	Healthcare Cost and Utilization Project
hMSC	Human Mesenchymal Stem Cells
hOB	Human Osteoblasts
IACUC	Institutional Animal Care and Use Committee
IBD	Interbody Fusion Device
MCL	Medical Collateral Ligament
MMA	Methyl Methacrylate
M_n	Number Average Molecular Weight
M_w	Weight Average Molecular Weight
PBS	Phosphate Buffered Saline
PDI	Polydispersity Index
PEEK	Polyether-ether-ketone
PEEK-BP	Bulk Porous PEEK
PEEK-IM	Injection Molded PEEK
PEEK-SP	Surface Porous PEEK
PMMA	Polymethylmethacrylate
pNPP	p-nitrophenylphosphate
PSL	Penicillin / Streptomycin / L-glutamate
SD	Standard Deviation

SE	Standard Error
S_a	Average surface roughness
SEM	Scanning Electron Microscopy
S_z	Max Peak-to-Valley Height
TCPS	Tissue Culture Polystyrene
T_m	Melting Temperature
T_V	Total Volume
VEGF	Vascular Endothelial Growth Factor
XPS	X-ray Photoelectron Spectroscopy
α-MEM	Alpha Minimum Essential Media
λ_c	Cutoff wavelength
µCT	Micro-computed Tomography
σ_N	Fatigue strength
σ_{UTS}	Ultimate Tensile Strength

SUMMARY

Orthopaedic injuries and disorders affect millions of people each year and often require surgical intervention using medical devices. Spinal fusion ranks as the third most common orthopaedic procedure with approximately 500,000 performed each year. Despite the high number and cost of these procedures, it is estimated that 5 – 20% of fusions experience surgical complication or must undergo revision. Many complications can be traced back to inadequate osseointegration of an implanted device. Interbody fusion devices (IBDs) are often used to maintain vertebral spacing and stabilize the spinal segment during fusion, but poor osseointegration and fixation can lead to fibrous encapsulation and migration of the device, causing pain and inhibiting fusion. Therefore, development of new materials-based strategies to enhance osseointegration and device fixation is a promising approach to improve spinal fusion outcomes.

The primary goal of this work was to improve the osseointegration of a commonly used IBD material, polyether-ether-ketone (PEEK), by modifying its surface to be porous. Conventional PEEK devices exhibit limited osseointegration, which is often attributed to PEEK's hydrophobic and chemically inert surface chemistry. However, the smooth surface of conventional PEEK surfaces also prevents osseointegration and fixation by limiting mechanical interlock with apposing bone. Indeed, rough and porous surfaces on non-PEEK devices, such as titanium, demonstrate greatly enhanced osseointegration compared to their smooth counterparts. Although this dependence on surface topography has been described for decades, the development of porous structures from PEEK that maintain sufficient mechanical properties for load-bearing applications has been limited.

This thesis introduced a new porous PEEK material for load-bearing orthopaedic applications and investigated how surface topography and surface chemistry influenced its osseointegration. Herein, we deomnstrate porous PEEK enhanced osseointegration relative to smooth and rough surfaces made from PEEK or titanium. Systematic investigation into the relative influence of surface topography and surface chemistry using nano-scale titanium coatings demonstrated that osseointegration was greatest for porous surfaces regardless of whether they possessed a PEEK or titanium surface chemistry. However, surface chemistry was shown to influence osseointegration of smooth and rough surfaces. These results could provide valuable insight for the development of more effective devices for spinal fusions and other orthopaedic applications.

CHAPTER 1. INTRODUCTION

Half of a million spinal fusion surgeries are performed each year in the U.S. to relieve back pain caused by a diseased intervertebral disc or other spinal deformity. These procedures help stabilize the spine and replace the diseased disc with rigid spacers, commonly called cages, to facilitate bony fusion across the disc space, thereby preserving disc height, reducing motion and relieving pain. Nearly half of all cages used today are made of a polymer called polyether-ether-ketone (PEEK). Developed in the late 1990's, PEEK cages gained popularity due to their high strength, imaging compatibility and biocompatibility in osseous environments. Although procedures utilizing PEEK cages remain largely successful, several recent reports have challenged PEEK's ability to effectively integrate with bone, arguing instead that PEEK's hydrophobic surface promotes fibrous encapsulation and implant migration. In response, several clinicians have turned towards more traditional titanium cages, allograft bone, or one of several surface coating technologies that have been developed to improve PEEK integration. However, each of these alternatives possesses its own disadvantages, leaving surgeons with no ideal implant and forcing them to choose between poor titanium medical imaging, inadequate allograft strength, PEEK coating instability, or poor PEEK osseointegration. Despite great interest in recent spinal fusion technologies, the reasons behind the poor osseointegration of regular PEEK cages remain poorly understood. This work seeks to better understand and overcome the limitations of PEEK by investigating bone's response to various surface states of PEEK implants.

It is well known that roughened and porous surface topographies can enhance osseointegration of titanium and other metallic orthopaedic implants. However, nearly all PEEK implants used today possess a smooth surface finish, which leads one to ask 1.) Could an altered surface topography overcome PEEK's poor osseointegration? or 2.) Is PEEK's surface chemistry an inherent limitation to implant fixation? The following studies will probe PEEK's surface topography and surface chemistry to investigate factors influencing PEEK implant osseointegration.

AIM 1: Investigate the osseous response to porous PEEK

In contrast to current smooth PEEK implants, our group developed porous PEEK implants with promising mechanical properties for the high load bearing environment of the spine. However, investigation of the osseointegration and fixation of porous PEEK implants had not been conducted. The primary goal of this aim was to investigate the *in vitro* and *in vivo* osseous response to porous PEEK implants compared to smooth PEEK. *In vitro* studies were conducted using a standard pre-osteoblast differentiation cell culture model and *in vivo* studies were conducted using a femoral segmental defect model and tibial metaphysis implant model in the rat. Biomechanical testing, μCT and histology were used to evaluate the bone implant interface over 4 – 12 weeks.

AIM 2: Compare osseointegration of porous PEEK to a clinically relevant alternative PEEK technology

Following baseline characterization of the osseous response to porous PEEK, it was of interest to compare porous PEEK to another surface technology designed to overcome the poor osseointegration of smooth PEEK implants. To this end plasma-sprayed titanium

coatings on PEEK were selected as a comparative group based on their widespread clinical use and favorable reported osseointegration. The stark differences between the macro-porous PEEK and micro-rough titanium surfaces also provided a unique opportunity to begin probing the effects of surface topography and surface chemistry on osseointegration. *In vitro* and *in vivo* evaluation of these surfaces in comparison to smooth PEEK controls were conducted in much the same manner as Aim 1.

AIM 3: Examine the role of multi-scale topographies and surface composition on PEEK osseointegration

Results from Aim 1 and Aim 2 in conjunction with other reports from the literature suggest that porous PEEK can enhance osseointegration despite possessing a predominantly normal PEEK surface chemistry. The goal of this aim was to independently vary surface topography and chemistry to evaluate the relative effect of each on PEEK implant osseointegration. The central hypothesis of this aim was that surface topography would influence PEEK implant osseointegration to a greater extent than surface chemistry. To modify topography, PEEK was roughened by grit blasting or made porous as in Aim 1 and Aim 2. Samples either retained their PEEK chemistry or were coated with a 30 - 50 nm layer of TiO_2 using Atomic Layer Deposition (ALD). Known for their thinness and uniformity, ALD coatings presented a suitable method to alter PEEK chemistry while minimizing topographical changes to the surface. Independent modification of PEEK topography and chemistry was important to limit confounding effects described in similar studies throughout the literature. TiO_2 was used due to its widespread clinical use on the surface of all titanium implants. Surface topography was characterized at the nano-, micro- and macro- scale using atomic force microscopy (AFM), confocal laser microscopy,

scanning electron microscopy (SEM) and microcomputed tomography (μCT). Surface chemistry was characterized using x-ray photoelectron spectroscopy (XPS) and energy dispersive x-ray spectroscopy (EDS). Osseointegration of each surface was evaluated using the same tibial implant model as in Aim 2.

CHAPTER 2. BACKGROUND

2.1 Spinal Fusion Epidemiology and Economic Impact

Orthopaedic injuries and disorders affect millions of people each year and often require surgical intervention. The three most common orthopaedic procedures for the past two decades have been hip and knee arthroplasty followed by spinal fusion at nearly 500,000 procedures in 2013 [1, 2]). The number and cost of most orthopaedic procedures has steadily increased each year, yet spinal fusion has recently grown exponentially to be the one of the most expensive surgeries in the U.S. overall at $105,184 in hospital charges per procedure. In total, spinal fusion surgery costs the healthcare system $42.8B dollars each year (Figure 2.1). Although the amount that hospitals charge is typically greater than the actual amount paid, the general trends are expected to be similar. Considering the great number and cost of spinal fusion procedures, it is imperative to develop effective treatment strategies to benefit patients and improve surgical outcomes.

The rationale behind spinal fusion surgery is to utilize neural decompression and arthrodesis to eliminate back pain and vertebral segment motion associated with spinal degeneration, deformity and trauma [3, 4]. Fusion is often achieved through posterior fixation of the spine with pedicle screws and stabilizing rods, followed by insertion of an interbody device to provide anterior support and facilitate fusion across the interbody space [4]. First investigated in the late 1950's [5], spinal fusion using an interbody device (IBD, or more commonly 'cage') has become routine and represents a total implant market size of $4.5B (U.S. 2012) [6]. Increased fusion cage utilization has been attributed to improved

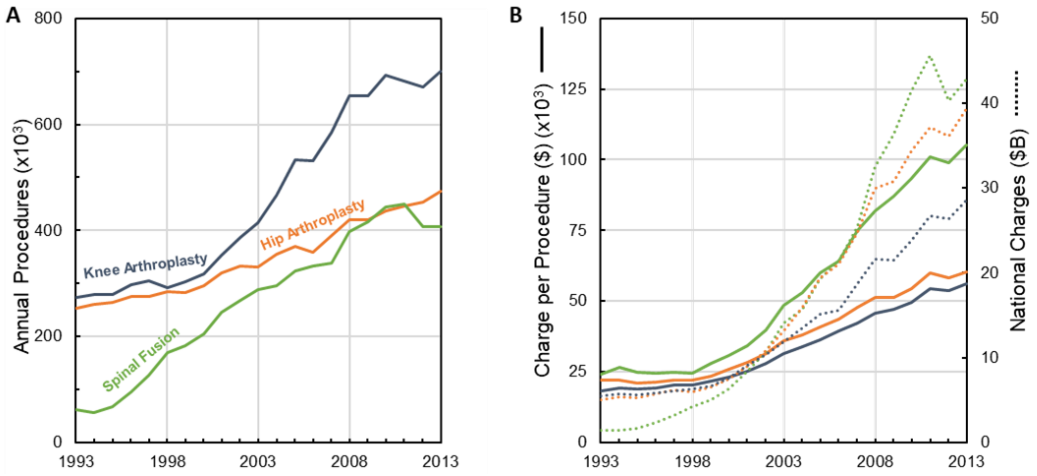

Figure 2.1 - Epidemiology and economics of common orthopaedic procedures. (A) Number of annual procedures and (B) average hospital charges (solid lines) and cumulative national charges (dotted lines) for the three most common orthopaedic procedures in the U.S. (Data taken from the HCUP database.)

diagnostic techniques, increased life expectancy, prevalence of obesity and increased implant availability following their FDA approval in 1996 [2, 3].

2.2 Spinal Fusion Outcomes

Despite their widespread use, spinal fusions often result in clinical failure. Outcomes vary greatly depending on the level of the spine, with cervical fusions in the neck typically being more successful than lumbar fusions of the lower back. Approximately 95% of cervical fusion patients have good to excellent results, perhaps due to low loading levels in the cervical spine [7]. In contrast, between 30% and 50% of lumbar fusion patients experience the same or worse back pain two years after surgery [8]. Large population studies report surgical complication rates of 16-19% and revision rates of 12-18% for lumbar fusion cases, with smaller studies finding more variable rates [9-12]. For perspective, these lumbar fusion revision rates are higher than both hip and knee arthroplasty revision rates (8.1%

and 3.0%, respectively) [12]. Unfortunately, the likelihood of revision following lumbar fusion appears to be increasing with time. Patients in the late 1990's were 40% more likely to undergo revision following fusion compared to those in the early 1990's [13]. Whether or not this trend has continued in recent years remains to be determined. Nevertheless, such high complication and revision rates combined with increasing use of fusion techniques and a growing, aging population represent a substantial clinical and economic challenge. At these rates, approximately $5-7B is wasted annually revising failed fusion procedures. Development of more effective technologies that reduce the risk of revision could serve to alleviate these costs.

Spinal fusion procedures can be considered clinical failures for several different reasons including infection, nonunion, continued pain, and adjacent segment degeneration [14-16]. However, a large population study found that 42.1% of lumbar spine fusion failures are related to implanted devices [13]. Although this large figure is likely comprised of various devices and failure modes, two commonly reported failure mechanisms that are directly related to fusion cage design and composition are implant migration and subsidence. Implant migration occurs when the implant does not directly bond to the interfacing bone and can migrate within the disc space. Even minute micro-motion of the implant can induce fibrous encapsulation of the implant and prevent stable fixation within the disc [17]. At its worst, large scale implant migration may result in spinal cord impingement through posterior migration or expulsion out of the disc space altogether [18]. As a result, anterior plates are often used to prevent cage expulsion. Cage migration is reported to occur in up to 23% of fusion cases [18-20]. Implant subsidence occurs when the implant breaks through the vertebral endplates and extends into the vertebral trabecular

bone. Subsidence may result in increased pain and spinal misalignment; however, radiological evidence of subsidence does not always correlate with worsening symptoms. Placing the implant on denser bone (e.g. apophyseal ring) or using wider implants may provide more support and reduce subsidence. Subsidence rates range from 3-50% depending on cage design, spine region and surgical approach [21-24].

2.3 Biomaterials for Spinal Fusion Implants

Due to the influence of implant design and composition on the success of fusion procedures, interest has been placed on developing more effective cages that mitigate migration, subsidence and other implant-related complications. Multiple efforts have focused on overall implant design, featuring ridges, spikes or locking screws to prevent migration. However, more recent focus has shifted toward understanding how material composition and surface properties influence implant fixation and fusion.

Current fusion cages are primarily made from three different materials: allograft bone, titanium alloy and polyether-ether-ketone (PEEK). Other materials such as silicon nitride, stainless steel and carbon fiber are also used sparingly. Each implant material has its own advantages and disadvantages depending on diagnosis, patient demographic, surgical approach and surgeon preference.

Structural allograft bone constitutes approximately 35% of lumbar and 58% of cervical fusion cages [6]. Allograft cages demonstrate favorable bone integration and fusion; however, concerns exist surrounding disease transmission, immune rejection, availability, and strength in the case of lumbar applications. In addition to allograft, autograft bone from the iliac crest has also been used with favorable fusion outcomes, yet

donor site morbidity and tissue availability limit its use as a structural implant. Conversely, local autograft in morselized form is commonly packed within synthetic, non-bone cages to accelerate fusion.

Early synthetic fusion cages were predominantly made from titanium and its alloys (e.g. Ti6Al4V). First evaluated for dental applications, titanium's favorable osseointegration response has made it popular in spine and other orthopaedic device applications [25]. Additionally, titanium's strength far exceeds the rigorous loading requirements of the lumbar spine. However, titanium's high elastic modulus may alter the local loading environment and lead to stress shielding and corresponding bone resorption [26]. Further, titanium's high density creates medical imaging artifacts that interfere with a surgeon's ability to monitor patients' progress postoperatively. These concerns resulted in titanium cages comprising only 4-5% of all fusion cages in 2012 [6].

Most current synthetic cages are made from PEEK polymer, with higher frequencies seen in lumbar applications. First introduced in the 1990's, PEEK has gained widespread acceptance as a high-strength polymer in spine and other orthopaedic device applications due to its imaging characteristics, high strength, fatigue resistance and Young's modulus that is comparable to bone to reduce stress-shielding [27]. PEEK possesses adequate strength for high load-bearing applications and has a modulus that better matches bone to limit stress shielding. Further, PEEK does not create medical imaging artifacts and allows surgeons to visualize bone growth through and adjacent to implants during fusion. Though the mechanical and imaging properties of PEEK have contributed to its popular use, recent evidence has demonstrated that conventional smooth PEEK implants can exhibit poor osseointegration [27, 28] and fibrous encapsulation [29,

30]. As discussed above, lack of bone-implant contact can induce micromotion and inflammation that leads to fibrous layer thickening, osteolysis, and implant loosening [31-35]. Outcomes from previous studies support that these effects result from the implant surface being smooth because both smooth PEEK and smooth titanium exhibit similarly low bone fixation compared to rough and porous surfaces [36, 37]. However, PEEK's poor osseointegration is often, without direct evidence, "attributed" to other properties, such as its relatively inert and hydrophobic surface chemistry [37, 38]. As a result, multiple efforts have been made to modify PEEK's surface using plasma treatments, plasma-sprayed titanium coatings, and composites to improve PEEK implant integration. However, many of these surface technologies have exhibited only modest improvements in osseointegration and may suffer practical limitations to their clinical adoption such as delamination, instability, and mechanical property tradeoffs suggesting the need to develop alternative solutions [39-45].

2.4 Effects of surface topography and surface chemistry

Despite great interest in recent PEEK surface technologies, the reasons behind poor osseointegration of current PEEK cages remain poorly understood. Two surface characteristics thought to influence osseointegration most are chemistry and topography [46]. Other measurable surface characteristics, such as surface energy and surface charge, can often be related back to these two primary surface properties [47]. While PEEK's hydrophobic surface chemistry likely plays some role, extensive research on non-PEEK materials, particularly titanium, suggests that surface topography (or structure) would have a first-order impact on PEEK's ability to osseointegrate. Though compositionally different, research on titanium may inform analogous investigations on PEEK, which are sparse.

Surface structures on orthopaedic implants can largely be divided into two-dimensional (2D) textured surfaces and three-dimensional (3D) porous networks. Most 2D textured surfaces possess micro-scale roughness (S_a = 1-2 μm) that mimics osteoclast resorption pits, increases surface area for protein adsorption and cell adhesion, and is generally associated with a beneficial bone response [48, 49]. 2D textured surfaces possessing nano-scale features (1-100 nm) have also been investigated, though their effect on osseointegration is not as well understood [49-52], and other characteristics such as surface chemistry may have a stronger effect [53]. In contrast to 2D surfaces, 3D surfaces are typically characterized by an interconnected porous network (100-800 μm pores) to facilitate bone ingrowth and provide mechanical interlock at the bone-implant interface [54-56].

Although 2D and 3D surface structures have been shown to improve osseointegration when evaluated in isolation, recent studies have begun to investigate the combined effects of multi-scale surface features on cellular behavior and implant osseointegration. Such strategies are useful in determining the relative effects of surface features at each length scale. Notably, studies on titanium have reported that nano-scale surfaces contributed relatively little to bone cell behavior in the absence of larger micro-scale features [57, 58]. Similarly, micro-textured surfaces appear to contribute less to implant osseointegration compared to 3D macro-porosity [36, 59]. Altogether, the titanium surface literature suggests that 3D macro-scale porosity is the dominant surface structure influencing implant osseointegration.

Though the above conclusions are drawn from reports on titanium, we hypothesize that similar concepts hold true for PEEK. Initial reports from other research groups on bone

Table 2.1 - Development stages of porous PEEK in the literature

Source	Structural Characterization	Mechanical Testing	Cell Response	Animal Models	FDA Clearance	In Clinical Use
Edwards et al., 2012	●	●	●			
Zhao et al., 2013	●		●	●		
Landy et al., 2013	●	●	●			
Evans et al., 2015 Torstrick et al., 2016 Evans et al., 2016 Evans et al., 2017	●	●	●	●	●	●
Siddiq et al., 2015	●	●				
Roskies et al., 2016	●		●			

The Web of Science database was searched for "TITLE: ((porous OR scaffold OR three-dimensional OR 3D) AND (PEEK OR polyether ether ketone OR polyether-ether-ketone OR polyetheretherketone))" with no date restrictions on November 6, 2016. 40 results were found. 34 results were excluded based on: non-medical focus; theoretical models; porous PEEK composites; non-PEEK materials; and non-porous materials. 3 articles were added from the author's library.

ingrowth into porous PEEK implants have supported this view, yet these previous porous PEEK technologies had yet to reach clinical use and remained at various stages of development (Table 2.1) [38, 60-67].

Herein is described a new porous PEEK biomaterial with similar physical and mechanical properties of standard PEEK, making it a promising new candidate for spinal fusion and other load-bearing orthopaedic applications. The goal of the studies that follow was to characterize the osseointegration of this new porous PEEK material and help fill the literature gap concerning the effects of surface topography and surface chemistry on PEEK osseointegration. The results of this work have contributed to the successful clinical translation of this technology onto a spinal fusion device.

CHAPTER 3. HIGH STRENGTH, SURFACE POROUS POLYETHER-ETHER-KETONE FOR LOAD-BEARING ORTHOPAEDIC IMPLANTS[1]

3.1 Introduction

The ultimate goal of most medical implants is to restore impaired biological function and achieve functional integration with the body. Several porous polymers and other tissue engineered scaffolds have made advances in this regard for many soft tissue applications where mechanical loading is minimal [68]. However, similar solutions in high load-bearing orthopaedic environments remain elusive due to performance tradeoffs in clinically adopted biomaterials. Metallic implants provide high strength but are associated with medical imaging artifacts and unwanted bone resorption due to their high modulus and corresponding stress shielding [26]. Current porous polymer scaffolds can facilitate bony ingrowth but lack the strength necessary for high load-bearing environments experienced in clinical soft tissue reconstructions, spinal fusions, and arthrodesis applications [54, 69]. Bioresorbable polymers and composites facilitate osseointegration and implant resorption, but are clinically limited to soft tissue reconstructions and have cited incidences of prolonged inflammation, migration, incomplete degradation, and implant breakage [70].

[1] Modified from:

- N.T. Evans*, F.B. Torstrick*, C.S.D. Lee, K.M. Dupont, D.L. Safranski, W.A. Chang, A.E. Macedo, A.S.P. Lin, J.M. Boothby, D.C. Whittingslow, R.A. Carson, R.E. Guldberg, K. Gall, High-strength, surface-porous polyether-ether-ketone for load-bearing orthopedic implants, Acta Biomaterialia 13 (2015) 159-167.
- F.B. Torstrick, D.L. Safranski, J.K. Burkus, J.L. Chappuis, R.E. Guldberg, K.E. Smith, Getting PEEK to Stick to Bone: The Development of Porous PEEK for Interbody Fusion Devices, Tech Orthop 32(3) (2017) 158-166.

As a relatively new implant material, polyether-ether-ketone (PEEK) has gained widespread acceptance as a high-strength polymer used primarily in spinal fusions and soft tissue reconstructions, with favorable imaging compatibility and stiffness that closely matches bone [27, 71]. However, PEEK suffers a key property tradeoff in poor osseointegration. Its aromatic backbone and semi-crystalline nature provide high strength and biocompatibility, yet its hydrophobic and chemically inert surface limits local bone attachment [72, 73].

Basic research approaches to enhance PEEK osseointegration have focused both on surface modification and bulk porosity. Surface modifications such as plasma or chemical etching [40, 41, 44], addition of bioactive coatings [43, 74], and PEEK composites have performed well *in vitro* and *in vivo* [39], yet their clinical success may be limited due to their potential instability and delamination in physiological or surgical environments [75, 76]. Introducing bulk porosity throughout PEEK implants via powder sintering (or compression molding) aims to increase implant fixation by encouraging the migration and proliferation of various cell types to enhance vascular and bone tissue ingrowth [54, 55]. Indeed, porous PEEK implants have exhibited increased osseointegration [77]; however, they also suffered up to 86% reduction in strength due to the high overall fraction of porosity and the relatively weak local bonds created during powder sintering [54, 64, 78].

Limiting porosity to PEEK's surface could promote osseointegration and maintain bulk mechanical properties [78, 79]. Furthermore, a surface porosity approach is supported by the finding that a completely porous structure may not be required for functional integration [78, 79]. A porous surface layer could retain implant strength, provide an

adequate conduit for bone ingrowth, and avoid tissue necrosis common at the center of large fully porous implants in cases of limited vascular and nutrient supply [80, 81].

Here we investigate a novel method to create a functionally graded PEEK material with a balance between surface porosity for osseointegration and a solid core for mechanical load-bearing. Porous and solid regions are seamlessly connected, resulting in outstanding mechanical properties compared to powder sintering or coatings [54]. Samples are created using a patent-pending technique in which PEEK is extruded through sodium chloride crystals to create a surface porosity. The resulting structure and properties of the surface porous PEEK are discussed as well as preliminary *in vivo* results to provide initial insight into its potential to osseointegrate.

3.2 Materials and Methods

3.2.1 Sample Preparation

Surface porous PEEK (PEEK-SP) samples were created by extruding medical grade PEEK (Zeniva® 500, Solvay Advanced Polymers, T_m=340ºC) through the lattice spacing of sodium chloride crystals (Sigma Aldrich) under heat and pressure. After cooling, embedded sodium chloride crystals were leached in water leaving behind a porous surface layer. To control for pore size, sodium chloride was sieved into a range of 200-312 μm using #50 and #70 U.S. mesh sieves. Injection molded PEEK samples (PEEK) were used as smooth controls. Powder sintered bulk porous samples (PEEK-BP) were created using a compression molding technique [54]. Briefly, sodium chloride and PEEK powder (KetaSpire® KT-820FP, Solvay Advanced Polymers) were thoroughly mixed at a ratio to achieve equivalent pore size and porosity as PEEK-SP. Powder mixtures were sintered

under 260 MPa compression for 60 minutes at 363°C within a 10 mm diameter cylindrical mold (Heated Manual Press, Model 4386, Carver, Inc.). Sodium chloride was leached in water and sodium chloride removal was confirmed via microcomputed tomography (μCT). Poly(methyl methacrylate) (PMMA, McMaster-Carr), a polymer commonly used as bone cement in orthopaedic surgery, was used as a control for monotonic tension and tensile fatigue studies.

All tensile specimens were ASTM D638 Type I dog-bone samples. Shear samples were cut from PEEK bars to have a cross-sectional shear area of 16 x 16 mm for PEEK and PEEK-SP or 10 mm diameter for PEEK-BP. *In vitro* samples were 15 mm diameter x 2 mm disks that possessed either a porous PEEK or machined smooth PEEK surface. *In vivo* implants used in femoral defect studies were 5 mm diameter cylinders machined to a length of 8 mm from PEEK bars. One face was made surface porous while the other face was machined smooth as a control. A hole was bored through the center to replace the native medullary cavity. *In vivo* implants used in tibial implant studies were 3 mm diameter cylinders with the surface of interest on the bottom implant face.

3.2.2 Pore Layer Characterization

PEEK-SP samples were cut to size and the porous layers were scanned using μCT (μCT 50; Scanco Medical) at 10 μm voxel resolution with the scanner set at a voltage of 55 kVp and a current of 200 μA (n=15). Surface porous layers were manually contoured tightly to the pores to minimize inclusion of non-porous volume. A global threshold was applied to segment PEEK from pore space and kept consistent throughout all evaluations. Pore layer morphometrics were evaluated using direct distance transformation methods [82]. Briefly,

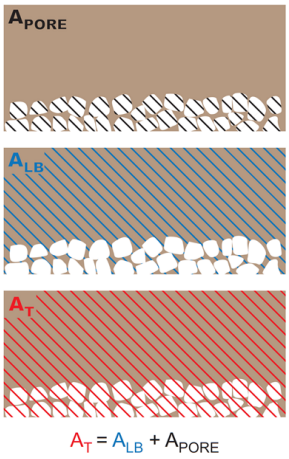

Figure 3.1 - Schematic of the PEEK-SP cross-sectional areas used in stress calculations. The processing increases cross-sectional areas due to the creation of pores. However, the load-bearing area, A_{LB}, is representative of the initial area of PEEK material, assuming volume conservation. The total area, A_T, is the sum of the load-bearing area and the area of the pore network, A_{PORE}

strut spacing was calculated using a maximal spheres method adapted from a trabecular spacing index. Porosity was determined by 1–BV/TV, where BV represented polymer volume and TV represented the total volume of the porous layer. Average pore layer thickness was determined using a trabecular thickness index algorithm on the filled TV of each porous layer. Pore layer interconnectivity was determined by inverting segmented pore and solid spaces and dividing the largest connected pore space volume by the total pore volume [83]. Scanning electron microscopy (SEM, Hitachi S-3700N VP-SEM) was utilized to observe the surface topography of PEEK-SP samples. Pore size was measured from SEM images as the length of the pore diagonal (n=50).

To detect changes in molecular weight due to PEEK-SP processing, gel permeation chromatography (GPC) was performed by Solvay Advanced Polymers on 100 mg samples of the isolated surface porous layer, solid core from a surface porous sample, and injection molded PEEK.

3.2.3 Monotonic and Fatigue Tensile Testing

Tensile tests were performed according to ASTM D638 at room temperature using a MTS Satec 20 kip (89 kN) servo-controlled, hydraulically-actuated test frame (n=5 PEEK-SP, n=5 PEEK, n=4 PMMA). The crosshead speed was 50 mm/min. Force-displacement data was used to calculate ultimate stress, elongation at break, and elastic modulus as well as generate the stress-strain curves.

Fatigue tests were run at increasingly lower stresses below the ultimate stress of the samples to generate S-N curves and determine the endurance limits of the respective samples. Fatigue tests were run on the same Satec test frame in axial stress control at a frequency of 1 Hz with a sinusoidal load. Tests were run until failure or runout. Runout was defined as greater than 1,000,000 cycles unless noted otherwise.

For monotonic and fatigue results, two representations of stress for PEEK-SP were calculated: the first using load-bearing area, A_{LB}, and the second using total area, A_T (Figure 3.1). Load-bearing area was taken as the cross sectional area of the as-received dog bone before porous processing. Total area was taken as the cross sectional area of the dog bone after porous processing. Use of total area produces stress values that assume void area contributes to load-bearing, and results will consequently depend on pore layer thickness and volume fraction of porosity. Conversely, load-bearing area includes only the cross-sectional area of polymer material, including solid polymer and porous strut regions, ignoring void area in the porous layer.

3.2.4 Aligned Interfacial Shear

Interfacial shear testing was adapted from ASTM F1044-05 using 3M™ Scotch-weld™ 2214 Non-Metallic Filled as adhesive and a 30 kN load cell (Instron). A thin layer of adhesive was applied evenly to the surfaces of shear samples and like faces were pressed together, clamped, and placed in a vacuum oven to cure at 121°C for 1 hour. The shear test fixtures were clamped in Instron jaws and adjusted to enable horizontal alignment of the shear sample. The plane of the adhesive was coincident with the axis of loading. Cured samples were placed into custom fixtures ensuring a tight clearance fit. The fixtures were pulled apart at 2.54 mm/min until the interfacial surfaces of the samples were completely sheared. The shear stress was calculated based on the measured failure load and cross-sectional area. Shear test groups included smooth PEEK (n=4), PEEK-SP (n=8) and PEEK-BP (n=5).

3.2.5 In vitro Cell Attachment and Mineralization

Clonal mouse pre-osteoblast cells (MC3T3-E1, ATCC) were seeded onto porous PEEK surfaces at 20,000 cell/cm^2 and cultured in growth media (α-MEM supplemented with 16.7% FBS and 1% Penicillin-Streptomycin-L-glutamine), refreshing media every 3 – 4 days. Live/dead staining was performed using calcein-AM and ethidium homodimer-1 (Invitrogen) on day 0 following cell attachment and on day 14. Stained cultures were imaged using confocal microscopy. *In vitro* mineralization was investigated using human mesenchymal stem cells (hMSC) culture in osteogenic media. At 4 weeks, cultures were stained using Alizarin Red.

3.2.6 Preliminary in vivo Animal Studies

Two established rat models were utilized to preliminarily assess the osseointegration potential of PEEK-SP compared to smooth PEEK surfaces. First, a femoral segmental defect model was chosen based on its previous use in characterizing bone ingrowth in porous polymeric and metallic implants [84-88]. All surgical procedures were approved by the Institutional Animal Care and Use Committee at the Georgia Institute of Technology (IACUC protocol #A11028). Briefly, bilateral 8 mm femoral defects were made in the central diaphyses of three 13-week old female Sasco Sprague-Dawley rats (Charles River), totaling six defects. Femurs were stabilized prior to defect creation using a modular plating system consisting of a polysulfone plate and two stainless steel risers. PEEK implants with one surface porous and one smooth end face were press-fit into each defect before incision closure (n=6). The orientations of surface porous faces were alternated between contralateral limbs. After surgery animals were allowed to recover and ambulate freely. Animals were injected with slow release buprenorphine at the time of surgery to relieve any pain. One animal was euthanized at 6 weeks and the remaining two were euthanized at 12 weeks.

The second preliminary *in vivo* study utilized an established implant plug model in the proximal rat tibia [89, 90]. All surgical procedures were approved by the Institutional Animal Care and Use Committee at the Georgia Institute of Technology (IACUC Protocol No. A16015). Porous PEEK and smooth PEEK cylinders (3 mm in diameter) were scanned prior to implantation using μCT to characterize the porous structure of each surface (n = 4 – 5). Male Sprague-Dawley rats (Charles River Laboratories International, Inc., Wilmington, MA) were anesthetized using isoflurane, administered analgesic via a

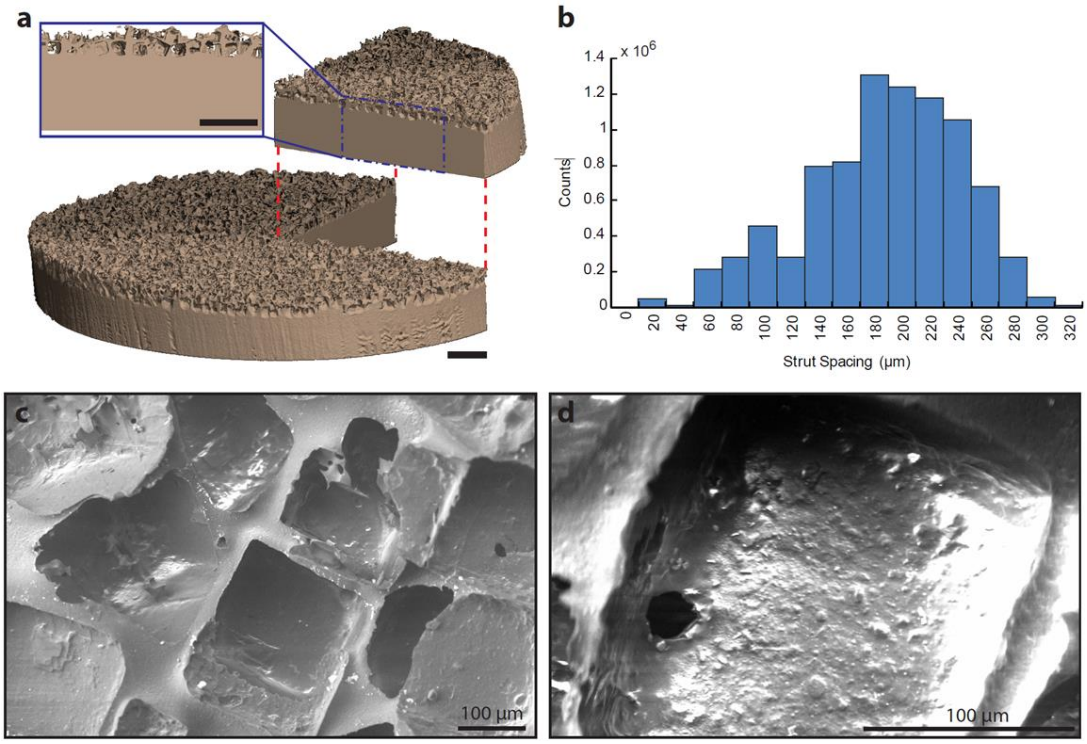

Figure 3.2 - Microstructural characterization of PEEK-SP: (a) µCT reconstruction of PEEK-SP structure showing representative pore layer cross-section. Note the cubic pore morphology due to cubic sodium chloride crystals. Scale bar is 1 mm. (b) Strut spacing histogram as characterized by micro-CT. (c,d) SEM micrographs of the PEEK-SP pore network. Images confirm cubic pore morphology and pore interconnectivity detected by µCT.

sub-cutaneous injection of sustained release Buprenorphine, and both hind limbs were shaved and prepared using alternating applications of chlorhexidine solution and isopropanol. A 1 cm incision was made over the medial aspect of the proximal tibia and muscle was released from the bone surface surrounding the growth plate and medial collateral ligament (MCL). The MCL was transected and a 2.5 mm biopsy punch (Integra® Miltex®, Plainsboro, NJ) was used to create a 2.7 mm diameter hole directly below the growth plate and in line with the native MCL path. Each implant was press-fit into the hole

Table 3.1 - Molecular weight distribution.

	M_n (g/mol)	M_w (g/mol)	PDI[d]
Porous[a]	44 753	100 032	2.24
Solid[b]	45 717	99 449	2.18
As-received[c]	46 208	98 846	2.14

[a] Porous region of PEEK-SP
[b] Solid region of PEEK-SP
[c] Injection molded PEEK without surface porous treatment
[d] Polydispersity index, PDI = M_w/M_n

such that the lip of the implant rested flush on the tibial cortex. Animals were euthanized at 8 weeks after surgery and explanted tibiae were frozen prior to further analysis.

3.2.7 Ex vivo µCT Imaging

Following euthanization, µCT scans were performed to assess bone ingrowth into each face of the implant. Femurs were scanned at 55 kVp and 145 µA with a 15 µm voxel size (Viva-CT, Scanco Medical). Tibiae were scanned at 55 kVp and 200 µA with a 17.2 µm voxel size (µCT50, Scanco Medical). Three-dimensional reconstructions were created from two-dimensional slices thresholded to include mineral densities >50% of native cortical bone. The volume of mineralized tissue within the tibial implants was divided by the pore volume for each implant to calculate percentage bone ingrowth.

3.2.8 Biomechanical Pullout Testing

Biomechanical pullout testing was performed to quantify functional osseointegration for each implant surface (n = 8). All pullout tests were conducted using a MTS 858 Mini Bionix II mechanical load frame (MTS Systems, Eden Prairie, MN, USA). Each thawed tibia was secured using a custom fixture and the implant was attached to a 100 N load cell by passing piano wire through the transverse hole of the implant and up to a clamp. Pre-

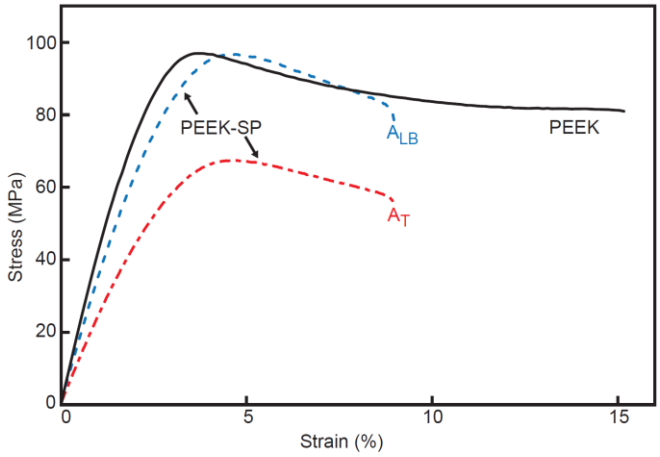

Figure 3.3 - Representative stress-strain curves of solid PEEK and PEEK-SP calculated using both A_{LB} and A_T.

loaded samples (1.0 N) were subjected to a constant tensile load rate of 0.2 mm/sec. The pullout force was the maximum load achieved before implant detachment or failure.

3.2.9 Histology

Femoral explants were fixed in formalin and stored in 70% ethanol until processing. Samples were processed through ascending grades of ethanol followed by xylene before embedding in methyl methacrylate. After embedding, rough sections were cut (Isomet® 1000 Precision Saw, Buehler) and then ground to 30 µm (EXAKT 400 CS). Sections were stained using a Goldner's Trichrome protocol to distinguish osteoid (red) from mineralized bone (green).

3.2.10 Statistical Analysis

Comparisons between the strength and modulus of PEEK-SP and solid PEEK were performed with a Student's t-test. Biomechanics comparisons between smooth PEEK and

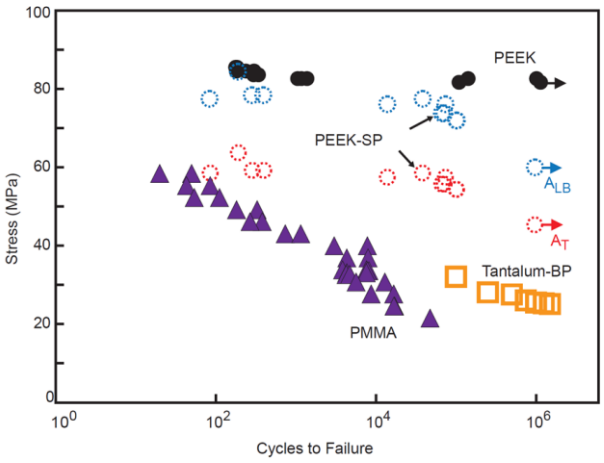

Figure 3.4 - S-N curve comparing the fatigue behavior of PEEK-SP using the load-bearing, A_{LB}, and the total area, A_T, to solid PEEK, PMMA, and bulk porous tantalum tested by Zardiackas et al., 2001. Arrows denote tests that were halted after reaching 106 cycles (solid PEEK, PEEK-SP), which is defined as the runout stress.

PEEK-SP were also conducted using a Student's t-test. The results of the interfacial shear test were analyzed using a one-way ANOVA and Tukey post-hoc analysis (95% confidence interval). All data is expressed as average ± standard deviation.

3.3 Results

3.3.1 Pore Layer Characterization

Pore morphology reliably correlated to sodium chloride crystal size (200 - 312 µm) and cubic nature with a pore size of 280±32 µm (Figure 3.2). The pore layer was 67.3±3.1% porous and highly interconnected (99.9±0.1%) with an average strut spacing of 186.8±55.5 µm as determined by µCT. Interconnectivity values are potentially skewed slightly higher than actual values due to spatial resolution imaging limitations that may have prevented detection of thin walls between pores. However, pore interconnectivity was expected to be high due to water's high degree of pore accessibility during leaching, as evidenced by the

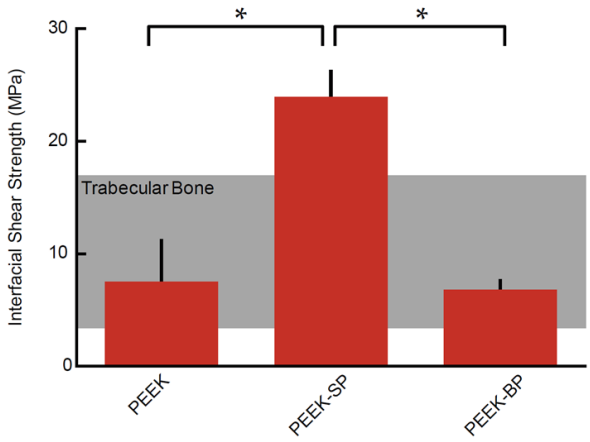

Figure 3.5 - Interfacial shear strength of PEEK-SP compared to smooth PEEK and sintered PEEK-BP with the shear strength of trabecular bone shown in the shaded region (Goldstein et al., 1987). Asterisks (*) indicate $p < 0.05$.

absence of residual sodium chloride on µCT. The average thickness of the pore layer was 399.6±63.3 µm.

Table 3.1 shows the molecular weight of the polymer from the surface porous region, a solid region from a surface porous sample, and injection molded PEEK. The

results demonstrate that the surface porous processing does not change the molecular weight of the samples.

3.3.2 Tensile Monotonic Testing

The creation of a surface porosity did not significantly decrease the strength of samples compared to injection molded controls when using A_{LB} ($p=0.52$). The ultimate tensile strength (σ_{UTS}) and elastic modulus of PEEK-SP samples were 96.11±2.61MPa and

3.36±0.30GPa compared to 97.7±1.0MPa and 3.34±0.14GPa for unprocessed solid PEEK

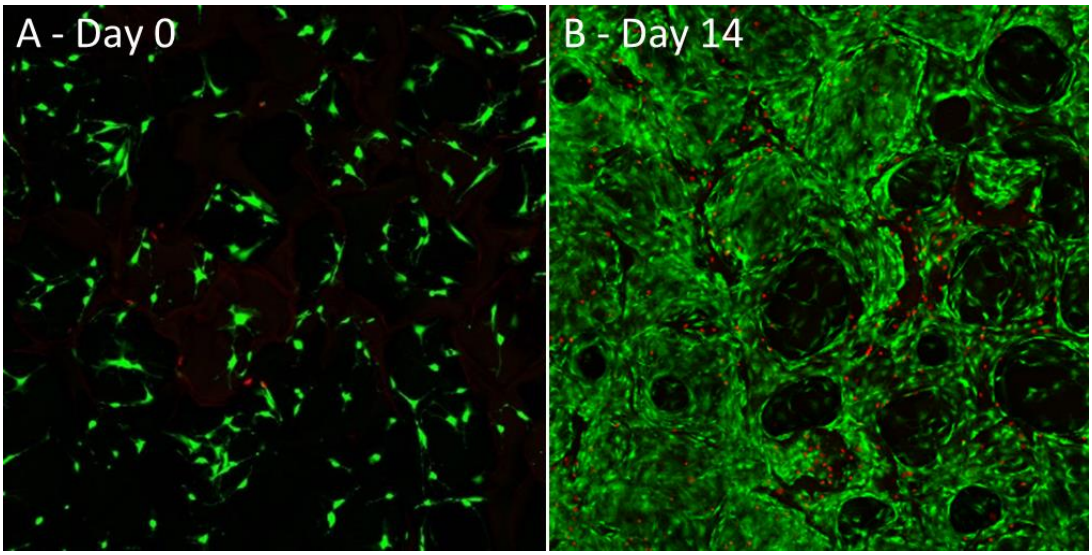

Figure 3.6 - Live/Dead confocal microscopy images of MC3T3 cultures grown on porous PEEK in growth media at (A) day 0 and (B) day 14. Live cells appear green and dead cell nuclei appear red.

controls, respectively, using A_{LB} (Figure 3.3). However, failure strains were decreased from 20.24±2.43 to 7.79±2.25. When the total area was used in stress calculations, PEEK-SP retained 73.9% of the strength and 73.4% of the elastic modulus of solid PEEK, corresponding to a tensile strength of 71.06±2.17MPa and modulus of 2.45±0.31GPa for a porous layer that comprises approximately 20% of the sample cross sectional area.

3.3.3 Tensile Fatigue Testing

PEEK-SP samples demonstrated high fatigue resistance regardless of which area was used in stress calculations (σ_N= 60.0 MPa for A_{LB} and σ_N = 45.3 MPa for A_T) (Figure 3.4). Further, the fatigue strength of PEEK-SP (A_{LB}) was 73% of the σ_{UTS} of smooth, injection-molded PEEK. Both PEEK and PEEK-SP experienced higher fatigue strength at similar cycle number than PMMA.

3.3.4 Aligned Interfacial Shear

The average shear strength of smooth PEEK, PEEK-SP, and PEEK-BP was 7.52±3.64, 23.96±2.26, and 6.81±0.81 MPa, respectively (Figure 3.5). Different shear failure modes were apparent for each group. Smooth PEEK failed at the glue layer interface, PEEK-SP failed within the porous network and within the solid region on the edges of some samples, and PEEK-BP failed in the empty bulk porous region behind the glue layer.

3.3.5 In vitro cell attachment and mineralization

Live/dead imaging of mouse pre-osteoblasts revealed cell attachment to the porous PEEK architecture at day 0 and thorough cell layer coverage of the pores by day 14, demonstrating favorable cell growth and proliferation on porous PEEK (Figure 3.6). hMSC cultures exhibited extensive mineralization as evidenced by Alizarin Red staining of porous PEEK cultures grown in osteogenic media for four weeks (Figure 3.7). Smooth PEEK cultures demonstrated less mineral formation in comparison to porous PEEK cultures.

3.3.6 Implant Osseointegration

Three-dimensional μCT reconstructions of PEEK femoral explants at 6 and 12 weeks suggested bone formation within the PEEK-SP network (Figure 3.8). Bone ingrowth possessed cubic morphology similar to that of the pores, suggesting most available pore space was occupied by newly-formed bone. Cubic bone ingrowth regions were apparent at 4/6 porous interfaces and 0/6 smooth interfaces. Bone growth through the central cannula and along the outer surface of implants was present in 5/6 samples and originated from both proximal and distal ends.

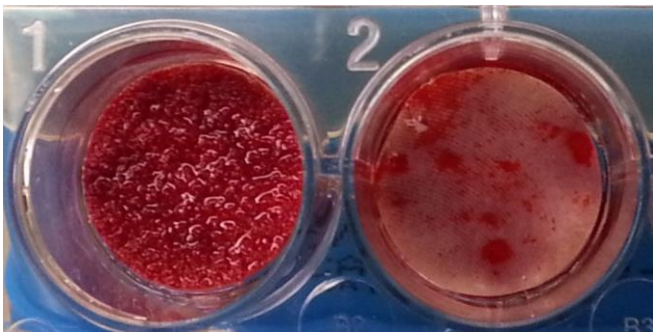

Figure 3.7 - Alizarin red calcium staining of hMSC cultures grown in osteogenic media for 4 weeks on porous PEEK (left) and smooth PEEK (right).

Histological evidence confirmed that the mineral seen within pores on µCT reconstructions was cellularized bone (Figure 3.9). At both six and twelve weeks, substantial bone formation was evident within the pore layer, with bone formation seeming to increase between the two time points. Ingrown bone was closely apposed to the pore walls and exhibited a substantial reduction in fibrous tissue formation compared to the smooth PEEK faces.

Microcomputed tomography (µCT) imaging of porous PEEK samples from the tibial implant model demonstrated that 40 ± 14% of the available pore space on tibial implants contained mineralized tissue at 8 weeks (Figure 3.10). Biomechanical pullout testing of tibial implants demonstrated that porous-faced PEEK implants exhibited over twice the integration strength of smooth PEEK implants (36.7 ± 10.0 N vs. 15.9 ± 6.3 N, $p < 0.01$) (Figure 3.10).

Qualitative agreement between µCT and histology was also confirmed by comparing bone ingrowth morphology at approximately the same cross sections using each technique. Mineral attenuation maps from µCT represented histological findings well and provided

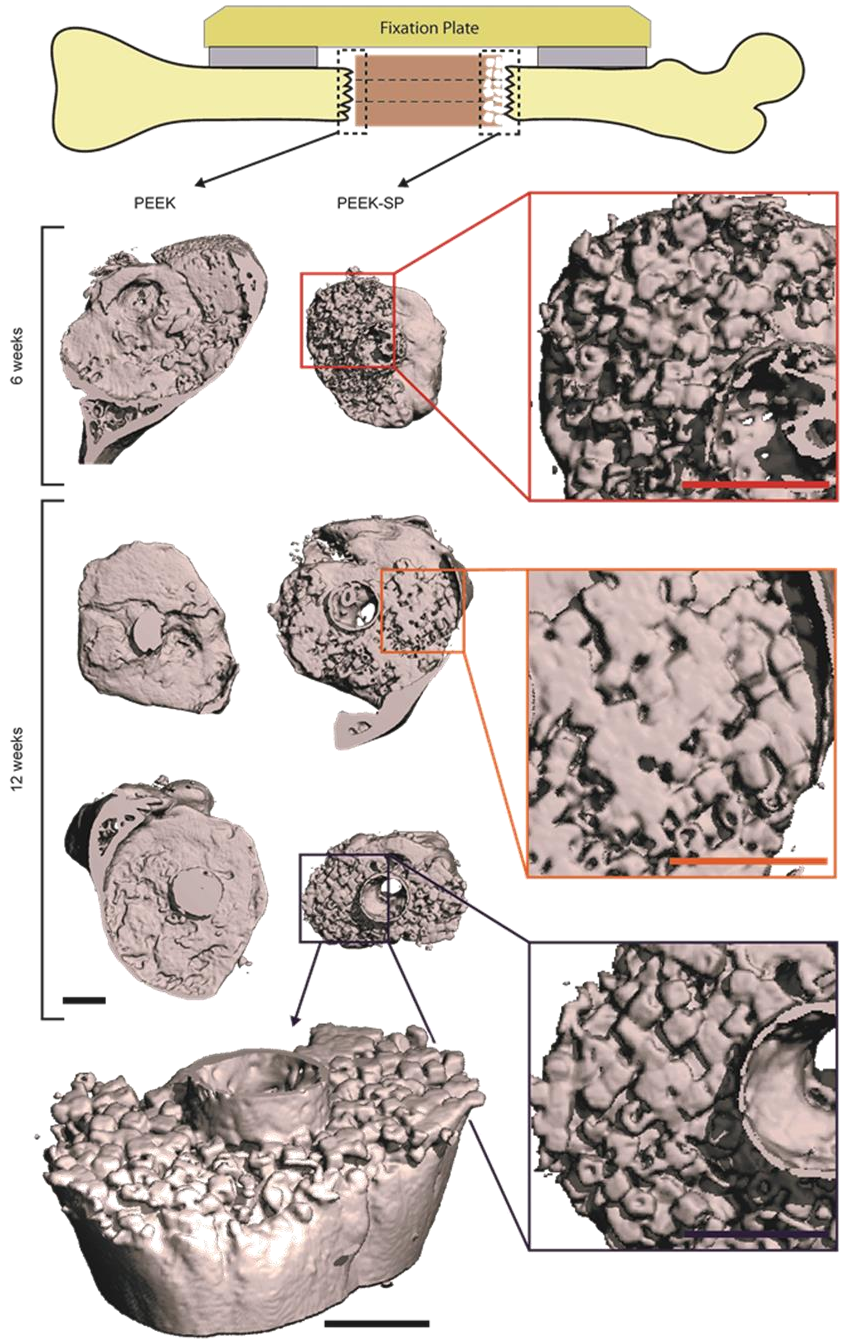

Figure 3.8 - µCT reconstructions of bone growth into PEEK-SP and adjacent to smooth PEEK surfaces (dashed boxes) at 6 and 12 weeks show the extent of bone ingrowth. Images are oriented with the lateral side on top. Insets show magnified views of ingrown bone. PEEK implants are not depicted due to thresholding difficulties of µCT reconstructions. An angled view is presented to visualize the extent of bone intrusion into the porous surface layer. Note the cubic morphology of bone in the surface porous PEEK samples, suggesting complete growth into the cubic pores. Scale bars on µCT images are 1 mm.

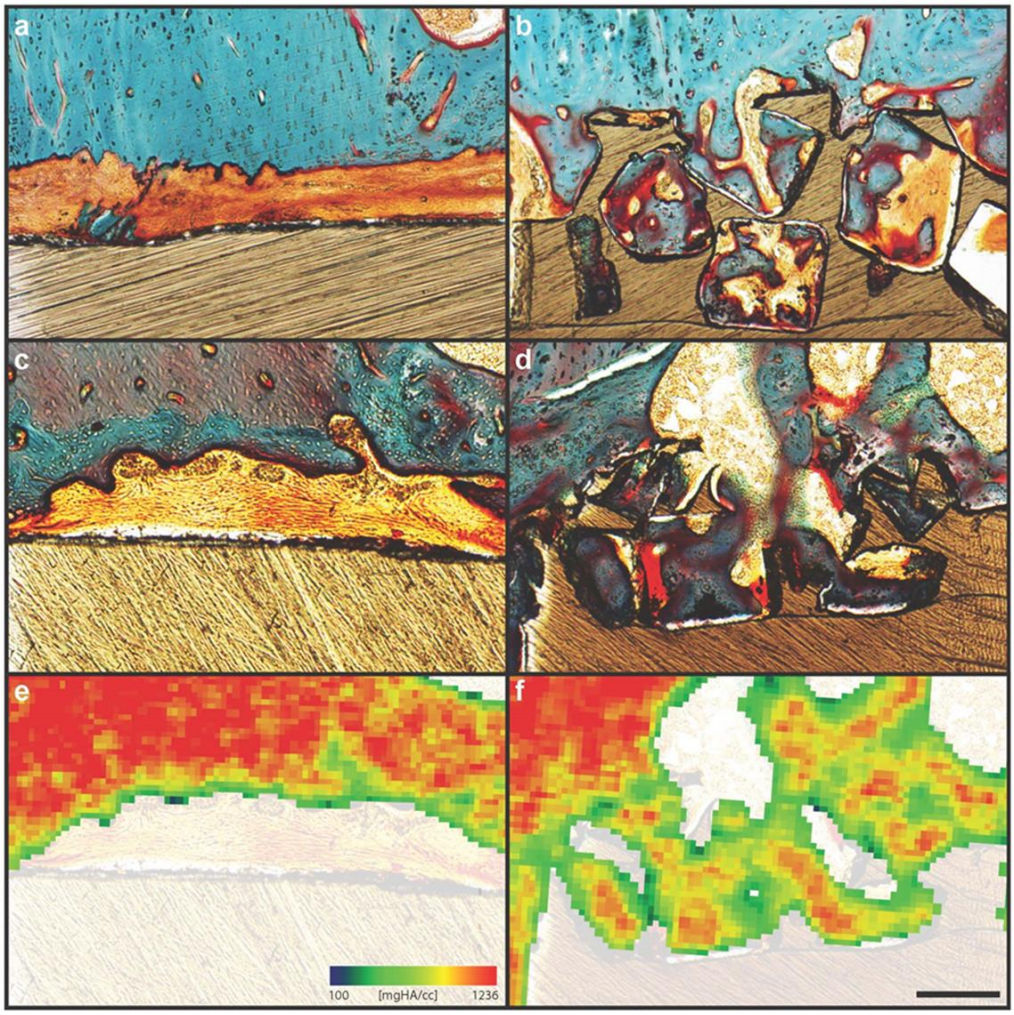

Figure 3.9 - Bone ingrowth of PEEK-SP and smooth PEEK surfaces: (a,c) Representative histological images of fibrous tissue formation on smooth PEEK faces at six and twelve weeks, respectively. (b,d) Representative histological images of bone ingrowth within PEEK-SP faces at six and twelve weeks, respectively. Osteoid stained deep red; mineralized bone stained green; fibrous tissue stained light orange; and PEEK material is seen in brown. (e,f) Representative mineral attenuation maps from µCT at approximately the same cross sections as (c,d). Blue represents lower mineral density and red indicates high mineral density. Scale bar is 200 µm.

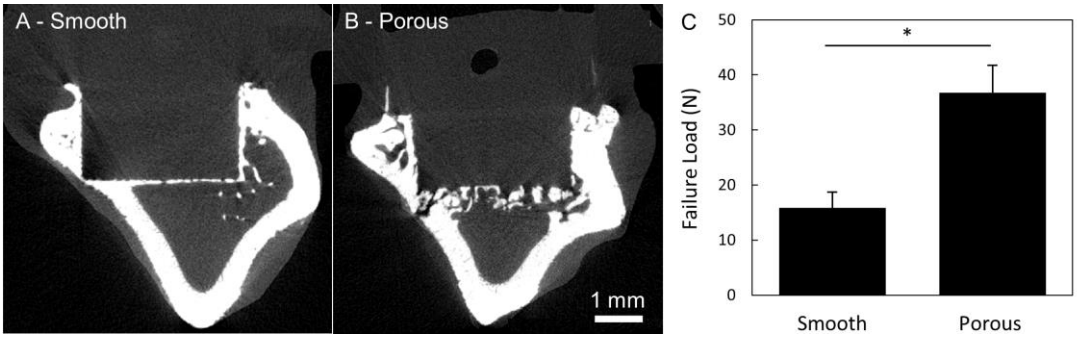

Figure 3.10 - µCT images of bone growth into (A) smooth PEEK compared to (B) porous PEEK surfaces at 8 weeks. (C) Biomechanical pullout force of smooth and porous PEEK implants at 8 weeks. * p < 0.01. (Student's t-test). Mean ± SE.

further validation for using µCT to detect bone ingrowth into the PEEK-SP pore layer (Figure 3.9).

3.4 Discussion

This study sought to create a surface porosity on PEEK to promote osseointegration while maintaining the structural integrity necessary for high load-bearing orthopaedic implants. The advantages of a surface porous polymeric implant have been previously discussed in the literature [38, 78, 91]. However, no surface porous PEEK structure has been shown to provide an adequate pore network for bone ingrowth while preserving the high strength of PEEK.

Characterization of our PEEK-SP surface layer revealed pore size, porosity and interconnectivity values that have been reported to allow for cell migration, nutrient transport, and vascularization that contribute to successful bone-implant integration [55, 78]. We also show that PEEK-SP preserved a high degree of PEEK's mechanical properties, retaining over 70% of the strength and modulus of solid PEEK when total cross-

Table 3.2 - Microstructural comparison of human bone and porous PEEK

	Porosity (%)	Pore Size / Strut Spacing (μm)	Strut Thickness (μm)	Young's Modulus (GPa)*	Yield Strength (MPa)*
Human Cortical Bone	3 - 12	-	-	11.5 - 17.0	51 - 133
Solid PEEK	-	-	-	3.4	98
Human Trabecular Bone	74 - 92	638 - 854	122 - 194	0.3 – 3.2	2 - 17
Porous PEEK	67 - 75	169 - 248	73 - 119	0.1	8 - 11

*Young's modulus and yield strength values are reported for compressive loading.

sectional area A_T is used in the stress calculation. Corresponding μCT analysis of human trabecular bone has reported similar microstructural properties as those possessed by porous PEEK [82] (Table 3.2).

Comparatively, typical bulk porous (BP) polymers reported in the literature retain only 15-36% strength and 11-39% modulus of the unprocessed polymer, depending on porous volume fraction (Figure 3.11) [54, 55, 64, 92-96].

Although the measured strength of PEEK-SP is decreased when using the total cross-sectional area A_T, the creation of a surface porosity does not significantly decrease the strength when calculated with the load-bearing area A_{LB} (Figure 3.3). The results indicate that the stress concentration effect of pores does not negatively impact material strength. The results also indicate that PEEK-SP retains its specific strength (strength/density), meaning the introduction of porosity using this processing method only spreads the material out rather than inherently weakening it. In addition, PEEK-SP possesses mechanical properties within the range of trabecular and cortical bone (Figure 3.11), a characteristic that has been suggested to improve functionality [55] Mechanical

properties can be tuned further by adjusting implant design parameters, such as decreasing layer thickness.

Given the decrease in ductility in PEEK-SP and the inherent cyclic loading experienced by orthopaedic implants, it was important to evaluate the effect of the processing on the fatigue properties of PEEK. As shown in Figure 3.4, the inherent fatigue resistance of solid PEEK was highly maintained after creation of a porous surface layer. The data also demonstrate that the fatigue resistance of PEEK-SP outperformed other clinically used orthopaedic biomaterials. PMMA, a polymer used as bone cement, did not trend towards an endurance limit and possessed much lower fatigue strength than PEEK-SP in the high cycle regime. Similarly, porous tantalum, a bulk porous metallic implant material used clinically to facilitate osseointegration, has fatigue performance almost 43% lower than surface porous PEEK at similar cycle number [97].

Because large shear stresses are experienced near bone-implant interfaces *in vivo* that can lead to micro-motion and implant loosening [98], it was essential to probe the inherent interfacial shear strength of the porous surface layer. The significant increase in interfacial shear strength of PEEK-SP compared with solid (smooth) PEEK suggests that PEEK-SP will possess the advantage of a mechanical interlock and higher bonding strength between the implant biomaterial and the surrounding natural bone once ingrowth occurs, providing greater mechanical stability at this critical interface [99]. Furthermore, PEEK-SP provides this advantage over many current techniques explored in the literature. Physical surface treatments such as plasma modification have shown increased bioactivity of PEEK implants but may not provide sufficient space for bony ingrowth and implant-bone fixation [40, 74]. In addition, PEEK implant coatings such as titanium and

hydroxyapatite have demonstrated improved cellular response [43, 100], but can be subject to delamination and decreased fatigue life [33]. Finally, sulfonation has been used to chemically modify the surface of PEEK and introduce a nanoporous surface network to improve osseointegration [38]. However, with single-micron pores that are well below the typical range for bone formation, sulfonated surface porous PEEK may not allow for the bony ingrowth that contributes to a strong mechanical interlock between the implant and bone.

The process of creating a surface porosity on PEEK implants introduces a random, topographically varied surface that may contribute to enhanced osseointegration. Such a disordered topography has been shown to improve the osteogenic response at nano- to micron-size scales [34, 101-103]. At a larger scale, porosity has also shown increased osteogenesis compared to solid or topographically smooth surfaces [55]. Together, the literature suggests that the random, topographically varied PEEK-SP surface may enhance the cellular response, leading to more stable fixation than PEEK that is smoother at the cellular level.

Though PEEK-SP and PEEK-BP both offer the potential for bone ingrowth into the porous network, the significantly lower shear strength of PEEK-BP may limit its clinical use in rigorous loading environments. The three-fold higher shear strength of PEEK-SP could be attributed to the porous surface layer being extruded from the bulk material instead of being created with the additive or sintering techniques currently used to create PEEK-BP. Extrusion of PEEK-SP from the bulk material seamlessly integrates solid and porous regions at the molecular level and maintains the high molecular weight necessary for high strength (Table 3.1). Notably, the surface porous layer has higher

interfacial shear

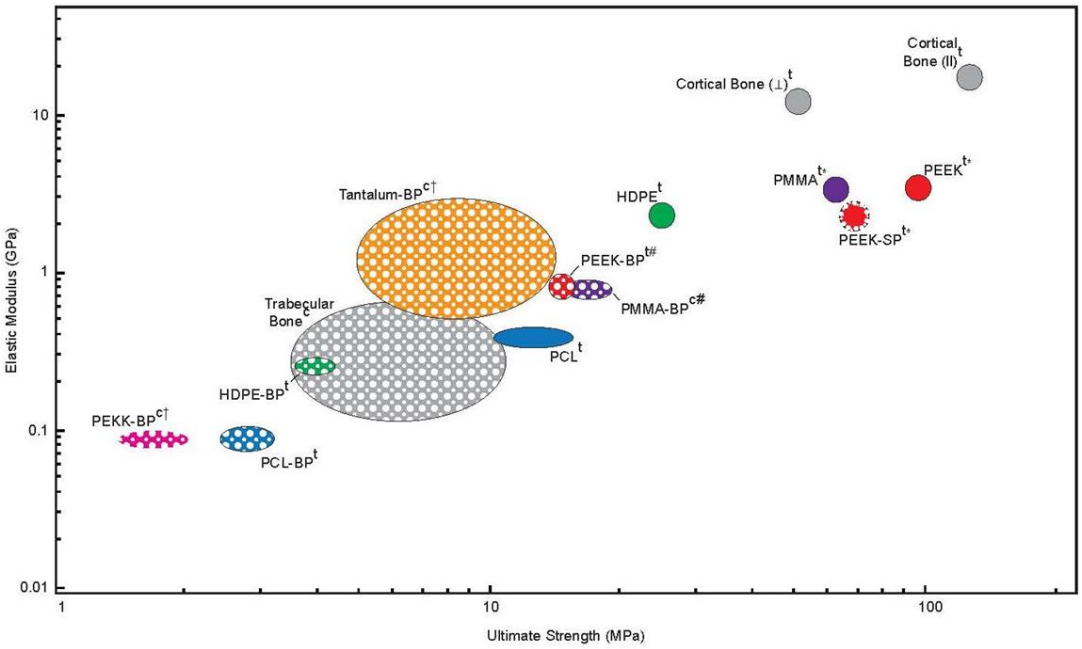

Figure 3.11 - Ashby plot of elastic moduli and ultimate strengths for several orthopaedic biomaterials and bone that have been reported in the literature [3, 20, 33-38]. Solid-filled ellipses represent fully dense materials and porous-filled ellipses represent porous materials. While cortical bone does possess low porosity, it is grouped with the fully dense materials for this comparison. Each material, with the exception of porous tantalum and polyether-ketone-ketone (PEKK), has both solid and porous properties included to illustrate the reduction in properties due to porosity. PEEK-SP is indicated by a porous layer outlining the solid-filled circle. Superscript 't' refers to materials tested in tension and 'c' indicates compression. Daggers (†) indicate yield strengths where ultimate strength was not reported. Pound signs (#) indicate bending modulus when elastic modulus was not reported. Asterisks (*) indicate values tested by our group. Ellipse central location and size represents reported mean and plus or minus one standard deviation, respectively, where available.

strength than trabecular bone [104] (Figure 3.5), which implies that failure will originate from bone itself and not the solid-porous interface even when high quality bone has fully integrated.

Preliminary *in vitro* and *in vivo* results provide further evidence of PEEK-SP's capacity to promote cell attachment, osteogenic differentiation, and bony ingrowth needed

for strong implant fixation. Substantial bone formation within the pore layer was confirmed via μCT and histology at six and twelve weeks post-surgery. These initial *in vivo* results compare favorably with previously reported porous networks with similar architectures to PEEK-SP. For example, a porous PEEK-HA composite has been shown to facilitate bone ingrowth with close apposition to the pore walls, similar to PEEK-SP [39]. However, even the nonporous form of current PEEK-HA composites can lack the strength, ductility and fatigue resistance of PEEK-SP.

A direct comparison of PEEK-SP to porous titanium can be found in a study that used a nearly identical segmental defect model in the rat [88]. This study reports a time course of bone ingrowth close to that of PEEK-SP and also describes similar histological findings. Both studies found substantial bone formation in the central cannula and around the outside of the implants, illustrating an attempt by bone to bridge the defect. Both studies also found close bone apposition to the pore walls (or struts) with the presence of some fibrous tissue in regions where bone was absent.

Though some fibrous tissue formation was apparent within the PEEK-SP pore network, the degree to which it formed was reduced compared to the characteristic fibrous encapsulation of smooth PEEK seen in Figure 3.9 and in previous studies [29, 30]. Many regions of PEEK-SP possessed pores that were completely filled with cellularized bone and no fibrous layer was observed between the bone and implant. Such reduced fibrous encapsulation combined with potentially faster bone ingrowth could increase implant stability and limit micromotion that can lead to increased inflammation and eventual implant loosening and failure [17, 34, 105].

The clinical potential of PEEK-SP is further illustrated with the clearance of this technology on a suture anchor implant through the Food and Drug Administration (FDA) in the United States (marketed as Scoria^{TM}). Despite these promising preliminary findings, further work is necessary to fundamentally understand what causes bone formation within the PEEK-SP pore layer and the quantitative mechanics behind the osseointegration of PEEK-SP [106].

3.5 Conclusion

We have investigated a process for selectively introducing surface porosity on PEEK that retains a substantial fraction of the solid polymer's mechanical properties. This method provides many advantages over sintered bulk porous polymers that rely on superficial bonding between polymer particles, which severely compromises mechanical properties. The creation of a surface porosity produced samples with high tensile strength, fatigue resistance and interfacial shear strength while simultaneously providing available porosity for bone ingrowth. Preliminary *in vitro* and *in vivo* results provided evidence of cell attachment, osteogenic differentiation, and bone ingrowth into the pore network, which could lead to enhanced implant stabilization. Though the cubic morphology of ingrown bone produced by this technique provides convincing preliminary evidence of improved osseointegration, the functionality of bone ingrowth remains to be determined in future studies.

CHAPTER 4. DO SURFACE POROSITY AND PORE SIZE INFLUENCE MECHANICAL PROPERTIES AND CELLULAR RESPONSE TO PEEK?[2]

In CHAPTER 3 the mechanical properties and preliminary *in vitro* and *in vivo* osseous responses to porous PEEK surfaces were investigated. The porous PEEK surfaces were shown to have adequate strength for load-bearing orthopaedic applications and exhibited favorable osteogenic differentiation and osseointegration compared to smooth PEEK. In this chapter the porous PEEK network was modified to investigate the effect of pore size on mechanical properties and osteogenic differentiation of mouse pre-osteoblasts *in vitro*.

4.1 Introduction

Polyether-ether-ketone (PEEK) is a polymer widely used in orthopaedic and spinal applications such as soft tissue repair and spinal fusion devices due to its high strength, fatigue resistance, radiolucency, and favorable biocompatibility in osseous environments [27, 73, 107-109]. However, due in part to PEEK's relatively inert and hydrophobic surface, recent evidence has demonstrated that smooth PEEK can exhibit poor osseointegration [27, 28] and fibrous capsule formation around the implant [29, 30]. Lack of bone-implant contact can induce micromotion and inflammation that leads to fibrous layer thickening, osteolysis, and implant loosening [31-35]. Previous studies [39-41, 43, 44, 74] have shown that surface modifications such as plasma treatments, coatings, and

[2] Modified from F.B. Torstrick*, N.T. Evans*, H.Y. Stevens, K. Gall, R.E. Guldberg, Do Surface Porosity and Pore Size Influence Mechanical Properties and Cellular Response to PEEK?, Clin. Orthop. Relat. R. 474 (2016) 2373-2383.

composites can improve PEEK implant integration, yet many suffer practical limitations such as delamination, instability, and mechanical property trade-offs.

The addition of porosity is a common modification to improve implant osseointegration by facilitating bone ingrowth and vascularization [56]. The importance of porosity for bone regeneration has been reviewed [55], and methods to create porous PEEK have been reported [38, 64, 66, 107, 108, 110]. However, it's still unclear which aspects of the pore architecture (such as pore size, porosity, and pore layer thickness) control the mechanical and biological properties of porous PEEK implants. Furthermore, the overall volume of porosity and its spatial distribution throughout the implant should be considered due to the inverse relationship between porosity and strength of porous structures [111]. For example, limiting porosity to just a thin surface layer could facilitate adequate ingrowth for stable implant fixation while preserving the solid core for load bearing.

Previously, our group described a surface porous PEEK (PEEK-SP) structure with high tensile strength, fatigue resistance, interfacial shear strength, and improved osseointegration compared to smooth PEEK [110]. Though the pore size investigated (200-312 μm) was within the commonly accepted range for porous orthopaedic implants [55], additional work is needed to investigate whether the pore microstructure could be reliably controlled to yield other pore sizes and the subsequent effect of pore size on both the mechanical properties and biological responses to PEEK-SP.

We therefore asked the following three questions: (1) Can PEEK-SP microstructure be reliably controlled? (2) What is the effect of pore size on the mechanical properties of PEEK-SP? (3) Do surface porosity and pore size influence the cellular response to PEEK?

4.2 Materials and Methods

4.2.1 Overview

In order to evaluate the degree to which PEEK-SP microstructure can be reliably controlled, we processed the material using three porogen sizes and characterized the resulting microstructure using microcomputed tomography. In order to assess the influence of pore size on mechanical properties of PEEK-SP, we performed monotonic tensile tests to evaluate the strength, failure strain, and modulus; tensile fatigue tests to evaluate the fatigue life; and interfacial shear tests to evaluate the interfacial shear strength of the surface porous layer. Finally, to determine whether surface porosity and pore size influence the cellular response to PEEK, we cultured human femoral osteoblasts, human vertebral mesenchymal stem cells, and mouse pre-osteoblasts on PEEK-SP of all three pore sizes and compared the proliferation and osteogenic differentiation of the cells to smooth PEEK, Ti6Al4V, and tissue culture polystyrene (TCPS).

4.2.2 Materials

Medical grade PEEK Zeniva® 500 was provided by Solvay Specialty Polymers (Alpharetta, GA, USA). Medical grade Ti6Al4V ELI (extra low interstitials) was purchased from Vulcanium (Northbrook, IL, USA) and the surface was fine grit blasted (GB-13 blast media) and anodized according to AMS 2488D Type II by Danco (Arcadia, CA). Sodium chloride was purchased from Sigma (St. Louis, MO).

4.2.3 Sample Preparation

Surface porous PEEK was created by extruding PEEK through the open spacing of sodium chloride crystals under heat and pressure as described previously [110]. By controlling the applied pressure and the time of processing, the flow distance was limited resulting in samples with a surface porosity and a solid core. After cooling, embedded sodium chloride crystals were leached in water leaving behind a porous surface layer. To control for pore size, sodium chloride was sieved into ranges of 200-312 μm, 312-425 μm, and 425-508 μm using #70, #50, #40, and #35 US mesh sieves. Samples processed using each size range are referenced as PEEK-SP-250, PEEK-SP-350, and PEEK-SP-450, respectively. Injection molded PEEK samples (PEEK-IM) were used as nonporous controls for mechanical testing. For cell studies, smooth nonporous PEEK samples were manufactured with a machined surface finish. Nonporous, machined smooth PEEK, PEEK-SP pore walls, and Ti6Al4V surfaces possessed a surface roughness (S_a) of 0.59 ± 0.12 μm, 0.48 ± 0.10 μm, and 0.55 ± 0.02 μm, respectively, determined by laser confocal microscopy using a 50x/0.5 mm objective, 50 nm step size and λ_c = 20 μm (LEXT OLS4000 , Olympus, Waltham, MA). S_a values were not statistically different between groups (p = 0.28, 1-way ANOVA).

4.2.4 Pore Layer Characterization

PEEK-SP samples were evaluated using microcomputed tomography (μCT 50; Scanco Medical , Switzerland) to measure the pore size, percent porosity, strut thickness, strut spacing, pore interconnectivity, and pore layer thickness. Samples were analyzed at 10 μm voxel resolution with the scanner set at a voltage of 55 kVp and a current of 200 μA (n = 10). Contouring, the method of delineating the region of interest from areas not included

in evaluation, was used to carefully select the pore layer volume and to minimize inclusion of non-porous volume. A global threshold was applied to segment PEEK from pore space for all evaluations. The global threshold was determined by analyzing the attenuation histograms for a representative sample of scans using an adaptive thresholding algorithm (Scanco) and confirmed visually prior to segmentation. Pore layer morphometric parameters were evaluated using direct distance transformation methods as described previously [82, 110]. The depth of the pore layer was calculated as the mean thickness of the filled in contour around each pore layer. Pore size was measured from μCT cross sections as the length of the pore diagonal (ImageJ, n = 375).

4.2.5 Monotonic and Fatigue Testing

Ultimate stress, failure strain, and elastic modulus were determined from monotonic tensile tests. Tensile tests were performed on Type I dog-bones according to ASTM D638 at room temperature using a Satec (MTS, Eden Prairie, MN) 20 kip (89 kN) servo-controlled, hydraulically-actuated test frame (n = 5). The crosshead speed was 50 mm/min. Force-displacement data as measured by the cross-head and validated by video (Canon HG10, Lake Success, NY) and image processing software (ImageJ, NIH, Bethesda, MD) were used to calculate ultimate stress, failure strain , and elastic modulus as well as to generate stress-strain curves. The reported results are engineering stress-strains.

Fatigue tests were run at sequentially lower stresses (3% decreases) below the ultimate stress of the samples to generate S-N curves and determine the endurance limits of the respective samples. Fatigue tests were run on the same Satec test frame in axial stress

control at a frequency of 1 Hz and and R-value of 0.05. Tests were run until failure or runout. Runout was defined as greater than 1,000,000 cycles.

For monotonic and fatigue results, two representations of stress for PEEK-SP were calculated: The first using the load-bearing area, A_{LB} (the cross-sectional area of PEEK material in the gage region, minus the pore area), and the second using the total area, AT (the cross-sectional area of the gage region, including the pores). Use of total area produced stress values that assume void area contributed to load-bearing, and results consequently depend on pore layer thickness and volume fraction of porosity. Conversely, load-bearing area includes only the cross-sectional area of polymer material, including solid polymer and porous strut regions, ignoring void area in the porous layer.

4.2.6 Aligned Interfacial Shear

Interfacial shear testing was used to assess the strength of the pore layer struts and predict their potential to withstand shearing loads experienced during implant insertion of after implantation. The test method was adapted from ASTM F1044-05 using Scotch-weld™ 2214 NonMetallic Filled (3M, St. Paul, MN) as adhesive and a 30 kN load cell (Instron 5567, Norwood, MA). A thin layer of adhesive was applied evenly to the surfaces of shear samples, and like faces were pressed together, clamped, and placed in a vacuum oven to cure at 121°C for 1 hour. The shear test fixtures were clamped in Instron jaws and adjusted to enable horizontal alignment of the shear sample. The plane of the adhesive was coincident with the axis of loading. Cured samples were placed into custom fixtures ensuring a tight clearance fit. The fixtures were pulled apart at 2.54 mm/min until the

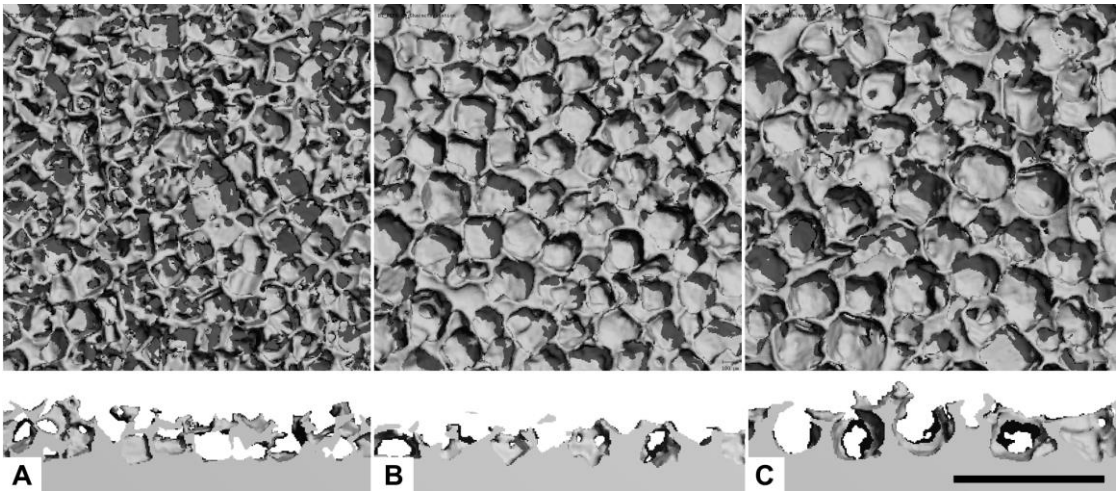

Figure 4.1 - Representative µCT reconstructions of the surface and cross-section of PEEK-SP. (A) PEEK-SP-250, (B) PEEK-SP-350, and (C) PEEK-SP-450 are shown.

interfacial surfaces of the samples were completely sheared. The interfacial shear stress was calculated based on the measured failure load and cross-sectional area.

4.2.7 In vitro Proliferation and Osteogenic Differentiation

Proliferation of human femoral osteoblasts (hOB, ScienCell, Carlsbad, CA) and human vertebral mesenchymal stem cells (hMSC, ScienCell) was evaluated on smooth nonporous PEEK, PEEK-SP-250, PEEK-SP-350, PEEK-SP-450, Ti6Al4V, and tissue culture polystyrene (TCPS) (n = 6) by measuring DNA incorporation of 5-ethynyl-2'-deoxyuridine (EdU) (Click-iT®-EdU, ThermoFisher, Waltham, MA) . hOB and hMSC were seeded at 10,000 cells/cm^2 in growth media (ScienCell, Carlsbad, CA) and proliferation was measured at 48 hours per the manufacturer's instructions. Osteogenic differentiation was evaluated on each surface utilizing clonal mouse preosteoblast cells (MC3T3-E1, ATCC, Manassas, VA) due to their homogeneity, availability and differentiation profile that is

Table 4.1 – PEEK-SP pore layer morphometrics

Surface	Pore size (μm)	Strut spacing (μm)	Strut thickness (μm)	Porosity (%)	Interconnectivity (%)	Layer thickness (μm
PEEK-SP-250	284 ± 35	169 ± 3	73 ± 8	69 ± 3	99.9 ± 0.04	391 ± 79
PEEK-SP-350	341 ± 49*	208 ± 5*	104 ± 9*	61 ± 3*	99.8 ± 0.17	303 ± 29*
PEEK-SP-450	416 ± 54*,†	248 ± 1*,†	119 ± 14*,†	62 ± 4*	99.8 ± 0.25	342 ± 38

Mean ± SD; *$p < 0.01$ versus SP-250; † $p < 0.05$ versus SP-350 (one-way analysis of variance, Tukey).

more similar to human osteoblasts than other *in vitro* models [112]. MC3T3 cells were seeded at 20,000 cells/cm^2 in growth media composed of α-MEM (Life Technologies, Carlsbad, CA) supplemented with 16.7% fetal bovine serum (FBS) (Atlanta Biologicals, Lawrenceville, GA) and 1% Penicillin-Streptomycin-L-glutamine (PSL, Life Technologies). Cells were cultured under dynamic conditions using a rocker plate. After 3 days cells reached confluence and half of all samples were switched to osteogenic media comprising growth media supplemented with 6 mM β-glycerophosphate, 1 nM dexamethasone, 50 ng/ml thyroxine, 50 μg/ml ascorbic acid 2-phosphate, and 1 nM 1α,25-Dihydroxyvitamin D3 (Sigma, St. Louis, MO). The remaining half of the samples were maintained in growth media. Samples were cultured for 14 days after confluence, changing media every 3 to 4 days. At 14 days samples undergoing assays for alkaline phosphatase (ALP) activity and DNA content were washed with phosphate-buffered saline ((-Ca^{2+}/-Mg^{2+}), ultrasonically lysed in Triton X-100 (0.05% in PBS) and subjected to one freeze-thaw cycle prior to further analysis. Samples assayed for calcium were washed with PBS (-Ca^{2+}/-Mg^{2+}) and vortexed overnight at 4°C in 1 N acetic acid to solubilize calcium. ALP activity, an early osteogenic differentiation marker, was determined by colorimetric intensity of cell lysates exposed to p-Nitrophenyl phosphate (pNPP, Sigma, St. Louis, MO) and was normalized to same-well DNA content determined by a Picogreen dsDNA assay (Life Technologies, Carlsbad, CA). Calcium deposition, a marker indicative of mineralization, in parallel cultures was determined by a colorimetric Arsenazo III reagent

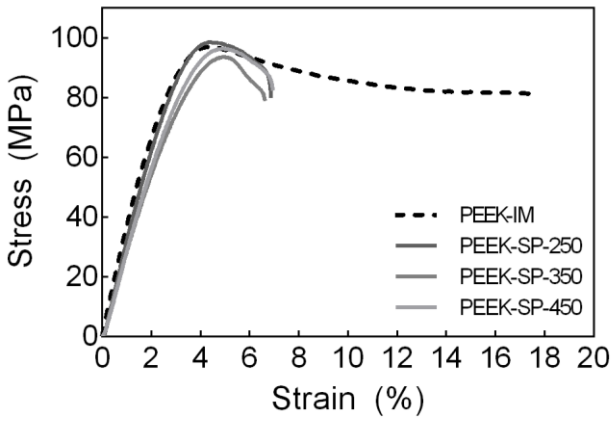

Figure 4.2 - Representative stress-strain curves of PEEK-IM and PEEK-SP.

assay (Diagnostic Chemicals Ltd., Oxford, CT). To determine the extent of non-cell-mediated mineral deposition, the assay was also performed on acellular control samples and on samples seeded with a non-mineralizing cell line (Human Embryonic Kidney (HEK), ATCC, Manassas, VA). HEK cells were seeded to reach confluency at the same 3-day time point as MC3T3 cultures. Both acellular and HEK controls were cultured under osteogenic conditions. Vascular Endothelial Growth Factor (VEGF) production by MC3T3-E1 cells was measured from culture media at Day 14 after confluence using an ELISA and normalized to same-well DNA content (R&D Systems, Minneapolis, MN).

Results of mechanical tests were analyzed using a one-way ANOVA and Tukey post-hoc analysis (95% confidence interval). *In vitro* assays were analyzed using a one-way ANOVA for EdU assays and a two-way ANOVA for all other assays. Tukey post-hoc tests were used to compare all *in vitro* groups. All data are expressed as mean ± standard deviation (S.D.)

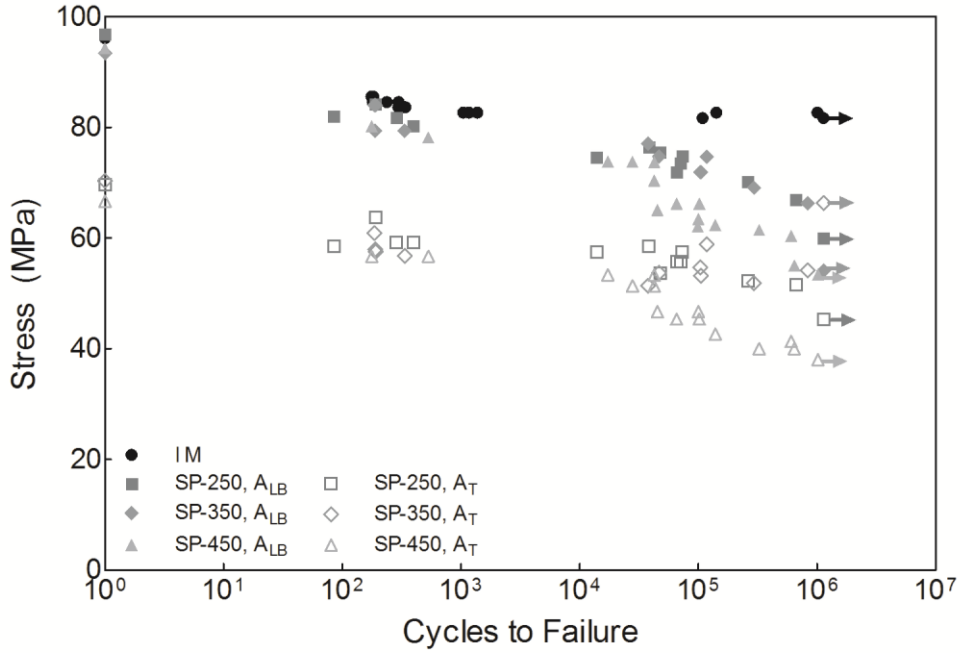

Figure 4.3 - Stress versus loading cycle (S–N) curves comparing the fatigue behavior of PEEK-IM and PEEK-SP of different pore sizes. The arrows denote tests that were halted after reaching 1 x 10^6 cycles, which was defined as the runout cyclic stress.

4.3 Results

4.3.1 Can PEEK-SP Microstructure Be Controlled?

Using µCT analysis, we found that pore morphology could be reliably controlled by varying the sodium chloride crystal size with the pores conforming to the porogen's cubic shape (**Figure 4.1**). The data demonstrate that salt crystal size can be used to reliably control the pore size of PEEK-SP (SP-250 = 284 ± 35 µm, SP-350 = 341 ± 49 µm, SP-450 = 416 ± 54 µm) ($p < 0.001$). Porosity was slightly affected with SP-250 having marginally higher porosity (69 ± 3 %) compared to SP-350 (61 ± 3 %) and SP-450 (62 ± 4 %) ($p < 0.001$). All three groups had high levels (> 99%) of pore interconnectivity (Table 4.1).

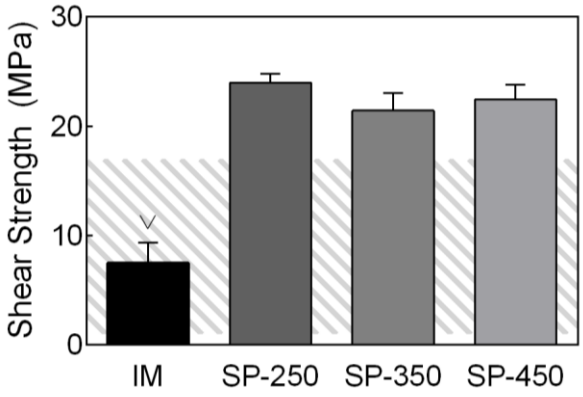

Figure 4.4 - Interfacial shear strength of PEEK-SP compared with the strength of the PEEK-IM contacting adhesive with the shear strength of trabecular bone shown in the shaded region [14, 17]. ^{V} p < 0.001 versus all SP groups (one-way ANOVA, Tukey). Mean ± SD.

4.3.2 Effect of Pore Size on Mechanical Properties

Mechanical testing results showed that varying PEEK-SP pore size within the studied range had relatively little influence on tensile strength, interfacial shear strength and ductility; however, the data suggests that larger pores (SP-450) led to lower fatigue strength. Compared to the tensile strength of PEEK-IM (97.7 ± 1.0 MPa; 95% CI, 96.5 - 99.0), PEEK-SP showed no difference in tensile strength when normalized to A_{LB} for PEEK SP-250 (96.1 ± 2.6 MPa; 95% CI, 93.4 – 98.9; p = 0.458) and PEEK SP-450 (94.5 ± 1.4 MPa; 95% CI, 92.8 – 96.2; p = 0.050) but there was a small decrease for the PEEK-SP-350 group (93.4 ± 1.5 MPa; 95% CI, 91.5 – 95.2; p = 0.006) (Figure 4.2). All pore sizes showed a decrease in ductility compared to PEEK-IM as indicated by a decrease in failure strain (IM = 20.2 ± 2.4%, 95% CI, 17.2 – 23.3; SP-250 = 7.8 ± 2.2%, 95% CI, 5.4-10.2; SP-350 = 7.0 ± 0.9%, 95% CI, 5.9 – 8.0; SP-450 = 8.1 ± 1.5%, 95% CI, 6.3 – 10.0)

Table 4.2 – Mechanical properties of PEEK-SP

Surface	Tensile strength, A_{LB} (MPa)	Tensile strength, A_T (MPa)	Failure strain (%)	Modulus, A_{LB} (GPa)	Modulus, A_T (GPa)
PEEK-IM	97.7 ± 1.0	97.7 ± 1.0	20.2 ± 2.4	3.3 ± 0.1	3.3 ± 0.1
PEEK-SP-250	96.1 ± 2.6	71.1 ± 2.2*	7.8 ± 2.2*	3.4 ± 0.3	2.5 ± 0.3*
PEEK-SP-350	93.4 ± 1.5*	70.3 ± 3.4*	7.0 ± 0.9*	3.3 ± 0.2	2.5 ± 0.2*
PEEK-SP-450	94.5 ± 1.4	67.0 ± 1.5*,†	8.1 ± 1.5*	3.2 ± 0.3	2.3 ± 0.2*

Mean ± SD; load-bearing area, A_{LB}, includes only the cross-sectional area of the polymer materials, ignoring void area; the total area, A_T, assumes void area contributes to load bearing area and is thus the measured sample dimensions; *$p < 0.01$ versus IM; † $p < 0.01$ versus SP-250 (one-way analysis of variance, Tukey).

($p < 0.001$) (Table 4.2). No difference was found in the modulus between PEEK-SP samples and PEEK-IM when using A_{LB}; however, differences were evident when normalized to AT (IM = 3.3 ± 0.1 GPa, 95% CI, 3.2 – 3.5; SP-250 = 2.5 ± 0.3MPa, 95% CI, 2.1 - 2.8; SP-350 = 2.5 ± 0.2MPa, 95% CI, 2.2 – 2.8; SP-450 = 2.3 ± 0.2 MPa, 95% CI, 2.0 – 2.6) ($p < 0.001$) (Table 4.2). Fatigue tests showed that surface porosity decreased the fatigue strength of PEEK, with the difference being more qualitatively pronounced at higher cycles (lower cyclic stresses) (Figure 4.3). Furthermore, PEEK-SP-450 appears to have a lower fatigue strength than the PEEK-SP-250 material. Runout stress at one million cycles was 81.7 MPa for PEEK-IM, 60.0 MPa (A_{LB}) and 45.3 MPa (A_T) for PEEK-SP-250, 54.1 MPa (A_{LB}) and 66.3 MPa (A_T) for PEEK-SP-350, and 53.4 MPa (A_{LB}) and 38.0 MPa (A_T) for PEEK-SP-450. The mean interfacial shear strength of PEEK-IM (7.5 ± 3.6 MPa, 95% CI, 1.7-13.3) was less than PEEK-SP-250 (24.0 ± 2.3 MPa, 95% CI, 22.1-25.8), PEEK-SP-350 (21.4 ± 4.3 MPa, 95% CI, 17.4 – 25.4), and PEEK-S P-450 (22.4 ± 3.6 MPa, 95% CI, 19.1 – 25.8) ($p < 0.001$) (Figure 4.4). Different interfacial shear failure modes were apparent for smooth PEEK and PEEK-SP. Smooth PEEK failed at the glue layer interface and the PEEK-SP samples failed within the porous network and within the solid region on the edges of some samples.

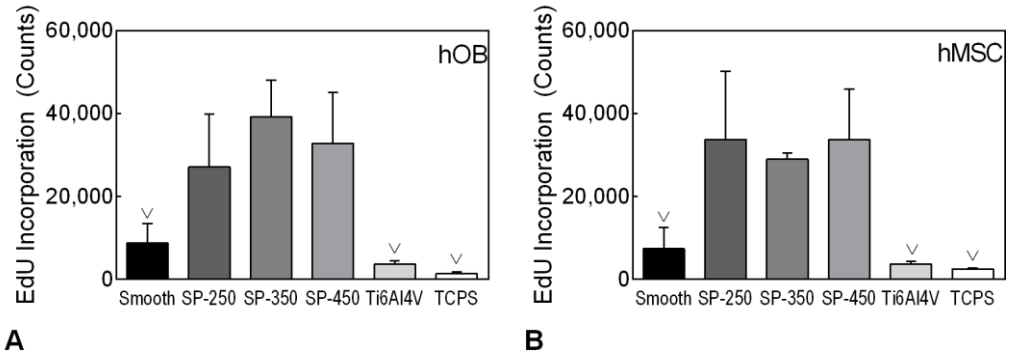

Figure 4.5 - (A) hOB and (B) hMSC proliferation measured by DNA incorporation of EdU 48 hours after seeding on smooth PEEK, PEEK-SP of various pore sizes, Ti6Al4V, and TCPS. ^{v} $p < 0.01$ versus all SP groups (one-way ANOVA, Tukey). Mean ± SD.

4.3.3 Influence of Surface Porosity on Cellular Response

Over all, cells cultured on PEEK-SP surfaces (regardless of pore size) exhibited a more differentiated phenotype than those cultured on PEEK-IM. All PEEK-SP groups had greater EdU DNA incorporation, which is indicative of increased cell proliferation, than smooth nonporous PEEK, Ti6Al4V, and TCPS surfaces for both hOBs and hMSCs cultures (hOB: Smooth = 8,752 ± 4,700 counts, SP-250 = 27,065 ± 12,812, SP-350 = 38,200 ± 8,874, SP-450 = 32,810 ± 12,257, Ti6Al4V = 3,583 ± 924, TCPS = 1,341 ± 419. hMSC: Smooth = 7,343 ± 5,098, SP-250 = 33,738 ± 16,485, SP-350 = 28,937 ± 1,581, SP-450 = 33,636 ± 12,341, Ti6Al4V = 3,685 ± 636, TCPS = 2,474 ± 274.) ($p < 0.001$, except smooth vs. SP-250 (hOB), $p = 0.008$) (Figure 4.5). However, there were no differences found in EdU incorporation between pore sizes ($p > 0.148$). Likewise, all PEEK-SP groups had similar calcium levels ($p > 0.77$ 9) that were much greater than smooth PEEK ($p < 0.001$), Ti6Al4V ($p < 0.001$) and TCPS ($p < 0.001$) in osteogenic conditions (Growth: Smooth = 5.7 ± 2.3 µg, SP-250 = 5.2 ± 1.4, SP-350 = 5.8 ± 1.4, SP-450 = 5.3 ± 0.5, Ti6Al4V = 3.0 ±

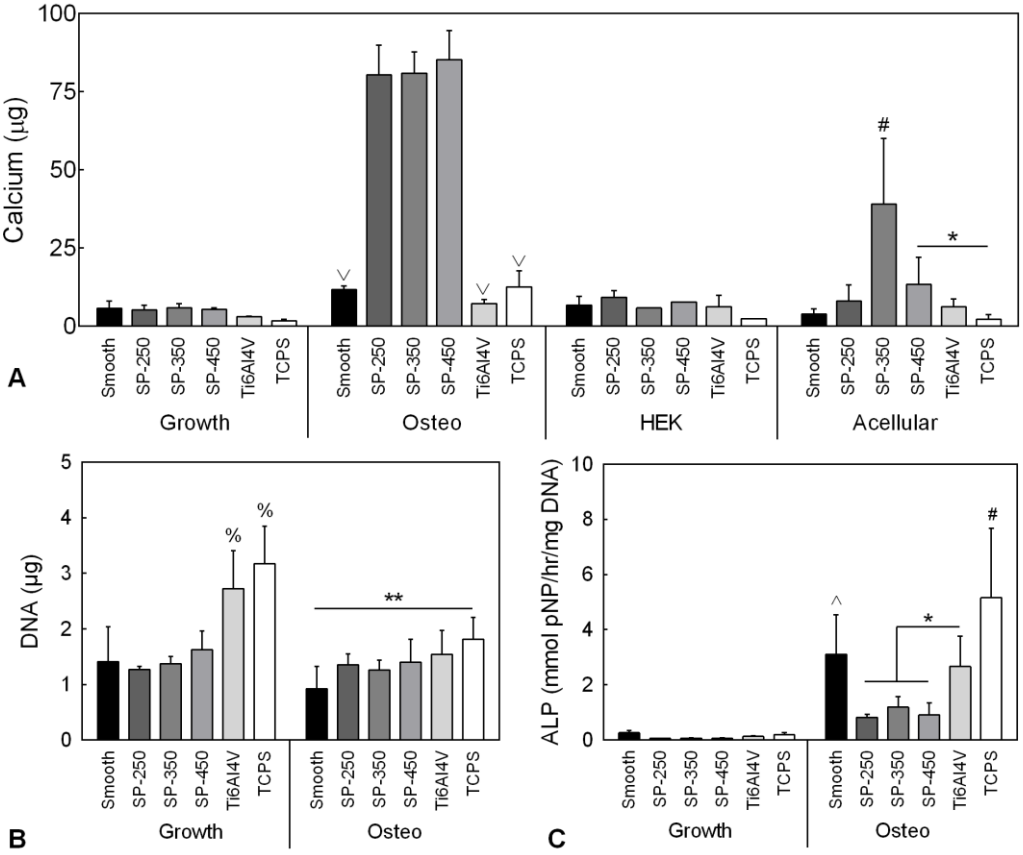

Figure 4.6 - (A) MC3T3 mediated calcium deposition on PEEK-SP groups compared with smooth PEEK, Ti6Al4V, and TCPS in growth media and osteogenic media. HEK cell and acellular cultures were used to determine the extent of noncell-mediated mineralization. Osteo: $^{\vee}p < 0.001$ versus all SP groups; acellular: $^{\#}p < 0.001$ versus all groups, $^{*}p < 0.05$ (two-way ANOVA, Tukey). (B) DNA content of parallel cultures on the same groups as in A. Growth: $^{\%}$ $p < 0.001$ versus all PEEK groups; Osteo: $^{**}p < 0.01$ (two-way ANOVA, Tukey). (C) ALP activity of same-well cultures as B. Osteo: $^{\wedge}p < 0.05$ versus all SP groups, $^{\#}p < 0.01$ versus all groups, * $p < 0.05$ (two-way ANOVA, Tukey). Mean ± SD.

0.2, TCPS = 1.6 ± 0.6. Osteogenic: Smooth = 11.6 ± 1.3, SP-250 = 80.4 ± 9.4, SP-350 = 80.9 ± 6.7, SP-450 = 85.2 ± 9.4, Ti6Al4V = 7.2 ± 1.3, TCPS = 12.5 ± 5.2. HEK: Smooth = 6.7 ± 2.8, SP-250 = 9.2 ± 2.1, SP-350 = 5.8 ± 0.1, SP-450 = 7.7 ± 0.1, Ti6Al4V = 6.2 ± 3.7, TCPS = 2.4 ± 0.1. Acellular: Smooth = 3.9 ± 1.7, SP-250 = 8.1 ± 5.1, SP-350 = 39.0

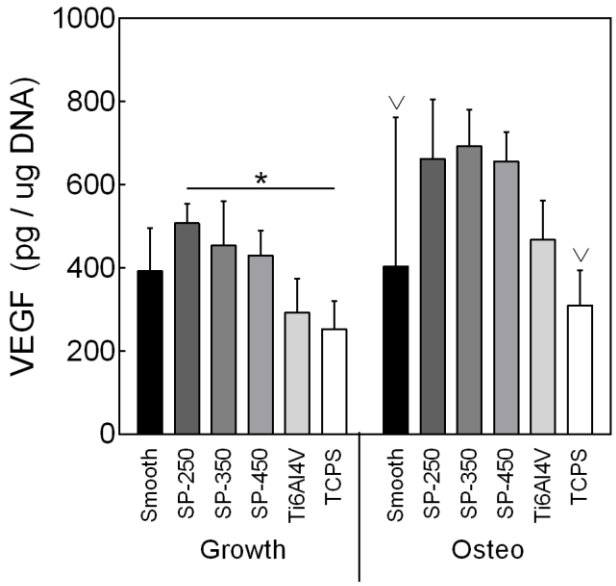

Figure 4.7 - VEGF secretion from MC3T3-E1 cells on PEEK-SP groups compared with machined smooth PEEK, Ti6Al4V, and TCPS in growth media and osteogenic media. ᵛ p < 0.05 versus all SP groups, *p < 0.05 (two-way ANOVA, Tukey). Mean ± SD.

± 21.0, SP-450 = 13.3 ± 8.8, Ti6Al4V = 6.1 ± 2.6, TCPS = 2.2 ± 1.4.) (Figure 4.6). As expected, an overall reduction in calcium was seen on acellular controls and was further reduced in HEK groups, approaching levels detected in MC3T3 groups under growth media conditions. No differences in calcium were found between groups for MC3T3 cultures in growth media or HEK cultures ($p > 0.723$). Under osteogenic conditions, smooth PEEK supported fewer cells than TCPS (Growth: Smooth = 1.4 ± 0.6 µg, SP-250 = 1.3 ± 0.1, SP-350 = 1.4 ± 0.1, SP-450 = 1.6 ± 0.4, Ti6Al4V = 2.7 ± 0.7, TCPS = 3.2 ± 0.7. Osteogenic: Smooth = 0.9 ± 0.4, SP-250 = 1.4 ± 0.2, SP-350 = 1.3 ± 0.2, SP-450 = 1.4 ± 0.4, Ti6Al4V = 1.5 ± 0.4, TCPS = 1.8 ± 0.4) ($p = 0.009$) (Figure 4.6). In growth media, TCPS and Ti6Al4V surfaces supported more cells than all PEEK and PEEK-SP surfaces ($p < 0.001$). ALP activity of MC3T3 cells in osteogenic conditions at Day 14 was greater

on TCPS compared to all other surfaces (Growth: Smooth = 0.27 ± 0.08 µmol pNP/hr/µg DNA, SP-250 = 0.05 ± 0.02, SP-350 = 0.06 ± 0.02, SP-450 = 0.06 ± 0.02, Ti6Al4V = 0.13 ± 0.03, TCPS = 0.19 ± 0.07. Osteogenic: Smooth = 3.10 ± 1.31, SP-250 = 0.82 ± 0.11, SP-350 = 1.18 ± 0.35, SP-450 = 0.91 ± 0.40, Ti6Al4V = 2.66 ± 1.02, TCPS = 5.17 ± 2.29) ($p < 0.001$, except smooth PEEK, $p = 0.003$) and was greater for smooth PEEK and Ti6Al4V compared to all PEEK-SP groups (smooth vs. SP-250, $p < 0.001$; smooth vs. SP-350, $p = 0.007$; smooth vs. SP-450, $p = 0.001$; Ti6Al4V vs. SP-250, $p = 0.011$; Ti6Al4V vs. SP-350, $p = 0.070$; Ti6Al4V vs. SP-450, $p = 0.018$) (Figure 4.6). No differences in ALP activity were found under growth conditions ($p > 0.998$). VEGF secretion of MC3T3 cells in growth media was greater on SP-250 compared to TCPS (Growth: Smooth = 392.4 ± 93.0 pg/µg DNA, SP-250 = 507.6 ± 41.7, SP-350 = 453.5 ± 95.7, SP-450 = 430.1 ± 54.0, Ti6Al4V = 293.2 ± 73.5, TCPS = 252.7 ± 61.5. Osteogenic: Smooth = 403.6 ± 327.6, SP-250 = 662.4 ± 131.0, SP-350 = 692.2 ± 80.2, SP-450 = 656.2 ± 62.8, Ti6Al4V = 467.4 ± 86.5, TCPS = 309.7 ± 76.8) ($p < 0.001$, except smooth PEEK, $p = 0.003$) ($p = 0.037$). Likewise, VEGF secretion in osteogenic media was greater on all PEEK-SP groups compared to smooth PEEK and TCPS (smooth vs. SP-250, $p = 0.022$; smooth vs. SP-350, $p = 0.008$; smooth vs. SP-450, $p = 0.040$; TCPS vs. SP-250, $p < 0.001$; TCPS vs. SP-350, $p < 0.001$; TCPS vs. SP-450, $p = 0.001$) (Figure 4.7).

4.4 Discussion

Interest in improving PEEK's osseointegration has accelerated in recent years after numerous reports have described its inability in smooth form to facilitate bone apposition [27-30, 113]. Reasons why this interest persists (as opposed to abandoning PEEK altogether) are often attributed to the other qualities of PEEK that make it favorable in

orthopaedic and spinal applications, mainly its radiolucency, MRI compatibility, high strength, and fatigue resistance. In addition, PEEK's elastic modulus is between that of cortical and trabecular human bone [55, 104] which may result in a lower risk of stress shielding and subsidence in applications such as spinal fusion when compared to other implant materials of the same geometry. We have previously shown that a surface porous PEEK implant facilitated osseointegration while preserving enough of PEEK's mechanical properties to be considered as a material for load-bearing orthopaedic implants [110]. Here we further investigated the PEEK-SP pore structure to compare the mechanical and biological performance of PEEK-SP with varied pore sizes.

Our study has a few limitations. First, percent porosity was not systematically studied and the range of pore sizes tested is rather small and only represents a two-fold difference from the smallest to largest pores. However, the range of pore sizes that we tested are expected to cover the range that is clinically-relevant [55]. Second, many applications can place implants under complex static or cyclic loading environments, such as compression, torsion and, bending (or combinations thereof), that were not tested here. Surface flaws will have the most detrimental effect on the bulk properties in tension, thus, we believe that the data presented here represent a worst-case scenario. However, further work is needed to understand the compressive properties of the surface porous layer. Additionally, all mechanical tests were performed in air at room temperature, but are not likely to deviate from those performed in a more physiologic environment. Third, we have not exclusively singled out pore size as a factor since other parameters also change with pore size (such as layer thickness) (Table 4.1).

We were able to reliably control pore size by selecting the size of salt crystal used as porogen. Reports investigating optimum pore sizes for various tissues generally recommend a pore size of 200-500 μm for bone [108, 114]. Smaller pores may prevent cell infiltration or lead to insufficient vascularization and nutrient transport *in vivo* [55, 115]. Therefore, salt crystal sizes used in this study (200-508μm) were chosen to promote bone ingrowth and create a pore structure favorable for osseointegration. Microstructural characterization also showed that strut morphology parameters (spacing and thickness) were strongly influenced by crystal size, but were again highly consistent within the three groups, suggesting a high level of manufacturing reproducibility and control.

Mechanical characterization showed that pore size has relatively little influence on the mechanical properties of PEEK-SP within the evaluated size range; no differences were found between PEEK-SP of the three different pore sizes. The data demonstrate that although the load-bearing capacity for all pore sizes decreases when using A_T, this is mostly a geometrical effect because their strength approaches that of PEEK-IM when calculated using A_{LB}. However, this will still influence the structural application of the material and is an important consideration in implant design. Tensile tests also revealed that failure strains were decreased to below 50% of PEEK-IM, consistent with previous studies that showed that polymers experience a decrease in failure strain in the presence of notches while the effect on strength is typically marginal [116, 117]. There was no change in modulus with the addition of surface porosity when using A_{LB}. Due to the cyclic loading experienced by orthopaedic implants and the often detrimental decrease in the fatigue resistance of polymers with surface flaws [118-120], it was important to evaluate the fatigue resistance of PEEK-SP. All pore sizes demonstrated a high fatigue resistance at one

million cycles when using A_{LB} despite a decrease in endurance limit from injection molded PEEK. It also appears that, qualitatively, PEEK-SP-450 had a slightly lower fatigue strength than PEEK-SP-250, in agreement with the finding that larger pores initiate more and larger fatigue cracks than small pores and therefore might have a greater effect on the fatigue life [121, 122]. Interfacial shear testing was also performed on PEEK-SP samples to investigate the mechanical integrity between the porous layer and solid core. No difference was found between PEEK-SP samples of different pore sizes. However, all PEEK-SP samples had higher interfacial shear strength than smooth PEEK, suggesting that any bone ingrowth will result in a mechanical interlock providing increased load-bearing area and higher bonding strength than smooth PEEK implants. Altogether, the mechanical properties of surface porous PEEK support its potential to bear physiologic loads with minimal risk of failure. For a clinical loading comparison, lumbar intervertebral discs experience loads of approximately 1000 - 3000 N depending on activity level, which is partially transferred to interbody implants after spinal fusion [123-125]. A simple stress calculation predicts that a PEEK-SP implant under such loading would require 25-80 mm^2 of surface area to remain in the elastic regime and below the fatigue strength at one million cycles (38 MPa). Most common spinal fusion implants exceed this size, lending support for PEEK-SP's use in spinal applications.

In vitro data support the ability of PEEK-SP to facilitate bone cell proliferation and differentiation. At early time points, cells exhibited increased proliferation on PEEK-SP compared to smooth PEEK, Ti6Al4V and TCPS. During this proliferative phase, cells are thought to produce the extracellular matrix proteins required for matrix mineralization [126]. Therefore, the reduced cell proliferation on smooth PEEK, Ti6Al4V, and TCPS

(Figure 4.5) may have caused matrix production and mineralization to occur at later time points in comparison to PEEK-SP (Figure 4.6). This point is further evidenced by the higher ALP activity of cells on smooth PEEK, Ti6Al4V, and TCPS at Day 14 (Figure 4.6), suggesting that the cells and matrix were still preparing for mineralization. This is in contrast to cultures on PEEK-SP that were extensively mineralized by Day 14 and exhibited lower ALP activity levels, which can occur in heavily mineralized cultures and mature bone (Figure 4.6) [58, 126]. This increased mineralization seen in PEEK-SP cultures was clearly cell-mediated and not due to the increased surface area of the porous layer. Additionally, cells grown on TCPS exhibited similar temporal trends in ALP activity and mineralization as in a previous report [112], suggesting that PEEK-SP accelerated osteoblast differentiation rather than smooth PEEK and Ti6Al4V causing delayed differentiation. One potential explanation for the initially increased cell proliferation on PEEK-SP is that the increased surface area effectively decreased the seeding density of cells, which could have facilitated greater cell proliferation at early time points [127, 128]. However, this increase in surface area and early proliferation did not translate to greater cell numbers at later time points (Figure 4.5). Although dynamic culture conditions likely enhanced nutrient transport within the pore layer [129], it is possible that cells on the surface of the porous layer caused more hypoxic conditions for the cells residing within the deeper pores. Although our previous data suggest that nutrient diffusion is not a limitation *in vivo*, where blood vessels are able to perfuse the pore network and allow bone to penetrate the full depth of the pore layer [110], hypoxia is known to influence osteoblast differentiation and endochondral ossification [130, 131]. This hypothesis is supported by

the increased VEGF production of MC3T3 cells on PEEK-SP groups (Figure 4.7), which is known to increase under hypoxic conditions [131, 132].

In this study, we demonstrated that surface porous PEEK can be created with a tunable microstructure. The results show that the introduction of a porous surface layer has the potential to provide an improved clinical outcome for polymeric implants while maintaining adequate load-bearing capacity. Unlike other methods to improve the osseointegration of PEEK implants such as fully porous PEEK scaffolds [78], PEEK-SP retains the bulk mechanical properties necessary for orthopaedic applications while potentially accelerating bone cell proliferation and differentiation compared to smooth PEEK and Ti6Al4V. Therefore, PEEK-SP may offer improved stability and performance over current implants at the critical bone-implant interface. Future studies will investigate the effect of pore size and pore layer depth on functional osseointegration *in vivo* within a preclinical animal model. In addition, further testing is needed to optimize the porosity to account for the tradeoff in bone ingrowth and compressive strength. To predict clinical performance in a spinal fusion application, implants possessing a PEEK-SP surface will undergo biomechanical testing to evaluate insertion force into the intervertebral disc space and the degree of subsidence into the endplates. This technology recently received FDA 510(k) clearance on the COHERE™ Cervical Interbody Fusion Device (Vertera Spine, Atlanta, GA) and clinical data is forthcoming.

CHAPTER 5. POROUS PEEK IMPROVES THE BONE-IMPLANT INTERFACE COMPARED TO PLASMA-SPRAYED TITANIUM COATING ON PEEK

Through CHAPTER 3 and CHAPTER 4 porous PEEK was demonstrated to enhance *in vitro* osteogenic differentiation and *in vivo* osseointegration compared to conventional smooth PEEK surfaces. In this chapter porous PEEK is directly compared to another surface technology designed to overcome the drawbacks of smooth PEEK implants: plasma-sprayed titanium coatings on PEEK.

5.1 Introduction

Achieving clinical success of load-bearing orthopaedic implants remains a significant and multifaceted challenge. Of the many aspects involved, osseointegration is perhaps the most critical and is itself dependent on multiple factors. The clinically oriented definition of osseointegration is more relevant here, described as "a process whereby clinically asymptomatic rigid fixation of alloplastic materials is achieved, and maintained, in bone during functional loading" [133]. Following this definition, an osseointegrated implant should fulfill its function to cohesively transfer physiological loads to surrounding bone and soft tissue without loosening and inducing further complications. Secondary to osseointegration, other, more practical, factors may also contribute to an implant's likelihood of clinical success. These include an implant's medical imaging characteristics, effective stiffness as related to stress shielding of adjacent tissue, and durability during and after implantation. All of these aforementioned clinical performance factors are largely

governed by the material composition and architecture of load-bearing orthopaedic implants.

Polyether-ether-ketone (PEEK) is a high strength semi-crystalline thermoplastic and is one of the most common materials used for load-bearing orthopaedic devices, particularly in spine. First introduced in the medical field in the early 1990s, PEEK has gained widespread acceptance due to its radiolucency on medical images and its lower Young's modulus compared to metals, which can facilitate the design of implants that reduce stress-shielding [27]. Though primarily used in interbody spinal fusion devices, PEEK is also utilized in soft tissue reconstruction, trauma, craniomaxillofacial, and dental applications. However, despite its widespread use, recent reports have demonstrated that conventional smooth PEEK implants can exhibit poor osseointegration and potentially lead to clinical failure [28-30, 37].

The reasons behind the poor osseointegration of current PEEK implants are actively debated. Much of the literature has attributed these poor outcomes to the hydrophobic and chemically inert material properties of PEEK, which has propagated a general perception in the field that PEEK is inherently limited with respect to osseointegration [37, 38, 134]. However, it should be recognized that conventional PEEK implants typically possess a smooth surface due to injection molding or machining processes. Extensive investigation into titanium and other non-PEEK materials have consistently demonstrated that such smooth surfaces provide limited osseointegration compared to roughened and porous surfaces [88, 135-138]. Similar investigations on PEEK surfaces are not as numerous but have begun to support similar conclusions [38, 65, 139]. Indeed, both smooth PEEK and smooth titanium exhibited similarly poor osseointegration compared to more

topographically complex surfaces within the same ovine model and research group [36, 37]. This model and others also support that bone ingrowth into larger scale surface features (e.g. pores) may contribute more to implant fixation compared to smaller micro-scale features (e.g. roughness) due to increased mechanical interlocking. It is likely that both surface composition and surface topography influence osseointegration, yet their relative contributions, particularly regarding PEEK, are still poorly understood [140]. Nevertheless, the high clinical value of PEEK's medical imaging properties and lower elastic modulus have motivated development of multiple different strategies to overcome the poor osseointegration of conventional smooth PEEK implants.

Due to the robust osseointegration response seen with roughened titanium surfaces in the literature, a common method to improve PEEK osseointegration has been to coat PEEK with roughened titanium, often via plasma-spraying. These coatings are typically 100 – 200 μm thick layers of commercially pure titanium and possess a high degree of roughness. Indeed, plasma-sprayed titanium-coated PEEK implants have consistently shown improved osseointegration compared to smooth PEEK and are widely-used clinically [37, 141, 142]. However, even such relatively thin coatings may obscure visualization of the bone-implant interface due to medical imaging artifact. Reports of coating wear and delamination upon implantation are also cause for concern with respect to particle-induced osteolysis and aseptic loosening [141, 143-145]. Thus, ti-coated PEEK implants may improve PEEK implant osseointegration, but possibly at the expense of imaging compatibility and durability.

Another clinically-available alternative to smooth PEEK is porous PEEK. Motivated by the improved osseointegration demonstrated by other porous materials, our

group developed a 100% PEEK structure with 300 – 400 µm porous features to facilitate bone ingrowth and preserve PEEK's favorable medical imaging properties. Our previous work has demonstrated that this porous PEEK structure can withstand relevant physiological and intraoperative loads, facilitate cellular proliferation and osteogenic differentiation, and enhance PEEK osseointegration in preliminary animal studies and clinical case reports [63, 67, 110, 146]. Though previous work supports enhanced osseointegration of porous PEEK, *in vivo* results beyond small-scale preliminary studies have not been published. In particular, no direct comparative studies to other smooth PEEK alternatives have been reported.

The purpose of this investigation was to compare the *in vitro* and *in vivo* performance of porous PEEK and ti-coated PEEK in relation to standard smooth PEEK controls.

5.2 Materials and Methods

5.2.1 Sample Preparation

All samples in this study were made from medical grade Zeniva® 500 PEEK (Solvay Specialty Polymers, Alpharetta, GA). Porous PEEK samples were created as described previously [110]. All ti-coated samples were plasma sprayed with a 0.13 – 0.25 mm thick layer of commercially pure titanium (APS Materials, Inc., Dayton, OH). The average bond strength of the titanium coating to the underlying PEEK substrate was certified to be 25.4 MPa by the vendor. Smooth PEEK samples used for *in vitro* experiments possessed an injection molded surface finish. Smooth PEEK samples used for the *in vivo* experiment possessed a machined surface finish.

In vitro samples were 15.4 mm diameter x 2 mm thick disks designed to press-fit into the bottom of 24-well tissue culture plates. *In vivo* samples were T-shaped cylinders with a bottom diameter of 3 mm and top diameter of 4 mm. Each diameter section measured 2 mm in length for a total implant length of 4 mm. Each implant possessed a 0.75 mm diameter transverse hole through the top section for pull-out testing and contained three orthogonally oriented 0.8 mm diameter titanium beads to aid implant registration during μCT evaluation. The surface of interest was present on the bottom surface of all implants while all other implant faces possessed a machined PEEK surface finish.

All samples were cleaned prior to further investigation by sonication in a 2% aqueous solution of Micro-90 cleaning solution (Cole-Parmer, Vernon Hills, IL). Samples were copiously rinsed in distilled water and allowed to air dry prior to steam sterilization in an autoclave.

5.2.2 Surface Characterization

Representative macro-scale images of each surface were taken at 250x magnification using a digital microscope (VHX-600, Keyence, Itasca, IL). Microcomputed tomography (μCT) was used to characterize the porous structure of porous PEEK samples (n = 12). Scans were performed using a 17.2 μm voxel size, 55 kVp tube voltage, 200 μA tube current, and 215 msec integration time (μCT 50, Scanco Medical, Brüttisellen, Switzerland). Porous PEEK cross-sections were manually contoured tightly to the pores to minimize inclusion of non-porous volume. A global threshold was applied to segment PEEK from pore space and kept consistent throughout all evaluations. Pore morphometrics were evaluated using direct distance transformation methods [82, 83]. Briefly, strut spacing was calculated using a

maximal spheres method adapted from a trabecular spacing index. Porosity was determined by 1–BV/TV, where BV represented polymer volume and TV represented the total contoured volume. Average pore depth was determined using a trabecular thickness index algorithm on the filled TV of each contour. Pore interconnectivity was determined by inverting the segmented porous structure and dividing the largest resulting connected solid volume by the total solid volume. Pore size was determined by measuring the maximum side length of three randomly selected pores from each scan.

Laser confocal microscopy was used to investigate micro-scale topography of each surface (LEXT OLS4000, Olympus, Waltham, MA). Four samples of each surface group were imaged using a 20x objective and 100 nm pitch. Images were analyzed for average surface roughness, Sa, and maximum peak-to-valley height, S_z, after applying a cutoff wavelength, λ_c, of 100 µm. Images of porous PEEK samples were focused on a single, flat pore wall and thus do not account for the larger height variations of the pore struts themselves.

Atomic force microscopy (AFM) was used to quantify the nanotopography of each surface. Porous PEEK samples underwent modified porous processing to minimize pore depth and accommodate the AFM tip. Surface images were acquired with an Asylum Research, Inc. (Santa Barbara, CA) MFP-3D AFM using Bruker (Santa Barbara, CA) NTESPA cantilevers (f0 = 300 kHz, k = 40 N/m, R = 10 nm) and a drive frequency 2 - 5% less than each cantilever's resonance frequency. The drive amplitude was set to maintain a tapping mode amplitude of 80 mV, and a 70 mV amplitude setpoint was used to minimize tip wear while maintaining sufficient force on the surface to stay in contact while imaging large valleys and peaks. All images were scanned at 0.2 Hz and 256 scan lines, and images

were flattened with a second-order polynomial. For each of four samples, between one and six 1.2 μm^2 representative images were collected at different regions on the surface. To assess nanotopography, the 1.2 μm^2 images were analyzed for surface roughness, S_a, and maximum peak-to-valley distance, S_z, within a 1.1 μm^2 area to avoid artifacts at the image boundaries due to piezo hysteresis or image flattening artifacts.

5.2.3 In vitro osteogenic differentiation

In vitro osteogenic differentiation was evaluated on all three surfaces utilizing clonal mouse pre-osteoblast cells (MC3T3-E1, ATCC, Manassas, VA) due to their homogeneity, availability and differentiation profile that is similar to human osteoblasts [112]. Cleaned and sterile disks from each group were press fit into the well bottoms of 24-well tissue culture plates and rinsed with phosphate-buffered saline (PBS) ($+Ca^{2+}/+Mg^{2+}$). MC3T3 cells were seeded on all surfaces at 20,000 cells/cm^2 in growth media composed of α-MEM (Life Technologies, Carlsbad, CA) supplemented with 16.7% fetal bovine serum (FBS) (Atlanta Biologicals, Lawrenceville, GA) and 1% Penicillin-Streptomycin-L-glutamine (PSL, Life Technologies). After three days cells reached confluence and all samples were switched to osteogenic media comprising growth media supplemented with 6 mM β-glycerophosphate, 1 nM dexamethasone, 50 ng/ml thyroxine, 50 μg/ml ascorbic acid 2-phosphate, and 1 nM 1α,25-Dihydroxyvitamin D3 (Sigma, St. Louis, MO). Samples were cultured for 14 days after confluence, changing media every 3 to 4 days. At 14 days media was removed from all samples and stored at -20°C. Samples undergoing assays for alkaline phosphatase (ALP) activity and DNA content were washed with PBS ($-Ca^{2+}/-Mg^{2+}$), ultrasonically lysed in Triton X-100 (0.05% in PBS) and subjected to one freeze-thaw cycle prior to further analysis (n = 5). Samples assayed for calcium were washed with PBS (-

Ca^{2+}/-Mg^{2+}) and vortexed overnight at 4°C in 1 N acetic acid to solubilize calcium (n = 5). ALP activity was determined by colorimetric intensity of cell lysates exposed to p-Nitrophenyl phosphate (pNPP, Sigma, St. Louis, MO) and was normalized to same-well DNA content determined by a Picogreen dsDNA assay (Life Technologies, Carlsbad, CA). Calcium deposition in parallel cultures was determined by a colorimetric Arsenazo III reagent assay (Diagnostic Chemicals Ltd., Oxford, CT). Vascular Endothelial Growth Factor (VEGF) and osteocalcin was measured from culture media and lysate, respectively, at day 14 after confluence using an ELISA and normalized to same-well DNA content (R&D Systems, Minneapolis, MN).

5.2.4 In vivo osseointegration

Osseointegration of each surface was assessed using an established implant plug model in the proximal rat tibia [89, 90]. All surgical procedures were approved by the Institutional Animal Care and Use Committee at the Georgia Institute of Technology (IACUC Protocol No. A16015). All implants were scanned prior to implantation using μCT as described above. A total of 18 male Sprague-Dawley rats were used in this study (Charles River Laboratories International, Inc., Wilmington, MA). Animals were 12 weeks old with a mean body weight of 402 g on the day of surgery. Animals were anesthetized using isoflurane, administered analgesic via a sub-cutaneous injection of sustained release Buprenorphine, and both hind limbs were shaved and prepared using alternating applications of chlorhexidine solution and isopropanol. A 1 cm incision was made over the medial aspect of the proximal tibia and muscle was released from the bone surface surrounding the growth plate and medial collateral ligament (MCL). The MCL was transected and a 2.5 mm biopsy punch (Integra® Miltex®, Plainsboro, NJ) was used to

create a 2.7 mm diameter hole directly below the growth plate and in line with the native MCL path. Each implant was press-fit into the hole such that the lip of the implant rested flush on the tibial cortex. The muscle was sutured over the implant and the skin was closed with wound clips. Animals could recover and ambulate freely following surgery. Each animal received one implant in each leg (n = 12, 36 total implants) and implant groups were randomized between animals, legs, and surgeons. All animals were euthanized 8 weeks after surgery by carbon dioxide asphyxiation. Dissected tibiae were stored at -20°C until further testing.

All samples were thawed and scanned with μCT prior to biomechanical testing (n = 8) and histology processing (n = 4) using the same scan settings as described above. Quantification of mineralized tissue volume within the porous PEEK structure was performed by registering the pre- and post-implantation μCT scans into the same orientation using the three orthogonally oriented titanium beads in each implant as fiducial markers. This procedure was necessary because the PEEK structure was not visible in the post-implantation reconstructions due to the similar attenuation properties of PEEK, water and soft tissue. The contour inscribing the porous region of the pre-scan could then be copied onto the same region of the post-scan to evaluate tissue within the porous structure. A global mineralization threshold of 425 mg HA/cm^3 was used to define mineralized tissue ingrowth, corresponding to 13.4% of the maximum possible gray value (32,767). This value was selected as 45% of the average mineral density of intact cortical bone (944 ± 21 mg HA/cm^3), calculated as the average density of six cortical regions located away from the implant site for three samples in each group. This thresholding method was chosen based on visual agreement with grayscale tomograms and on previous reports supporting

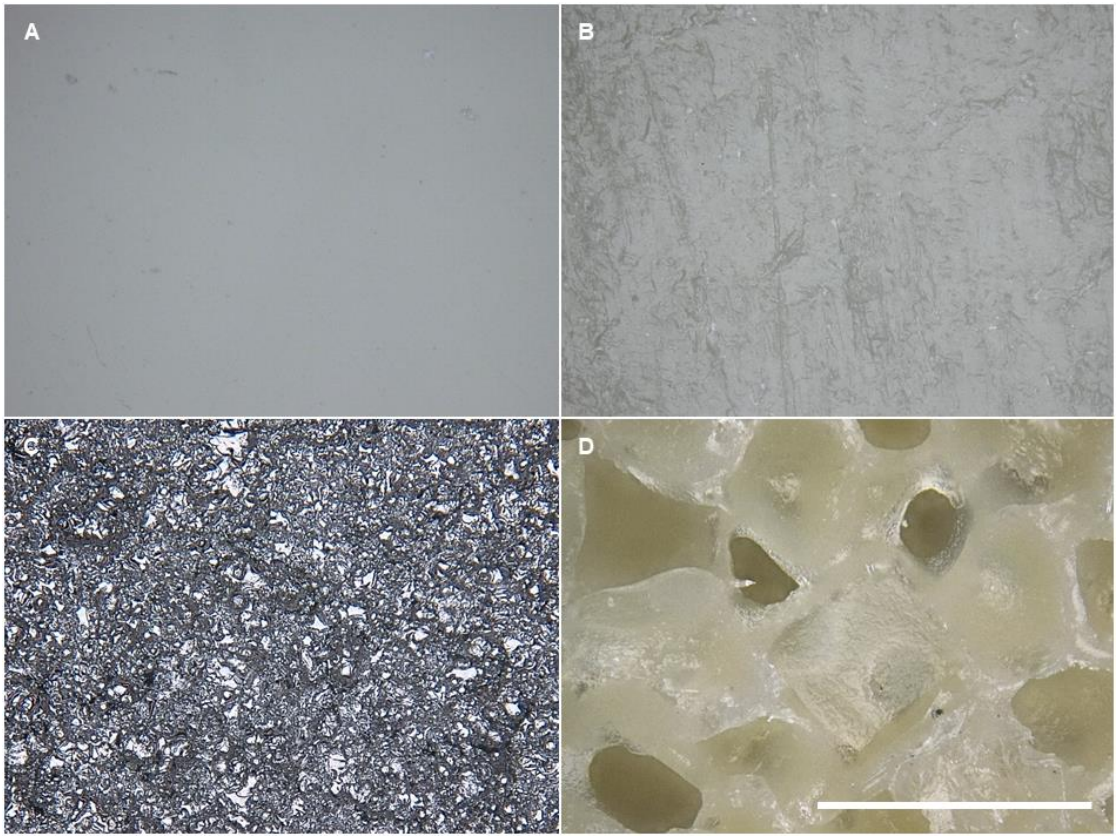

Figure 5.1 - Representative photomicrographs depicting the macro-scale topography of injection molded PEEK (A), machined PEEK (B), ti-coated PEEK (C), and porous PEEK (D). Scale bar is 500 µm.

that this threshold represents the approximate mineral density at which tissue assumes sufficient mechanical properties to contribute to biomechanical fixation [147, 148]. Percent ingrowth, BV/TV_{3D}, was calculated by dividing the volume of mineralized tissue inside the porous region, BV_{3D}, by the total available open pore volume, PV_{3D} (n = 12). Mineral density histograms were also generated for each sample (10 $mgHA/cm^3$ bin size) to further characterize tissue ingrowth.

Samples reserved for histological analysis were fixed in 10% neutral buffered formalin following µCT imaging, dehydrated in ascending grades of ethanol, and cleared

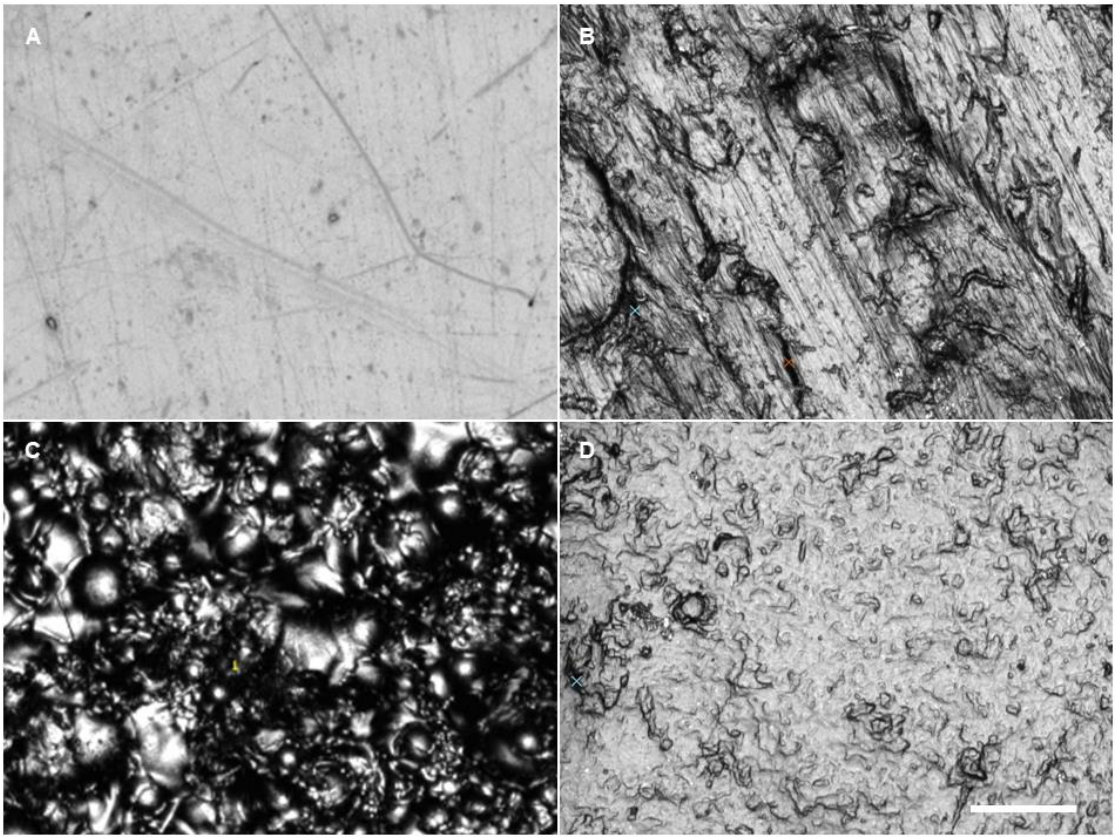

Figure 5.2 - Representative laser confocal microscopy images depicting the micro-scale topography of injection molded PEEK (A), machined PEEK (B), ti-coated PEEK (C), and porous PEEK (D). Scale bar is 50 µm.

in xylene before embedding in methyl methacrylate (MMA). MMA blocks were trimmed on a water-cooled band saw (Mar-med, Inc., Strongsville, OH), sectioned using a Isomet® 1000 Precision Saw (Buehler, Lake Bluff, IL), and ground to 30 µm thick sections on an EXAKT 400 CS grinder (EXAKT Technologies, Inc., Oklahoma City, OK). Sections were stained using Sanderson's Rapid Bone Stain (Dorn & Hart Microedge, Inc., Loxley, AL) with a Van Gieson counterstain (Electron Microscopy Sciences, Hatfield, PA) to distinguish bone (pink) from other soft tissues. Three sections spaced 0.7 – 0.8 mm from each other were cut from each sample and were imaged using an inverted microscope (Eclipse E600, Nikon, Tokyo, Japan) prior to evaluation using ImageJ (NIH, Bethesda,

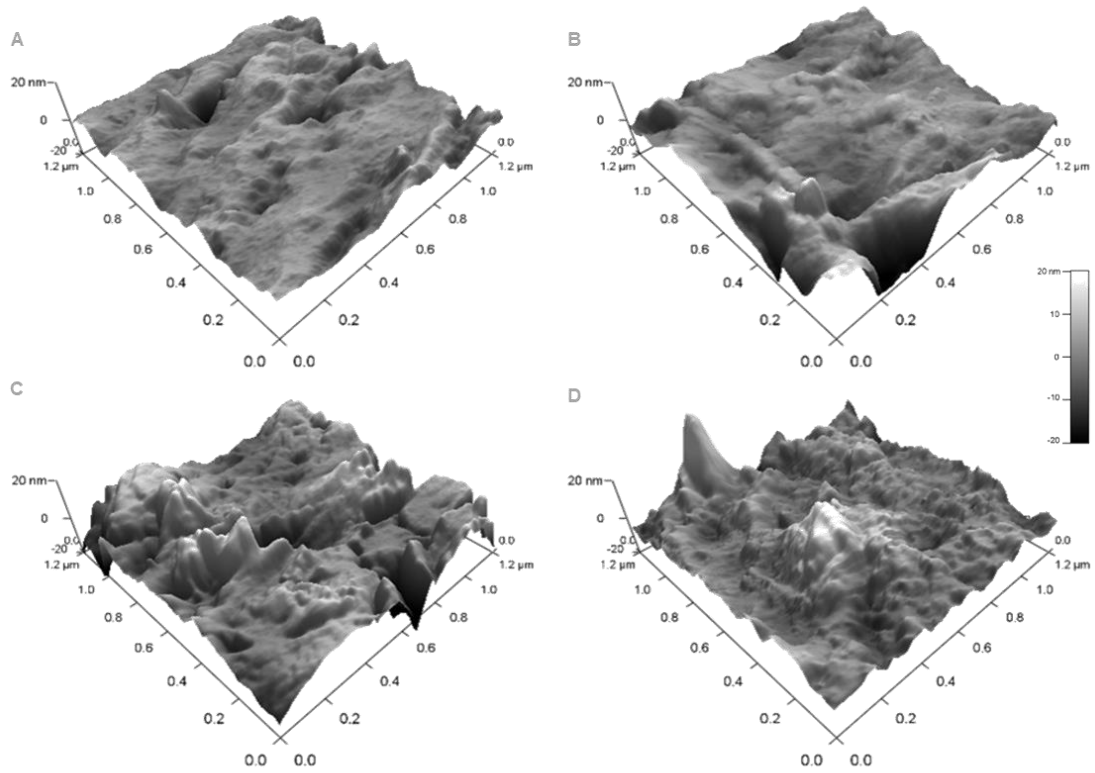

Figure 5.3 - Representative AFM images depicting the nano-scale topography of injection molded PEEK (A), machined PEEK (B), ti-coated PEEK (C), and porous PEEK (D).

MD). Bone ingrowth was calculated by manually contouring bone area, BV_{2D}, and pore area, PV_{2D}, and calculating BV/PV_{2D}. To account for variations in pore boundaries across the thickness of each section (Figure 5.5), the pore areas defined by the inner- and outer-most boundary of each section were averaged and used in the bone ingrowth calculations for each section. Final bone ingrowth values for each sample were calculated as the area-weighted mean of its corresponding three sections. Segmented µCT slices of the same plane as each histological section were similarly evaluated for bone ingrowth, BV/PV_{2D}, and correlated with the results from histology and full-volume 3D µCT ingrowth analysis.

Table 5.1 - Porous PEEK pore morphometrics

Pore Morphometric	Porous PEEK
Porosity (%)	68.7 ± 0.5
Pore Size (μm)	340 ± 8
Strut Spacing (μm)	244 ± 2
Strut Thickness (μm)	114 ± 2
Pore Depth (μm)	523 ± 17
Inter-connectivity (%)	99.96 ± 0.01

Mean +/- SE for all values

Bone-implant contact (BIC) was determined by dividing the length of the bone-implant interface in contact with bone by the total length of the interface using ImageJ. BIC of the pore walls within the porous PEEK architecture was also calculated in a similar manner. Final BIC values for each sample were calculated as the distance-weighted mean of its corresponding sections.

Biomechanical pullout testing was performed to quantify functional osseointegration for each implant surface (n = 8). All pullout tests were conducted using a MTS 858 Mini Bionix II mechanical load frame (MTS Systems, Eden Prairie, MN, USA). Each thawed tibia was secured using a custom fixture and the implant was attached to a 100 N load cell by passing piano wire through the transverse hole of the implant and up to a clamp. Pre-loaded samples (1.0 N) were subjected to a constant tensile load rate of 0.2 mm/sec. The pullout force was the maximum load achieved before implant detachment or failure. Pullout stiffness (N/mm) was calculated as the slope of the linear region of the

Table 5.2 – Surface topography parameters

	Nano-topography		Micro-topography	
	S_a (nm)	**S_z (nm)**	**S_a (µm)**	**S_z (µm)**
Smooth PEEK (injection molded)	2.41 ± 0.42	17.30 ± 3.52	0.10 ± 0.003	3.91 ± 0.67
Smooth PEEK *(machined)*	4.54 ± 0.56	23.13 ± 2.73	0.75 ± 0.09	13.18 ± 1.99
Ti-coated PEEK	10.31 ± 1.65*,#	48.52 ± 7.79*,#	7.02 ± 0.47^	91.50 ± 2.92^
Porous PEEK	8.32 ± 1.25*	37.04 ± 5.24	0.41 ± 0.04	27.04 ± 7.97*

^p<0.05 versus all other groups, *p<0.05 versus injection molded smooth, #p<0.05 versus machined smooth (Student's t-test).

force-displacement curve. Pullout energy (N-m) was calculated as the area under the force-displacement curve up to the maximum load. Pullout force, stiffness, and energy to failure for each sample was then plotted against its respective ingrowth value and tissue mineral density (overall and thresholded) from the full-volume 3D µCT analysis and fit with a linear function.

5.2.5 Statistics

All comparisons between the three groups were analyzed using a one-way analysis of variance (ANOVA) and Tukey post-hoc analysis for pairwise comparisons (95% confidence interval). Linear fits used a standard least-squares linear regression method. All data are expressed as mean ± standard error (SE).

5.3 Results

5.3.1 Surface Characterization

Macroscopic images of each surface are shown in Figure 5.1. Injection molded samples were smooth with minimal detectable surface features. Machined samples exhibited obvious machining marks, but still maintained an overall smooth surface finish. As expected ti-coated samples were visually rough with randomly distributed peaks and valleys. The pores of porous samples were at a noticeably larger length scale compared to the topographical features of the other groups and possessed a slight micro- texturing along the pore walls.

Quantitative μCT analysis of porous PEEK surfaces demonstrated a similar pore morphology to previous reports [67, 110, 146]. Porous PEEK structures possessed a porosity of 68.7 ± 0.5%, pore size of 340 ± 8 μm, strut spacing of 244 ± 2 μm, strut thickness of 114 ± 2 μm, pore depth of 523 ± 17 μm, and interconnectivity of 99.96 ± 0.01% (Table 5.1).

As expected, quantitative microtopographical analysis showed ti-coated PEEK surfaces to be substantially rougher than all other groups ($p < 0.01$ for S_a and S_z). Maximum peak-to-valley height, S_z, was greater for the pore walls of porous PEEK compared to the injection molded smooth surfaces ($p < 0.05$), but not from machined smooth surfaces (Table 5.2 and Figure 5.2). Approaching the nano-scale, ti-coated PEEK surfaces were rougher than both injection molded and machined smooth PEEK surfaces ($p < 0.05$ for S_a and S_z), but not statistically different from the pore walls of porous PEEK. The average nano-roughness, S_a, of porous PEEK was also found to be greater than injection molded

smooth PEEK surfaces ($p < 0.05$) (Table 5.2 and Figure 5.3). Thus, the roughness trends observed as imaging scale is zoomed inward from the micro- to the nano-scale is such that the large roughness difference between ti-coated PEEK and the other surfaces decreases.

5.3.2 In vitro osteogenic differentiation

Calcium content of porous PEEK cultures was greater than smooth PEEK ($p < 0.01$), but was not statistically different from ti-coated PEEK. Levels of osteocalcin and VEGF were also greater for porous PEEK compared to both smooth PEEK and ti-coated PEEK ($p < 0.01$). Interestingly, DNA content of smooth PEEK cultures was greater than porous PEEK ($p < 0.01.$), but neither group was statistically different from ti-coated PEEK. No differences in ALP activity were detected between groups at the 2 week time point ($p = 0.12$). Taken together, these data indicate that cells cultured on porous PEEK surfaces generally exhibited a more differentiated phenotype at 2 weeks than those cultured on smooth PEEK or ti-coated PEEK. No differences were detected between smooth PEEK and ti-coated PEEK for any assays (Figure 5.4).

5.3.3 In vivo osseointegration

All animals recovered from surgery without complication or death prior to euthanasia. Upon dissection, the cortex of one tibia in the porous PEEK group was inadvertently fractured. Additionally, one implant from the smooth PEEK group and ti-coated PEEK group exhibited bone growth up the side of the implant and into the transverse pullout hole, which artificially increased pullout resistance. These three implants were excluded from all biomechanical analyses, resulting in a final sample size of seven for each group. The mineralized tissue ingrowth data point from the porous PEEK sample (35.7%) was

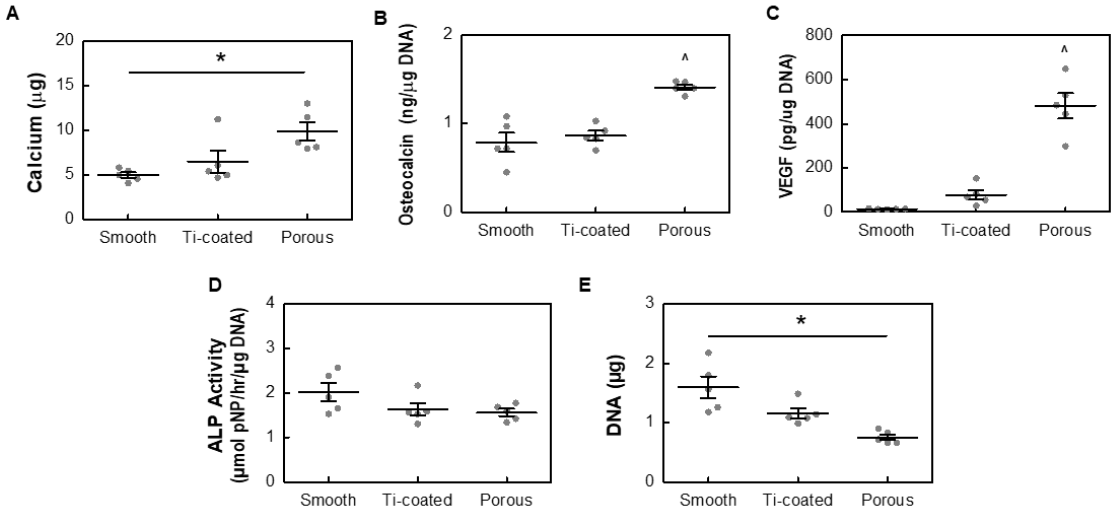

Figure 5.4 - Calcium content (A), osteocalcin (B), VEGF (C), ALP Activity (D), and DNA content (E) of MC3T3 cultures in osteogenic media at 14 days. All data is from identical sample wells, except calcium was from parallel cultures. *p<0.05, ^p<0.05 versus other groups (Two-way ANOVA, Tukey, n = 5). Mean ± SE.

included in the µCT analysis because the fractured cortex was not expected to influence the observed tissue ingrowth at the porous interface. It was also observed that the distance between the implant and growth plate had increased from the time of surgery with the growth of the animals. This placed the implant at the distal margin of the trabecular bone within the proximal tibial metaphysis.

Quantitative µCT analysis demonstrated that 32.8 ± 2.5% of the available pore volume of porous PEEK implants was filled with mineralized tissue (Figure 5.5 and Figure 5.6). Ingrown mineralized tissue had a median mineral density of 616 ± 9 mg HA/cm^3, while a small fraction (3.2 ± 0.7%) exceeded the average density of cortical bone (Figure 5.6). Qualitative observation of smooth PEEK reconstructions showed a thin shell of bone surrounding the implants (Figure 5.5). µCT analysis of ti-coated PEEK samples was

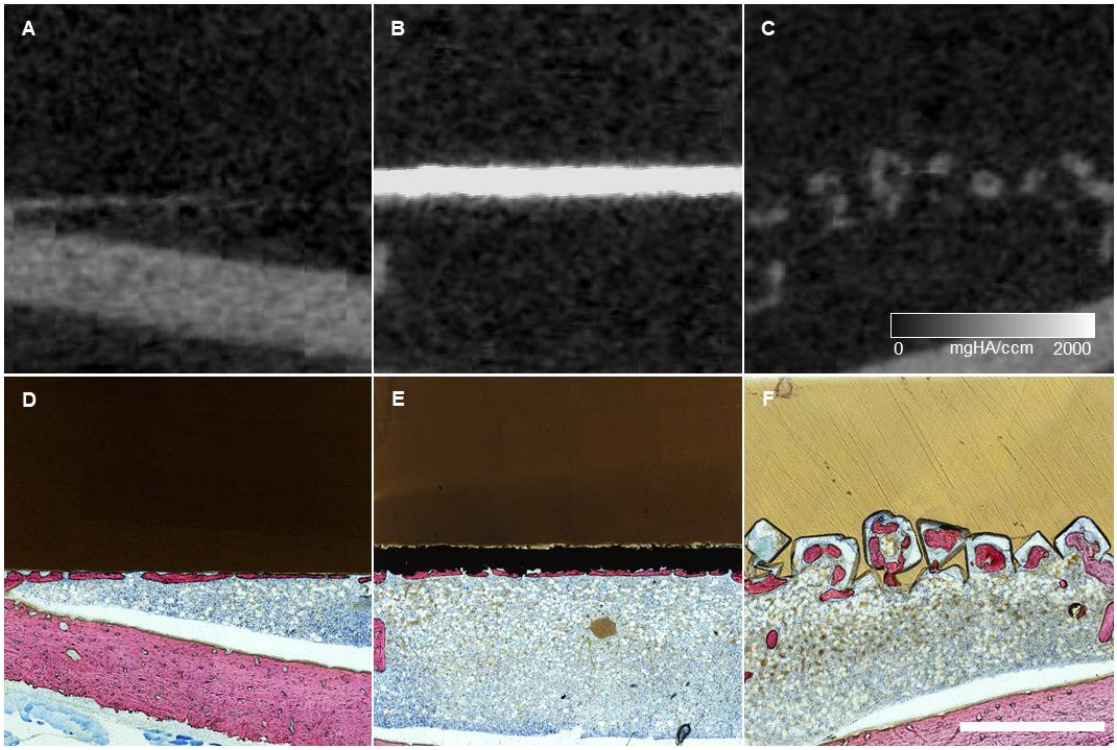

Figure 5.5 - Representative µCT tomograms (A, B, C) and matching histological sections (D, E, F) of the bone-implant interface at 8 weeks for smooth PEEK (A, D), ti-coated PEEK (B, E), and porous PEEK (C, F). The porous PEEK sample in this figure corresponds to the square symbol in Figure 4A and 4B. Grayscale scale bar depicts tissue density as mgHA/cm^3. Length scale bar is 1 mm.

prevented due to imaging artifact from the titanium coating (Figure 5.5). These observations were corroborated by matching histological sections (Figure 5.5).

Bone ingrowth calculations from histological analysis correlated well with mineralized tissue ingrowth calculations from matching 2D µCT slices ($r^2 = 0.75$, $p < 0.01$) (Figure 5.6). The slope of the regression line was 0.91, suggesting that the current µCT analysis method may calculate a slightly lower level of ingrowth compared to histological analysis. However, there was no statistical difference between the three ingrowth evaluation methods (e.g. µCT-3D, µCT-2D, and Histo-2D) (Figure 5.6). Ingrowth was 25.7

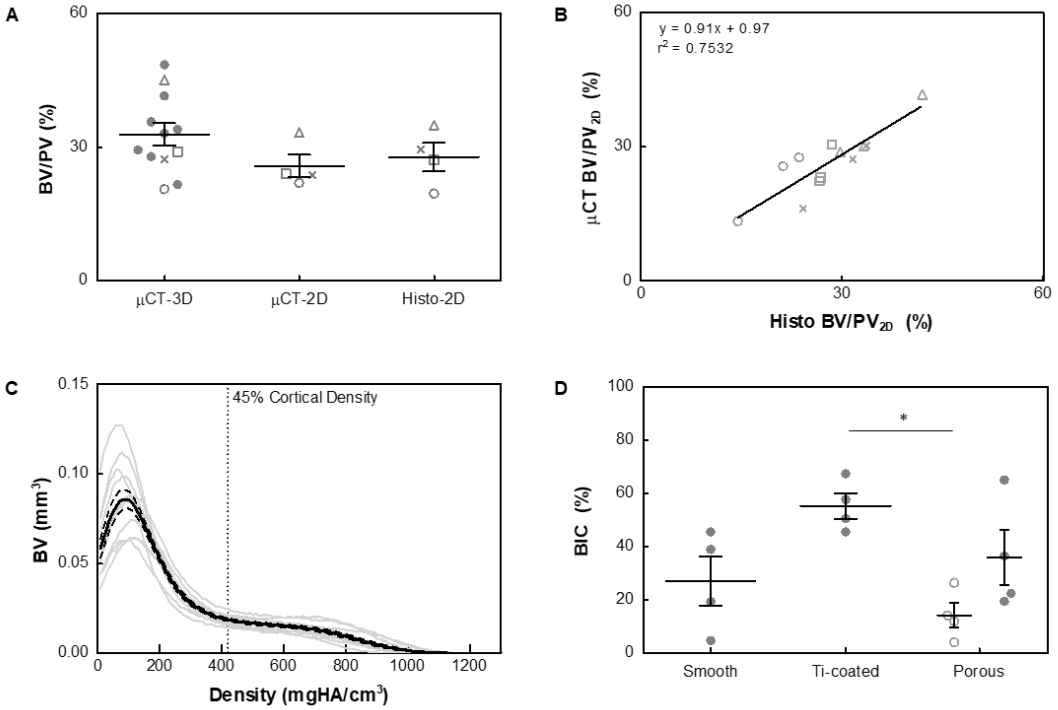

Figure 5.6 - Bone tissue ingrowth evaluation into porous PEEK surfaces using µCT and histological methods. Ingrowth calculations were similar across three different evaluation methods (µCT-3D, µCT-2D and Histo-2D), supporting that µCT analysis is representative of standard histological evaluation (A, B). 3D analysis includes the entire porous surface of each implant, while 2D analysis evaluates the porous regions represented on histological sections. Individual (gray) and mean (black) mineral density histograms of tissue ingrowth into porous PEEK surfaces are shown in (C). Tissue above a threshold of 45% of the global mean cortical bone density was used in µCT ingrowth calculations. BIC at the bone-implant interface (filled circles) was not statistically different between groups, yet the ti-coated PEEK interface exhibited greater bone contact compared to contact along the pore walls of the porous PEEK group (open circles) (D). ^p<0.05 (1-way ANOVA, Tukey). Mean ± SE.

± 2.6% for µCT-2D analysis and 27.8 ± 3.2% for Histo-2D analysis. BIC at the implant interface was not statistically different between ti-coated PEEK (55.3 ± 4.7%), smooth PEEK (27.1 ± 9.3%), or porous PEEK (35.9 ± 10.4%). However, BIC for the ti-coated PEEK interface was greater than the BIC along the pore walls within the porous PEEK architecture (14.2 ± 4.6%).

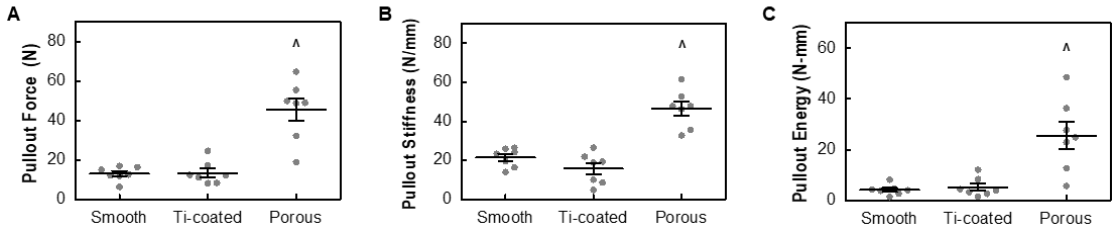

Figure 5.7 - Biomechanical implant pullout test results of smooth, ti-coated and porous PEEK surfaces at 8 weeks. Pullout force (A), stiffness (B), and energy to failure (C) were calculated from the same load-displacement curves. ^p<0.05 versus other groups (One-way ANOVA, Tukey, n = 7). Mean ± SE.

Biomechanical pullout testing resulted in greater pullout force, stiffness and energy to failure for porous PEEK implants compared to both smooth PEEK and ti-coated PEEK groups ($p < 0.01$) (Figure 5.7). Pullout force was 13.1 ± 1.4 N for smooth PEEK, 13.5 ± 2.2 for ti-coated PEEK, and 45.6 ± 5.8 N for porous PEEK. Pullout stiffness was 21.5 ± 1.8 N/mm for smooth PEEK, 15.8 ± 3.0 N/mm for ti-coated PEEK, and 46.4 ± 3.7 N/mm for porous PEEK. Pullout energy was 4.2 ± 0.8 N-mm for smooth PEEK, 5.2 ± 1.4 N-mm for ti-coated PEEK, and 25.6 ± 5.4 N-mm for porous PEEK. No delamination was observed on ti-coated PEEK implants during biomechanical pullout testing. A trend towards positive correlation of mineralized tissue ingrowth with pullout force ($r^2 = 0.35$, $p = 0.16$) and energy to failure ($r^2 = 0.56$, $p = 0.052$) was detected for porous PEEK samples, though the slopes of the fitted lines were not statistically different from zero due to one sample with exceptionally poor mechanical performance for its level of ingrowth. This sample was noted to have a loose fit upon implantation. Exclusion of this sample resulted in fitted lines that were significantly different from zero and better correlated ($r^2 = 0.83$, $p < 0.05$ and $r^2 = 0.89$, $p < 0.01$ for pullout force and energy to failure, respectively) (Figure 5.8).

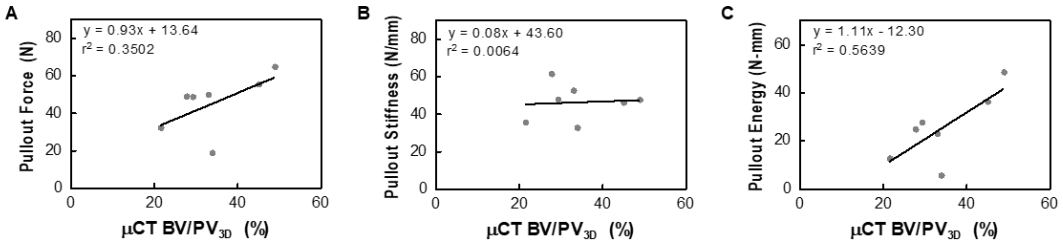

Figure 5.8 - Correlation between mineralized tissue ingrowth and biomechanical implant pullout test results for porous PEEK surfaces at 8 weeks. Pullout force (A), stiffness (B), and energy to failure (C) were plotted against ingrowth values and fit with a linear function.

Pullout stiffness was not correlated with ingrowth with ($r^2 = 0.006$, $p = 0.87$) or without ($r^2 = 0.008$, $p = 0.87$) including the sample in question (Figure 5.8). None of the biomechanics outcomes were correlated with the mineral density of ingrown tissue ($r^2 = 0.12$, $p = 0.39$; $r^2 = 0.006$, $p = 0.85$; $r^2 = 0.28$, $p = 0.18$ for pullout force, stiffness and energy to failure, respectively) (Figure 5.9).

5.4 Discussion

The current study investigated the *in vitro* and *in vivo* bone response to ti-coated PEEK and porous PEEK as two clinically available alternatives to smooth PEEK implants that are used prevalently in load-bearing orthopaedic applications. Overall, porous PEEK was associated with a more differentiated osteoblast phenotype *in vitro* and greater osseointegration *in vivo* compared to smooth PEEK and ti-coated PEEK. Comparing the results from smooth and porous PEEK provides evidence that not all PEEK implants inherently generate a fibrous response, as has previously been suggested [37, 38, 134]. Instead, the current data suggest that surface structure plays a larger role than implant

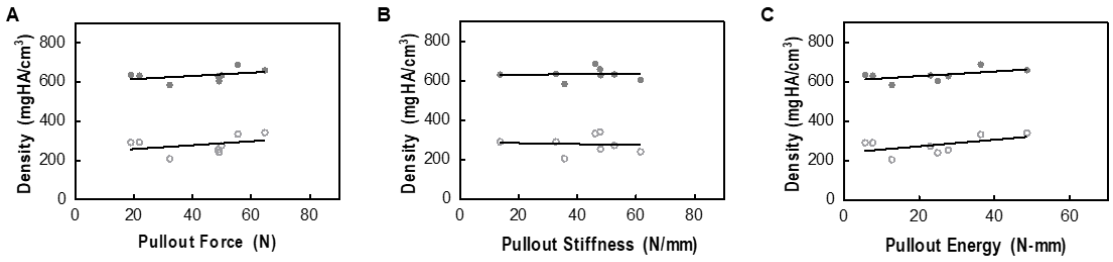

Figure 5.9 - Correlation between biomechanics results and mineral density of overall (open circles) and thresholded (solid circles) tissue ingrowth into porous PEEK surfaces at 8 weeks. No correlation was found between either mineral density and pullout force (A), stiffness (B), and energy to failure (C).

composition, with macro-porous features exhibiting improved functional osseointegration compared to smooth surfaces and micro-roughened surfaces.

In vitro results support that porous PEEK was associated with a more differentiated cell phenotype compared to smooth PEEK and ti-coated PEEK. The primary outcomes supporting this conclusion were the increased mineralization and corresponding osteocalcin production of porous PEEK cultures, both hallmarks of mature, differentiated osteoblasts [58, 126]. The increased mineralization of porous PEEK cultures is corroborated by previous work using the current model, which also demonstrated mineralization to be cell-mediated rather than non-specifically deposited on the surface [67]. Increased VEGF secretion by porous PEEK cultures may be suggestive of hypoxic conditions, possibly due to superficial cells and extracellular matrix restricting nutrient transfer to cells in deeper pores [67]. Hypoxic conditions are known to influence osteoblast differentiation and endochondral ossification [130-132]. However, this effect may differ from the *in vivo* context where nutrient transport would likely be influenced by vascular ingrowth within the pore network. Interestingly, ALP activity was not different between

any surfaces at 14 days post-confluence. Typically regarded as an earlier marker of osteogenic differentiation, low levels of ALP activity may have resulted from the chosen timepoint being too late in the culture maturation timeframe [126]. ALP activity has also been shown to be reduced in more mineralized cultures, which may partially explain these observations [58, 126]. Decreased DNA content of porous PEEK cultures compared to those on smooth PEEK provides further support that cells on porous constructs may have transitioned from a proliferative to a more differentiated state [126]. Similar trends in decreased DNA content on porous versus smooth and roughened surfaces have also been seen with porous titanium structures [136].

Surprisingly, ti-coated PEEK cell cultures did not exhibit signs of enhanced osteogenic differentiation as has been described for other roughened titanium surfaces. A potential explanation is that most rough titanium surfaces in the literature are grit-blasted to possess finer surface features in comparison to the larger "boulder-like" features of plasma-sprayed coatings [37, 48, 149]. Previous cell studies comparing these two rough titanium surfaces have also reported that cells grown on plasma-sprayed titanium coatings exhibit reduced ALP activity and DNA synthesis at early time points and reduced osteocalcin production and mineralization at later time points [48, 150-152]. These results support that, in an *in vitro* environment, cell behavior is sensitive to surface features at multiple length scales. Micro-scale surface features present on grit-blasted surfaces are thought to mimic the natural structure of osteoclast resorption pits and represent a structural stimulus for osteoblast differentiation [48]. Larger, macro-scale porous features with complex curvature could provide different cellular cues related to altered paracrine signaling or mechanical stresses exerted on or generated within cells [114, 153-155].

However, the surface feature size of plasma-sprayed titanium coatings typically falls between those of grit-blasted titanium and macro-scale porous structures, which may have resulted in reduced osteogenic differentiation.

Consistent with previous reports, *in vivo* results also support porous PEEK's ability to facilitate bone ingrowth and improve osseointegration compared to smooth and ti-coated PEEK [146]. Indeed, the level of bone ingrowth demonstrated by porous PEEK here was comparable to the bone ingrowth reported for numerous other porous metallic, ceramic, and polymeric materials including titanium [156], stainless steel [99, 157], cobalt chromium [158], tantalum [79], nitinol [159], silicon nitride [160], polyparaphenylene [161], polysulfone [162], polyethylene [163, 164], and polytetrafluoroethylene [164]. Such pervasive bone ingrowth into porous topographies exhibiting a wide array of material compositions illustrates the central role that surface structure can play in determining functional implant fixation and osseointegration.

Bone growth into an implant surface confers mechanical advantage through interlocking mechanisms, which are influenced by both the size and orientation of surface features. Larger surface features facilitate larger volumes of bone ingrowth and result in larger bearing areas at the bone-implant interface to resist loads [165]. Indeed, the fixation strength of titanium surfaces has previously been shown to increase with increasing feature size, in order from polished, grit-blasted, plasma-spray coated, and porous surfaced [36, 37]. Similarly for the current study, the increased bone volume within the pores of porous PEEK relative to the bone volume between the surface asperities of ti-coated PEEK provided for greater mechanical interlocking and implant fixation. The lack of correlation between tissue density and biomechanics outcomes further supports that increased fixation

of porous PEEK resulted from the increased volume of interlocking bone rather than its mineral density. Thus, implants that facilitate greater volumes of interlocking bone ingrowth (e.g. porous implants) provide for greater implant fixation, regardless of material composition.

The orientation of surface features relative to shear and tensile loads also influences implant fixation. Shear loading of the bone-implant interface of load-bearing orthopaedic implants occurs in dowel-pin, screw-type, and many other applications. Tensile loading can occur in certain applications such as spinal fusion if the device toggles within the disc space during flexion or extension of the spine, or on the surface of total hip stems [99]. Ingrowth into most non-flat surfaces will resist shear loads to some extent due to asperity interference and locking during shear loading. However, resistance to tensile loading requires undercutting features (e.g. pores) to effectively interlock with bone. The ti-coated PEEK surface exhibited few appreciable undercutting features (Figure 5.5) compared to porous PEEK, which may have contributed to such low fixation under tension. Interestingly, this result occurred despite the increased BIC of ti-coated PEEK implants, which suggests that BIC, a standard metric for osseointegration, is a poor indicator of fixation in the absence of interlocking features. In addition to mechanical interlocking, true bone-implant bonding via direct osteoconduction would also contribute to implant fixation. However, the tensile bond strength of bone with polished titanium has been measured to be ~0.01 MPa [166], a negligible contribution compared to standard implant fixation strengths in the 2 – 30 MPa range [36, 37, 99, 156]. Indeed, the concept of "bone bonding" has itself been hypothesized to be a mechanical interlocking phenomenon of the cement line with micro-scale features on biomaterial surfaces during healing [167].

Interlocking features to resist tension have also been hypothesized to improve osseointegration by increasing fibrin clot retention during the early phases of healing. Interlocking of surface features with the fibrin matrix may provide more resistance to the tensile traction forces exerted by cells on the fibrin matrix as they migrate to the implant surface [168]. Detachment of the fibrin matrix could prevent these early stage cells from reaching the surface and facilitating key tissue repair and bone formation processes. This migratory process is typically considered at the scale of microtopography and may partially explain the differences in BIC in relation to the different surface topographies.

The agreement between bone ingrowth analyses from μCT and histology is notable. Histology is the standard method to evaluate bone ingrowth into porous structures. However, histology is a destructive process and only allows for evaluation of a small percentage of each sample, particularly for ground bone sections. For example, the current histology analysis accounts for just 3% of each sample. Conversely, μCT is a non-destructive evaluation method allowing for full volume analysis of each sample. Previous studies support the current findings that μCT and histology produce similarly accurate measures of bone morphology and ingrowth [169, 170]. As clinical imaging technology improves, the ability to perform similar CT ingrowth analysis in patients is alluring. Although the positive correlation between bone ingrowth and implant fixation is not surprising from a biomechanical perspective, it could provide clinical motivation for using imaging to non-invasively monitor bone ingrowth into a radiolucent porous implant to predict functional performance and guide patient rehabilitation. However, the use of this technique for load-bearing orthopaedic applications to date has been limited by imaging artifact induced by porous metallic implants. Indeed, this porous PEEK structure represents

the first clinically available porous technology for load-bearing orthopaedic applications that is radiolucent to facilitate such imaging.

This study has several limitations. First, definitive conclusions regarding the relative importance of surface composition and topography cannot yet be made because neither variable was held constant between the three groups studied here. However, other studies focused on decoupling these variables support that surface topography plays a larger role in osseointegration compared to surface composition [140, 171]. Second, the smooth PEEK surface used for the *in vitro* study was different from the smooth PEEK surface used for the *in vivo* study. Both surface finishes are clinically relevant and Poulsson et al. has shown that the osseointegration of injection molded and machined smooth PEEK is similar [44]. Third, detection of DNA and osteocalcin from the lysate may have been influenced by their binding affinity to mineral deposits that were not solubilized in the lysis buffer [172, 173]. Fourth, µCT analysis of bone ingrowth is influenced by the applied mineral threshold and the accuracy of the scan registration between pre- and post-scans based on the three registration markers. The applied threshold was selected based on visual agreement with grayscale tomograms and on previous reports demonstrating this threshold to isolate tissue with sufficient mechanical properties to contribute to biomechanical fixation. However, others have utilized different thresholds using other justifications. Mineral density histograms in Figure 5.6 illustrate the influence of threshold on bone ingrowth measurements. Lastly, the results of the *in vivo* study may have been influenced by the gradual remodeling of the implant environment towards an epiphyseal setting as the growth plate shifted proximally with time and animal growth. This effect may have

decreased the amount of trabecular bone surrounding the implant over time, which may have decreased observed bone ingrowth into the bottom face of each implant.

5.5 Conclusion

In this study porous PEEK demonstrated improved cellular osteogenic differentiation and increased implant osseointegration compared to smooth PEEK and plasma-sprayed titanium coatings on PEEK. The radiolucency of porous PEEK enabled μCT to be used to establish a direct link between bone ingrowth volume and fixation strength, which could motivate development of non-invasive diagnostic and monitoring techniques as clinical imaging improves. Further, these results illustrate the critical role that bone-implant mechanical interlocking has on implant fixation. Both the size and orientation of surface features contribute to interlocking and should be considered when assessing bone ingrowth and bone-implant contact metrics.

CHAPTER 6. RELATIVE EFFECTS OF SURFACE TOPOGRAPHY AND SURFACE MATERIAL ON PEEK AND TITANIUM OSSEOINTEGRATION

CHAPTER 5 began to provide insight into the relative influence of surface topography and surface chemistry on PEEK implant osseointegration. These results provided convincing evidence that macro-porosity was largely responsible for the favorable osseointegration and implant fixation outcomes of porous PEEK implants. However, multiple surface characteristics were different between smooth PEEK, porous PEEK and ti-coated PEEK surfaces, thereby limiting the ability to attribute osseointegration outcomes to any one variable. In this chapter explicit effort was made to isolate surface topography and material to evaluate their relative influence on the osseointegration of PEEK implants.

6.1 Introduction

Polyether-ether-ketone (PEEK) is a semi-crystalline thermoplastic that is commonly used in load-bearing orthopaedic applications due to its radiolucency and lower Young's modulus compared to titanium and other metals, which can facilitate implant designs to reduce stress shielding [27]. Though primarily used in interbody spinal fusion devices, PEEK is utilized across many orthopaedic disciplines including soft tissue reconstruction, trauma, craniomaxillofacial, and dental applications. Despite its widespread use, reports have demonstrated that conventional smooth PEEK implants can exhibit poor osseointegration in comparison with other common orthopaedic materials such as titanium [28-30, 139]. The poor osseointegration of current PEEK implants is often attributed to

PEEK's hydrophobic and chemically inert surface chemistry. However, the smooth surface topography of conventional PEEK implants also prevents osseointegration by limiting mechanical interlock with apposing bone. Topography and material likely both play a role in PEEK osseointegration, yet their relative contribution remains unclear.

When evaluated in isolation, both surface topography and surface material have been shown to influence implant osseointegration. Rough and porous topographies of various material compositions, including PEEK and titanium, have consistently demonstrated improved osseointegration compared to smooth surfaces of the same material [36, 88, 110, 136, 146, 174-176]. This effect is primarily due to increased mechanical interlocking of surface features with ongrown and ingrown bone. Further, porous surfaces that facilitate larger volumes of bone ingrowth provide for greater mechanical interlocking and implant fixation compared to rough and smooth surfaces [36]. Surface topography may also exert effects at the cellular level, where micro- and nano-scale features mimic the natural topography of osteoclastic pits and macro-scale porous features provide cellular cues related to paracrine signaling and mechanical stresses generated within cells [114, 155].

Investigations into the influence of surface material on osseointegration are less conclusive. Certain studies have reported that titanium surfaces increased osteoblast maturation *in vitro* and led to greater bone-implant contact *in vivo* compared to PEEK for smooth and rough topographies [177, 178]. On the other hand, conflicting studies have demonstrated equivalent *in vitro* outcomes and reported similar levels of bone-implant contact and fixation strength between the two materials [36, 37, 179]. These discrepancies may stem from the difficulty of controlling surface topography across different material

chemistries. Although labeled as simply smooth or rough, different material responses to common surface finishing techniques (e.g. polishing or grit-blasting) can result in different topographies, which may confound results. Consequently, several advanced methods to modify surface material and topography have been investigated, yet independent modification of surface topography and surface material remains difficult [38, 44, 134, 139, 176, 180, 181].

Although absolute control of topography and material is challenging, one of the more promising methods has been to use sub-micron and nano-scale coatings to alter surface material while minimizing topographical changes. These coatings have been used on non-PEEK surfaces to demonstrate that surface topography may play a larger role in implant osseointegration compared to surface material. Hacking et al. coated rough hydroxyapatite (HA) surfaces with a <100 nm thick titanium layer and determined that topography accounted for 80% of the osseointegration response to hydroxyapatite-coated implants. Similarly, Olivares-Navarrete et al. coated smooth and rough titanium surfaces with a ~150 nm layer of graphitic carbon and demonstrated that topography, not material, was the dominant driver of cellular osteogenic differentiation. In contrast, Han et al. indicated that material may still play a role with respect to PEEK osseointegration by demonstrating that smooth PEEK coated with a ~1 μm titanium layer increased bone-implant contact compared to uncoated PEEK surfaces [43].

Thus, there is evidence that both surface topography and surface material play a role in PEEK osseointegration, yet their effect relative to each other is still unclear. Additionally, no studies exist to the authors' knowledge that have investigated the effect of surface material across multiple surface topographies of different length scales, which

may not be constant. For example, the large increases in osseointegration associated with porous surface topographies may outweigh the effect of an altered surface material seen on smooth or rough surfaces [36, 110, 146].

Here we investigated the relative effect of surface material and surface topography on PEEK implant osseointegration. Atomic layer deposition (ALD) was utilized to coat smooth, rough and porous PEEK surfaces with a nano-scale titanium coating to alter surface material while minimizing topographical variations. Osseointegration of coated and uncoated implants of each topography was evaluated in a small animal tibial implant model. The entering hypothesis was two-fold. First, titanium-coated surfaces were expected to exhibit improved osseointegration compared to uncoated PEEK surfaces. Second, the positive effect of the titanium coating was expected to decrease as surface topography increased from smooth to rough to porous.

6.2 Materials & Methods

6.2.1 Sample Preparation

All implants in this study were made from medical grade Zeniva® 500 PEEK (Solvay Specialty Polymers, Alpharetta, GA). Porous surfaces were created as described previously [110]. Briefly, heated PEEK was extruded through the lattice spacing of sodium chloride crystals and leached in water to form pores. Rough surfaces were created by soda-blasting PEEK surfaces with 100 μm sodium bicarbonate media at 0.55 MPa (80 PSI) using a micro-blaster (Comco, Inc., Burbank, CA, USA). Smooth surfaces maintained an as-machined surface finish.

All implants were T-shaped cylinders with a bottom diameter of 3 mm and top diameter of 4 mm. Each diameter section measured 2 mm in length for a total implant length of 4 mm. Each implant possessed a 0.75 mm diameter transverse hole through the top section for pull-out testing and contained three orthogonally oriented 0.8 mm diameter polytetrafluoroethylene beads to aid implant registration during µCT evaluation. The surface of interest was present on the bottom surface of all implants while all other implant faces possessed a machined PEEK surface finish.

All samples were cleaned by sonication in a 2% aqueous solution of Micro-90 cleaning solution (Cole-Parmer, Vernon Hills, IL). Samples were copiously rinsed in distilled water and allowed to air dry. Half of the samples from each group were coated with a ~30 nm thick layer of TiO_2 using atomic layer deposition in a cleanroom environment (ALD NanoSolutions, Boulder, CO, USA). The ALD coating was present on all surfaces of the implant. All samples were steam sterilized in an autoclave prior to implantation.

6.2.2 Surface Topography Characterization

Microcomputed tomography (µCT) was used to characterize the porous structure of uncoated and coated porous PEEK samples (n = 12). Scans were performed using a 25 µm voxel size, 55 kVp tube voltage, 145 µA tube current, and 300 msec integration time (vivaCT, Scanco Medical, Brüttisellen, Switzerland). Porous PEEK cross-sections were manually contoured tightly to the pores to minimize inclusion of non-porous volume. A global threshold was applied to segment PEEK from pore space and kept consistent throughout all evaluations. Pore morphometrics were evaluated using direct distance

transformation methods [82, 83]. Briefly, strut spacing was calculated using a maximal spheres method adapted from a trabecular spacing index. Porosity was determined by 1–BV/TV, where BV represented polymer volume and TV represented the total contoured volume. Average pore depth was determined using a trabecular thickness index algorithm on the filled TV of each contour. Pore interconnectivity was determined by inverting the segmented porous structure and dividing the largest resulting connected solid volume by the total solid volume.

Laser confocal microscopy was used to investigate micro-scale topography of each surface (LEXT OLS4000, Olympus, Waltham, MA). Images were collected using a 20x objective and 100 nm pitch. Images were analyzed for average surface roughness, S_a, after applying a cutoff wavelength, λ_c, of 100 µm (n = 6 -10). Images of porous PEEK samples were focused on a single, flat pore wall and thus do not account for the larger height variations of the pore struts themselves.

Atomic force microscopy (AFM) was used to quantify the nanotopography of each surface. Surface images were acquired with an Asylum Research, Inc. (Santa Barbara, CA) MFP-3D AFM using Bruker (Santa Barbara, CA) NTESPA cantilevers (f0 = 300 kHz, k = 40 N/m, R = 10 nm) and a drive frequency 2 - 5% less than each cantilever's resonance frequency. The drive amplitude was set to maintain a tapping mode amplitude of 80 mV, and a 70 mV amplitude setpoint was used to minimize tip wear while maintaining sufficient force on the surface to stay in contact while imaging large valleys and peaks. All images were scanned at 0.2 Hz and 256 scan lines, and images were flattened with a second-order polynomial. For each of four samples, between one and six 1.2 μm^2 representative images were collected at different regions on the surface. To assess nanotopography, the 1.2 μm^2

images were analyzed for surface roughness, S_a, within a 1.1 μm^2 area to avoid artifacts at the image boundaries due to piezo hysteresis or image flattening artifacts.

6.2.3 Surface Chemistry Characterization

Energy dispersive x-ray spectroscopy (EDS) was used to determine ALD coating coverage using a Hitachi S-3700N Variable Pressure SEM (Hitachi, Ltd., Japan) equipped with an Aztec Energy EDS system (Oxford Instruments plc, United Kingdom). Injection molded and porous surfaces were evaluated as best and worst case topographical scenarios for the ALD coating. The surface chemistry of ALD titanium coatings were investigated further using a Thermo K-alpha X-ray photoelectron spectroscopy (XPS) system (ThermoFisher Scientific, Inc., Waltham, MA, USA). Survey spectra were collected to characterize overall atomic composition, and high resolution scans of C1s, O1s, Ti2p, and Al2p spectra were collected to investigate surface chemical states. Smooth injection molded surfaces were used as representative surfaces to isolate the effect of the ALD coating and to avoid the need to control for artifact generated by the irregular topographies of the rough and porous samples [182, 183].

XPS was also used to investigate possible surface chemistry changes induced during thermal processing of porous PEEK samples. Effort was made to scan regions that were relatively flat and superficial to minimize topography-induced artifact. Attenuated total reflectance Fourier-transform infrared spectroscopy (ATR-FTIR) was conducted using a Nicolet is50 FTIR with Smart iTR Diamond ATR module (ThermoFisher Scientific, Inc., Waltham, MA, USA) as a second method to investigate possible surface chemistry changes induced during porous processing.

6.2.4 Surgery

Osseointegration of each surface was assessed using an established implant plug model in the proximal rat tibia [89, 90, 184]. All surgical procedures were approved by the Institutional Animal Care and Use Committee at the Georgia Institute of Technology (IACUC Protocol No. A16015). All implants were scanned prior to implantation using μCT as described above. A total of 36 male Sprague-Dawley rats were used in this study (Charles River Laboratories International, Inc., Wilmington, MA). Animals were 12 weeks old with a mean body weight of 387 ± 3 g on the day of surgery. Animals were anesthetized using isoflurane, administered analgesic via a sub-cutaneous injection of sustained release Buprenorphine, and both hind limbs were shaved and prepared using alternating applications of chlorhexidine solution and isopropanol. A 1 cm incision was made over the medial aspect of the proximal tibia and muscle was released from the bone surface surrounding the growth plate and medial collateral ligament (MCL). The MCL was transected and a 2.5 mm biopsy punch (Integra® Miltex®, Plainsboro, NJ) was used to create a 2.7 mm diameter hole directly below the growth plate and in line with the native MCL path. Each implant was press-fit into the hole such that the lip of the implant rested flush on the tibial cortex. Blood wicking into the porous surface was observed on porous PEEK and porous titanium implants upon implantation. The muscle was sutured over the implant and the skin was closed with wound clips. Animals could recover and ambulate freely following surgery. Each animal received one implant in each leg (n = 12, 72 total implants) and implant groups were randomized between animals, legs, and surgeons. All animals were euthanized 8 weeks after surgery by carbon dioxide asphyxiation. Dissected tibiae were stored at -20°C until further testing.

All samples were thawed and scanned with μCT prior to biomechanical testing (n = 8) and histological processing (n = 4) using the same scan settings as described above. Quantification of mineralized tissue volume within the porous PEEK structure was performed by registering the pre- and post-implantation μCT scans into the same orientation using the three orthogonally oriented polytetrafluoroethylene beads in each implant as fiducial markers. This procedure was necessary because the PEEK structure was not visible in the post-implantation reconstructions due to the similar attenuation properties of PEEK, water and soft tissue. The contour inscribing the porous region of the pre-scan could then be copied onto the same region of the post-scan to evaluate tissue within the porous structure. A global mineralization threshold of 434 mg HA/cm^3 was used to define mineralized tissue ingrowth, corresponding to 13.6% of the maximum possible gray value (32,767). This value was selected as 45% of the average mineral density of intact cortical bone (965 ± 7 mg HA/cm^3), calculated as the average density of six cortical regions located away from the implant site for eight randomly selected samples. This thresholding method was chosen based on visual agreement with grayscale tomograms and on previous reports supporting that this threshold represents the approximate mineral density at which tissue assumes sufficient mechanical properties to contribute to biomechanical fixation [147, 148]. Percent ingrowth, PV_{3D}, was calculated by dividing the volume of mineralized tissue inside the porous region, BV_{3D}, by the total available open pore volume, PV_{3D} (n = 12). Morphology of mineralized bone ingrowth was quantified using standard trabecular morphology algorithms to calculate trabecular spacing, trabecular thickness, and the surface-to-volume ratio. Mineral density histograms were also generated for each sample (10 mgHA/cm^3 bin size) to further characterize tissue ingrowth. All density calculations

were performed after applying a two voxel peel on the segmented image to minimize partial volume edge effects.

Samples reserved for histological analysis were fixed in 10% neutral buffered formalin following μCT imaging, dehydrated in ascending grades of ethanol, and cleared in xylene before embedding in methyl methacrylate (MMA). MMA blocks were trimmed on a water-cooled band saw (Mar-med, Inc., Strongsville, OH), sectioned using a Isomet® 1000 Precision Saw (Buehler, Lake Bluff, IL), and ground to 30 μm thick sections on an EXAKT 400 CS grinder (EXAKT Technologies, Inc., Oklahoma City, OK). Sections were stained using Sanderson's Rapid Bone Stain (Dorn & Hart Microedge, Inc., Loxley, AL) with a Van Gieson counterstain (Electron Microscopy Sciences, Hatfield, PA) to distinguish bone (pink) from other soft tissues. Sections were imaged using an inverted microscope (Eclipse E600, Nikon, Tokyo, Japan).

Biomechanical pullout testing was performed to quantify functional osseointegration for each implant surface (n = 8). All pullout tests were conducted using a MTS 858 Mini Bionix II mechanical load frame (MTS Systems, Eden Prairie, MN, USA). Each thawed tibia was secured using a custom fixture and the implant was attached to a 100 N load cell by passing piano wire through the transverse hole of the implant and up to a clamp. Pre-loaded samples (1.0 N) were subjected to a constant tensile displacement rate of 0.2 mm/sec. The pullout force was the maximum load achieved before implant detachment or failure. Pullout stiffness (N/mm) was calculated as the slope of the linear region of the force-displacement curve. Pullout energy (N-m) was calculated as the area under the force-displacement curve up to the maximum load. Simple and multiple linear

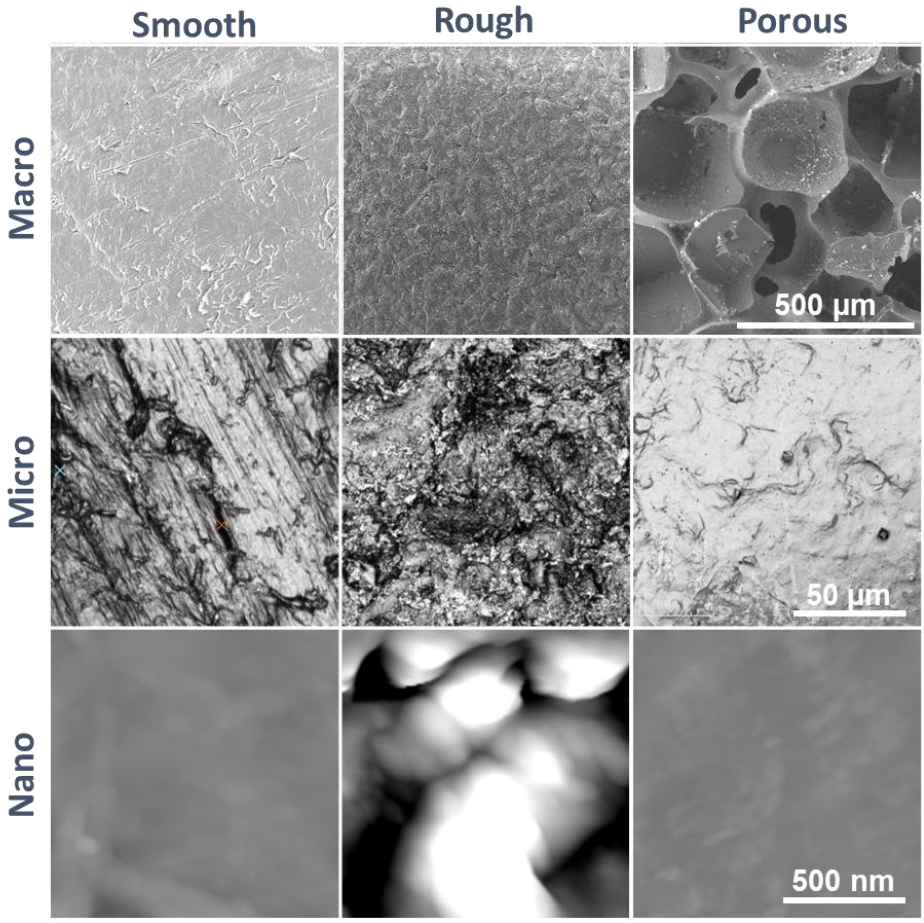

Figure 6.1 – Macro-, micro-, and nano-scale images of smooth, rough and porous PEEK surfaces. Macro-scale topography images are from SEM images. Micro-scale topography images were acquired using laser confocal microscopy. Nano-scale topography images were acquired using AFM.

regression was used to detect the predictive ability of mineralized tissue ingrowth volume and tissue ingrowth density (overall and mineralized) in determining pullout force, stiffness, and energy to failure.

Table 6.1 - Porous PEEK and porous titanium pore morphometrics

	Porosity (%)	Strut Spacing (µm)	Strut Thickness (µm)	Pore Depth (µm)	Inter-connectivity (%)
Porous PEEK	71.7 ± 0.7	263 ± 2	115 ± 2	775 ± 10	99.9 ± 0.002
Porous Titanium	71.0 ± 0.6	259 ± 2	118 ± 3	756 ± 18	99.9 ± 0.004
p-value	0.50	0.30	0.41	0.35	0.59

Mean +/- SE for all values. Student's t-test.

6.2.5 Statistics

Comparisons between groups for nano- and micro-topography characterization, bone ingrowth evaluation, and biomechanics analysis were conducted using a two-way analysis of variance (ANOVA) and Bonferroni post-hoc analysis for pairwise comparisons (95% confidence interval). Comparisons between coated and uncoated porous groups for pore morphometrics and tissue density results were conducted using a Student's t-test (95% confidence interval). Linear fits used a standard least-squares linear regression method. Multiple regression analysis was performed using Minitab software (State College, PA, USA). All other statistical analysis was performed using GraphPad Prism software (La Jolla, CA, USA). All data are expressed as mean ± standard error (SE).

6.3 Results

6.3.1 Surface Topography Characterization

Macro-, micro-, and nano-scale images of each surface from the *in vivo* study are shown in Figure 6.1. Porous surfaces possessed evident macro-scale pores and slight nano- and

Table 6.2 – Surface topography parameters

	Smooth			Rough			Porous		
	PEEK	Titanium	p-value	PEEK	Titanium	p-value	PEEK	Titanium	p-value
Micro-roughness, S_a (µm)	0.73 ± 0.04	0.80 ± 0.05	0.91	1.36 ± 0.06	0.76 ± 0.01	<0.01	0.47 ± 0.10	0.47 ± 0.04	>0.99
Nano-roughness, S_a (nm)	4.54 ± 0.56	7.61 ± 0.63	0.18	38.92 ± 1.43	10.59 ± 0.66	<0.01	8.32 ± 1.25	13.64 ± 1.12	<0.01

Mean +/- SE for all values. Student's t-test

micro-texturing of the pore walls. Rough surfaces were devoid of macro-scale surface features, but exhibited substantial micro- and nano-scale texture. Smooth samples appeared to be relatively smooth at the macro- and nano- scale, yet possessed distinct machining marks at the micro-scale.

Quantitative µCT analysis of porous surfaces demonstrated a similar pore morphology to previous reports, although porosity was slightly greater in the current study [24, 25, 27]. No differences were detected between porous PEEK and porous titanium surfaces for any pore morphometric (Table 6.1). Percent porosity was 71.7 ± 0.7% for porous PEEK and 71.0 ± 0.6% for porous titanium ($p = 0.50$). Strut spacing was 263 ± 2 µm for porous PEEK and 259 ± 2 µm for porous titanium ($p = 0.30$). Strut thickness was 115 ± 2 µm for porous PEEK and 118 ± 3 µm for porous titanium ($p = 0.41$). Pore depth was 775 ± 10 µm for porous PEEK and 756 ± 18 µm for porous titanium ($p = 0.35$). Interconnectivity was 99.99 ± 0.002% for porous PEEK and 99.98 ± 0.004% for porous titanium ($p = 0.59$).

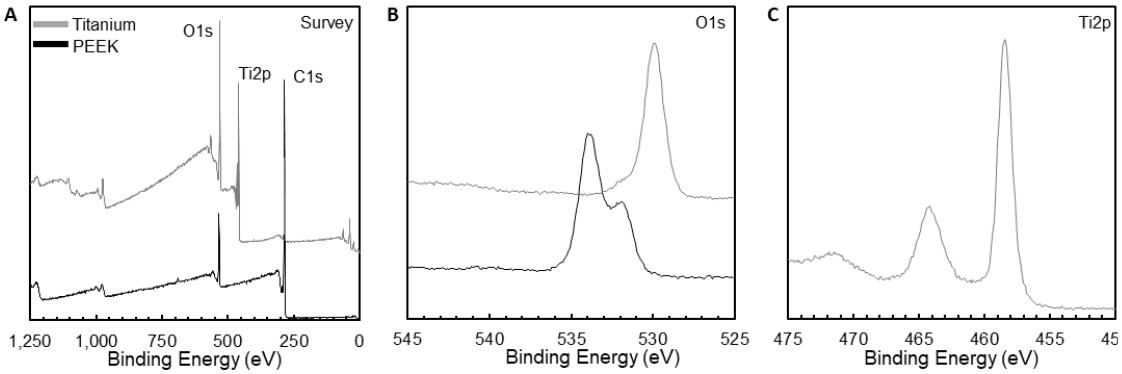

Figure 6.2 – XPS spectra comparing uncoated PEEK (black line) and TiO_2 ALD coated PEEK (gray line) surface chemistry. (A) Survey, (B) O1s, (C) Ti2p.

Quantitative analysis of micro-topography using laser confocal microscopy confirmed qualitative observations (Table 6.2). Average surface micro-roughness, S_a, was: 0.73 ± 0.04 µm for smooth PEEK and 0.80 ± 0.05 µm for smooth titanium; 1.36 ± 0.06 µm for rough PEEK and 0.76 ± 0.01 µm for rough titanium; 0.47 ± 0.10 µm for porous PEEK and 0.47 ± 0.04 µm for porous titanium. The titanium coating not significantly affect the micro-roughness of the smooth or porous surfaces, but roughened surfaces were smoother following the coating process.

Quantitative analysis of nano-topography using atomic force microscopy revealed a similar smoothing effect on the rough surfaces. Porous surfaces experienced a small but significant increase in roughness at the nano-scale.

6.3.2 Surface Chemistry Characterization

XPS analysis of titanium surfaces showed a clear TiO_2 chemistry on the survey, O1s and Ti2p spectra [185] (Figure 6.2). EDS analysis demonstrated the uniformity of the titanium coating on smooth and porous topographies (Figure 6.3). The strong carbon signal was

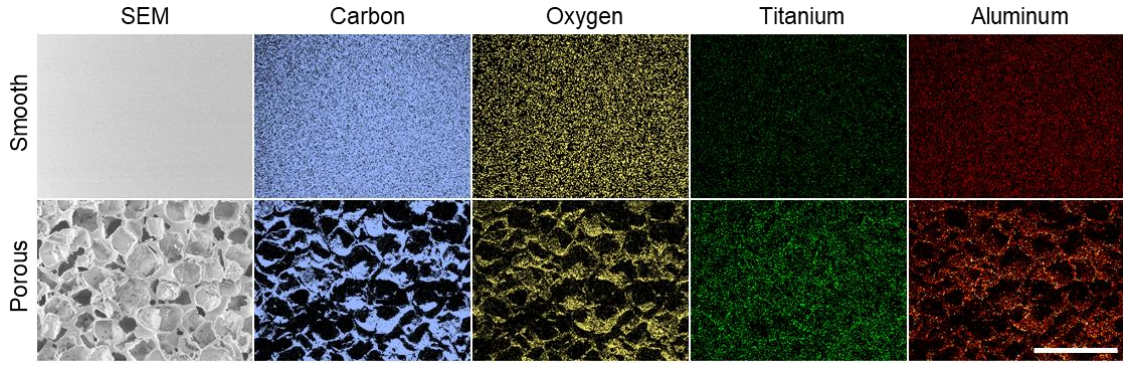

Figure 6.3 - EDS images of the atomic distribution of TiO_2 ALD coatings on smooth and porous PEEK surfaces.

likely due to signal from the underlying PEEK substrate and adventitious carbon contamination. The oxygen signal was contributed to by the PEEK substrate and TiO_2 surface layer.

XPS survey spectra revealed similar profiles between smooth PEEK and porous PEEK surfaces (Figure 6.4). However, high resolution scans of the O1s spectra exhibited minor variations in ether (533.9 eV) and ketone (531.8 eV) peaks (Figure 6.4). These results may be suggestive of surface oxidation during porous processing. ATR-FTIR scans revealed similar spectra between smooth and porous PEEK, suggesting that any surface chemistry variation that may exist was limited to the first several nanometers of the surface.

6.3.3 In vivo osseointegration

All animals recovered from surgery without complication or death prior to euthanasia. Upon dissection, one of the smooth titanium implants was found to be out of the bone and loose in the surrounding soft tissue. No analysis was performed on this sample and no observations were made during the study to suggest a cause for this to occur. The sample

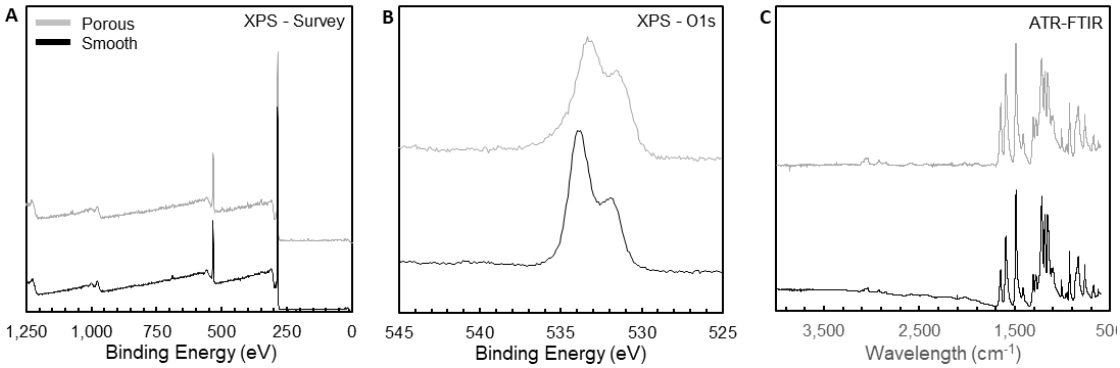

Figure 6.4 - XPS and ATR-FTIR spectra comparison between unmodified smooth PEEK (black lines) and porous PEEK (gray line). XPS survey scan (A), XPS O1s scan (B), and ATR-FTIR spectra (C).

was noted to have a tight press fit during implantation. Another smooth titanium implant and one smooth PEEK implant exhibited substantial bone growth up the side of the implant and into the transverse pullout hole, which exaggerated the measured implant fixation. These two samples were excluded from all biomechanics analyses. For one porous PEEK implant and one porous titanium implant, the piano wire experienced slipping during pullout testing, which artificially increased the area under the load-displacement curve. These samples were excluded from energy-to-failure calculations, but were included in all other analyses.

Quantitative μCT analysis demonstrated that mineralized tissue ingrowth, BV/PV_{3D}, was 38.9 ± 2.8% for porous PEEK and 30.7 ± 3.3% for porous titanium ($p = 0.07$) (Figure 6.5). The density of overall tissue ingrowth and mineralized tissue ingrowth within porous PEEK implants (309 ± 13 and 758 ± 4 $mgHA/cm^3$) was not different from that of porous titanium implants (284 ± 14 and 752 ± 7 $mgHA/cm^3$) ($p = 0.22$ and 0.44, respectively). However, the overall shape of the tissue ingrowth density histogram for

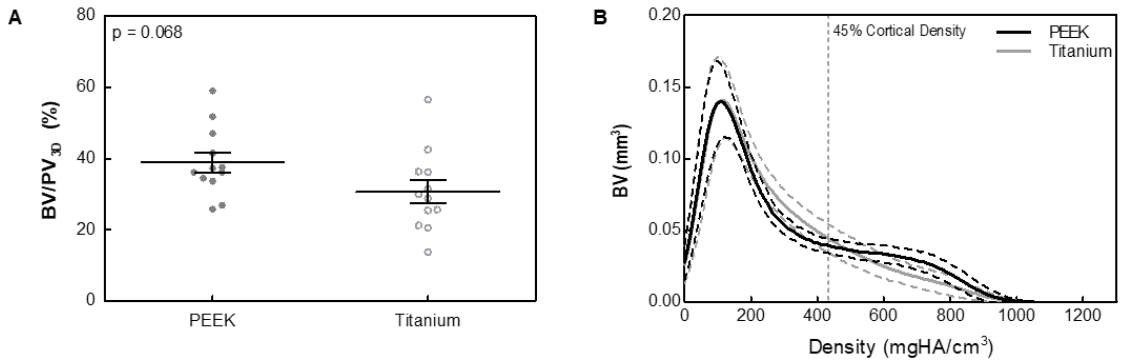

Figure 6.5 - Bone tissue ingrowth evaluation into porous PEEK and titanium surfaces from µCT analysis (A). Mean mineral density histograms of tissue ingrowth into porous PEEK (black line) and porous titanium (gray line) surfaces are shown in (B). Dotted lines represent the standard deviations. Tissue above a threshold of 45% of the global mean cortical bone density was used in µCT ingrowth calculations. Student's t-test. Mean ± SE.

porous PEEK possessed a higher density shoulder region to the right of the 434 mgHA/cm^3 threshold compared to porous titanium (Figure 6.5). Interestingly, porous titanium implants possessed greater volumes of lower density tissue ingrowth in the 200 – 400 mgHA/cm^3 range compared to porous PEEK ($p < 0.01$).

Qualitative analysis of µCT tomograms and matching histological sections showed that bone ingrowth within porous titanium surfaces primarily consisted of thin bone shells that conformed to the pore walls, leaving the center of most pores devoid of bone (Figure 6.6). In contrast, bone ingrowth within porous PEEK was greater in the center of pores with periodic contact with pore walls. These qualitative observations were supported by quantitative morphological analysis of the mineralized tissue ingrowth for each surface using µCT. Mineralized tissue ingrowth of porous titanium exhibited a significantly greater trabecular spacing index ($p < 0.05$) and surface-to-volume ratio ($p < 0.01$) compared to porous PEEK, which supports the thin, dispersed morphology observed. Conversely,

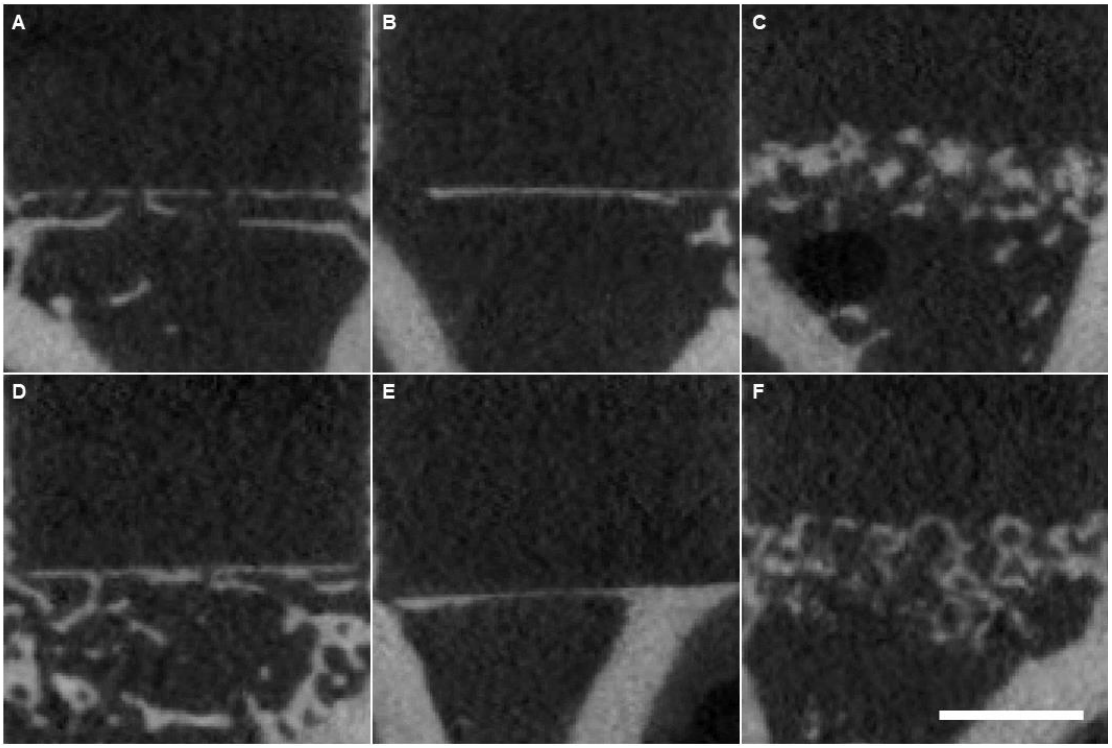

Figure 6.6 - Representative µCT tomograms of the bone-implant interface at 8 weeks for smooth (A, D), rough (B, E), and porous (C, F) surface topographies. Each topography was implanted possessing its native PEEK surface chemistry (A, B, C) or TiO_2 ALD surface chemistry (D, E, F). Length scale bar is 1 mm.

mineralized tissue ingrowth within porous PEEK implants possessed a significantly greater trabecular thickness index ($p < 0.01$) compared to porous titanium, which supports the thicker protrusions observed within porous PEEK implants. Smooth and rough surfaces showed a thin shell of bone surrounding the implants. Qualitatively, greater bone apposition was observed for rough surfaces compared to smooth surfaces and for titanium surfaces compared to PEEK surfaces (Figure 6.7). This observation was confirmed through bone-implant contact analysis, which demonstrated that titanium coated groups resulted in an overall increase in bone implant contact (Figure 6.8).

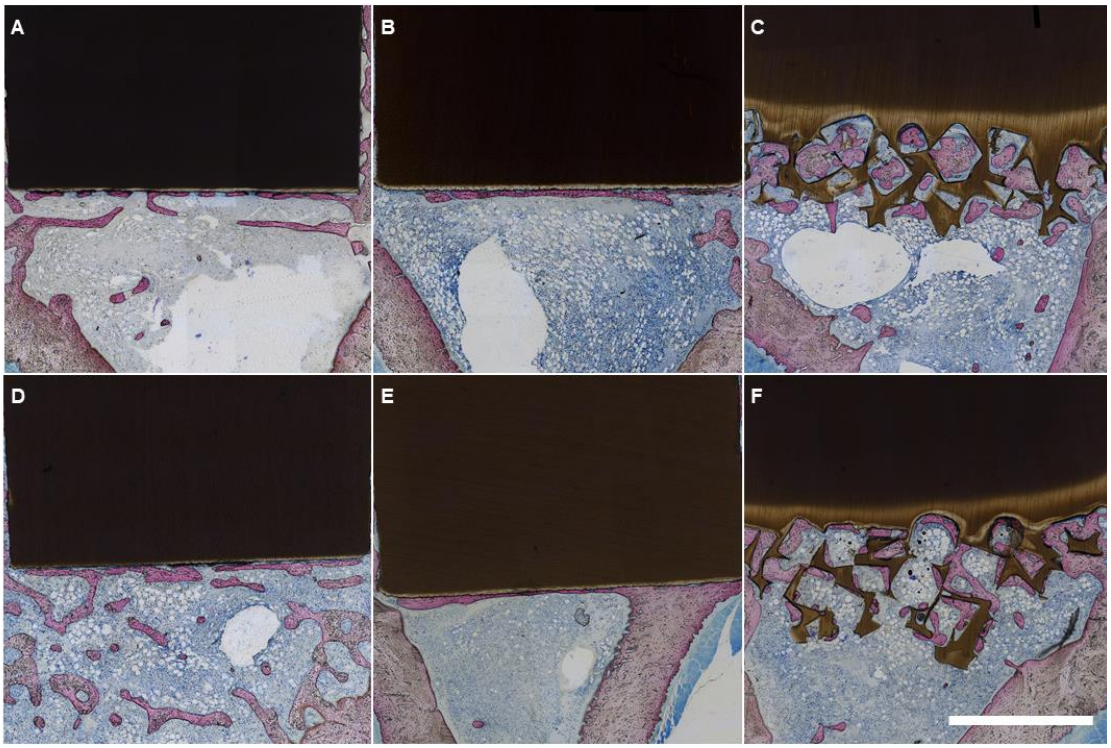

Figure 6.7 - Representative histological sections of the bone-implant interface at 8 weeks for smooth (A, D), rough (B, E), and porous (C, F) surface topographies. Each topography was implanted possessing its native PEEK surface chemistry (A, B, C) or TiO_2 ALD surface chemistry (D, E, F). Length scale bar is 1 mm.

Histological and μCT observations were corroborated by biomechanics outcomes. Across all groups both surface material and surface topography had a significant overall effect on all biomechanics outcomes ($p < 0.05$). Surface topography accounted for 66.16%, 43.93%, and 54.62% of the total variance for pullout force, stiffness, and energy to failure. In contrast, surface material accounted for 6.53%, 9.81%, and 5.23% of the total variance of the same respective outcomes. No interaction between surface material and topography was detected for pullout force ($p = 0.17$), stiffness ($p = 0.38$), or energy to failure ($p = 0.81$). For pairwise comparisons, there was no significant difference in any biomechanics outcomes between surfaces possessing the same surface topography with different surface

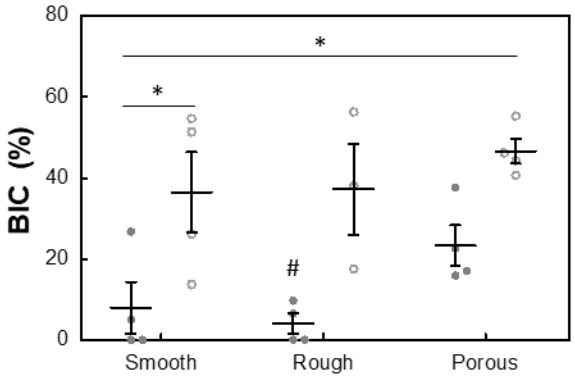

Figure 6.8 – Bone-implant contact for smooth, rough and porous surfaces possessing either PEEK (solid circles) or titanium (empty circles) surface chemistry. (Two-way ANOVA, Tukey, n = 7). Mean ± SE.

material ($0.14 < p < 0.99$ for all comparisons). Interestingly, rough implants did not exhibit an increase in any biomechanics outcome compared to smooth implants of the same surface material ($p > 0.99$ for all comparisons). Overall, both porous PEEK and porous titanium exhibited increases in all biomechanics outcomes compared to all smooth and rough implants regardless of surface material ($p < 0.05$), with the exceptions that pullout stiffness and energy to failure of porous PEEK was not statistically different than smooth titanium implants ($p = 0.07$ and 0.06, respectively) and the pullout stiffness of porous titanium implants was not different than rough titanium implants ($p = 0.64$). Lastly, rough titanium implants exhibited greater pullout force ($p < 0.01$) and stiffness ($p < 0.05$), but not energy to failure ($p > 0.99$), compared to smooth PEEK; however, rough PEEK did not exhibit any differences compared to smooth titanium ($p > 0.99$ for all comparisons).

Pullout force was: 7.5 ± 0.9 N for smooth PEEK and 19.9 ± 3.5 N for smooth titanium; 14.3 ± 2.2 N for rough PEEK and 25.9 ± 2.9 N for rough titanium; 44.2 ± 3.6 N for porous PEEK and 45.8 ± 4.5 N for porous titanium. Pullout stiffness was: 34.5 ± 5.1

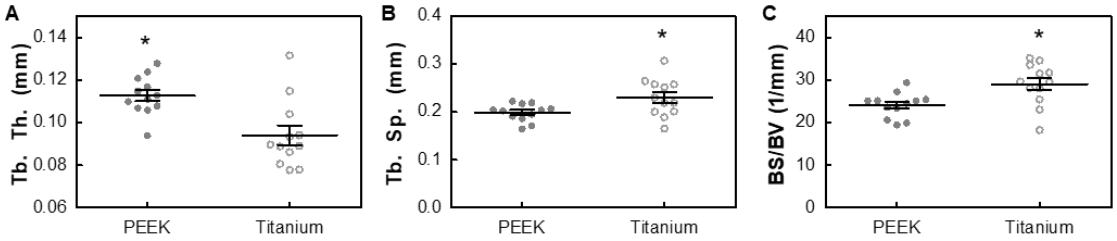

Figure 6.9 – Morphological characterization of mineralized tissue ingrowth into porous PEEK and porous titanium surfaces. µCT analysis was used to calculate trabecular thickness (A), trabecular spacing (B), and bone surface-to-volume ratio (C) parameters. *p < 0.05, Student's t-test. Mean ± SE.

N/mm for smooth PEEK and 48.8 ± 8.4 N/mm for smooth titanium; 42.5 ± 6.6 N/mm for rough PEEK and 63.0 ± 4.1 N/mm for rough titanium; 73.2 ± 5.3 N/mm for porous PEEK and 78.8 ± 3.4 N/mm for porous titanium. Pullout energy to failure was: 1.3 ± 0.3 N-mm for smooth PEEK and 6.7 ± 1.5 N-mm for smooth titanium; 3.2 ± 0.6 N-mm for rough PEEK and 6.5 ± 1.3 N-mm for rough titanium; 16.1 ± 2.6 N-mm for porous PEEK and 18.8 ± 4.0 N-mm for porous titanium.

Mineralized tissue ingrowth, BV/PV_{3D}, was positively correlated with pullout force for porous PEEK ($r^2 = 0.67$, $p < 0.05$) and porous titanium ($r^2 = 0.62$, $p < 0.05$); however, it was not significantly correlated with pullout stiffness ($p_{PEEK} = 0.19$, $p_{Titanium} = 0.08$) or energy to failure ($p_{PEEK} = 0.06$, $p_{Titanium} = 0.44$) (Figure 6.11). Overall ingrowth density was also positively correlated with pullout force for porous PEEK ($r^2 = 0.64$, $p < 0.05$) and porous titanium ($r^2 = 0.68$, $p < 0.05$), but not stiffness ($p_{PEEK} = 0.16$, pTitanium = 0.051) or energy to failure ($p_{PEEK} = 0.09$, $p_{Titanium} = 0.35$). In fact, mineralized tissue ingrowth and overall ingrowth density were well correlated with each other for both porous materials ($r^2 > 0.96$, $p < 0.001$) with the regression line for porous titanium being downward-shifted

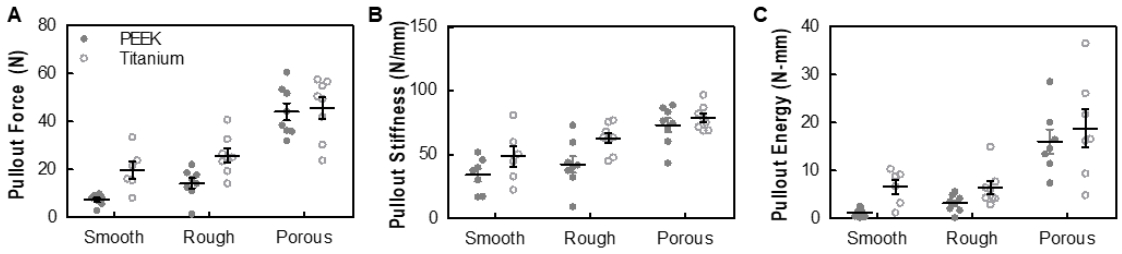

Figure 6.10 - Biomechanical implant pullout test results of smooth, rough and porous PEEK surfaces possessing PEEK or titanium surface chemistry at 8 weeks. Pullout force (A), stiffness (B), and energy to failure (C) were calculated from the same load-displacement curves. ^p<0.05 versus other groups (Two-way ANOVA, Tukey, n = 7). Mean ± SE.

compared to porous PEEK ($p < 0.001$). Interestingly, the slopes of all regression lines correlating tissue ingrowth characteristics with biomechanics outcomes were not different between porous PEEK and porous titanium. No significant effects were detected from multiple regression analysis. This result was partly due to the multicollinearity of mineralized tissue ingrowth and overall ingrowth density (VIF > 30).

6.4 Discussion

PEEK is often used in load-bearing orthopaedic applications for its radiolucency and favorable mechanical properties, yet the factors that influence PEEK implant osseointegration are still poorly understood. Both the surface material and surface topography of implants made from PEEK and other materials have previously been shown to influence implant osseointegration, yet few studies have investigated the effects of each factor in relation to each other. Here we investigated the relative effects of surface topography and surface material on the osseointegration of implants that possessed smooth, rough and porous topographies and displayed either PEEK or titanium surface material. Through biomechanics, histology and µCT analyses, the overall hypothesis was

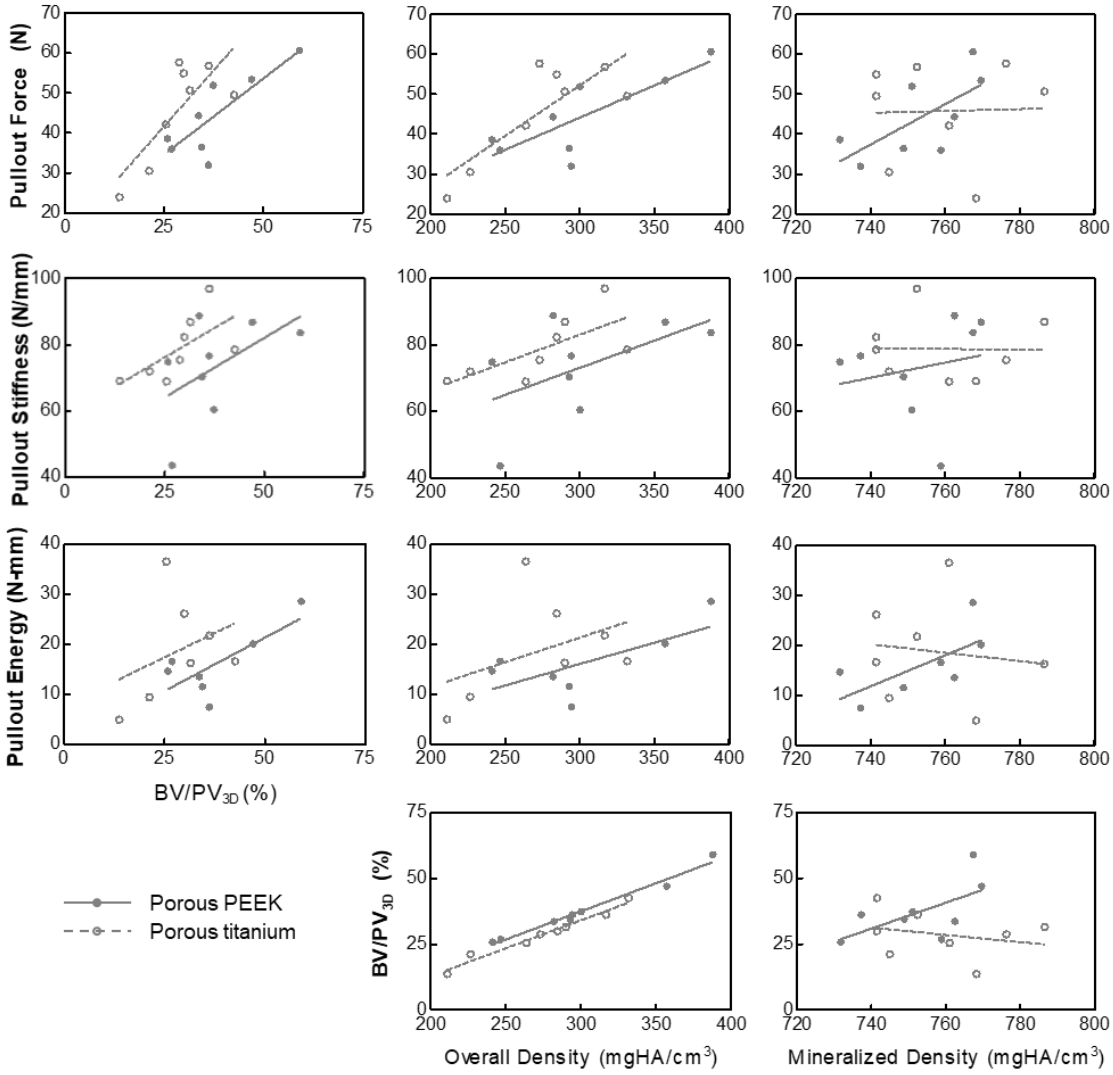

Figure 6.11 - Correlations between biomechanics outcomes and tissue ingrowth volume and density for porous PEEK (solid circles) and porous titanium (open circles).

confirmed and the data suggest that surface topography played a greater role in implant osseointegration compared to surface material, with porous topographies exhibiting the strongest osseointegration response.

Implant fixation is influenced by mechanical interlocking and adhesive forces at the bone-implant interface. In the absence of meaningful surface features with which to interlock, adhesive forces would be expected to dictate implant fixation. The increased fixation of smooth and rough titanium implants compared to PEEK implants in this study suggests that titanium had either greater bone adhesion strength and/or greater bone contact area, thereby increasing the overall force to rupture the bone-implant interface. These results are supported by previous studies where effort was made to control for topography between PEEK and titanium surfaces [43, 177]. This favorable reaction is often attributed to titanium's high surface energy and hydrophilicity that are thought to drive preferential protein adsorption, mineral formation, and osteogenic differentiation of bone precursor cells [167, 178, 186]. The resulting bone adhesion strength to polished titanium surfaces that are devoid of interlocking features has been measured to be ~0.01 MPa [166]. Analogous measurements on PEEK have not been reported, but would provide critical insight into the different osseointegration mechanisms between these two materials.

Although bone-implant adhesion may contribute to implant fixation, mechanical interlocking of bone with topographical features, especially macro-scale features (e.g. pores), has been shown to generate mechanical responses that are orders of magnitude greater. When investigating mechanical interlock, the volume, density and orientation of ingrown bone must be considered.

In general, larger surface features facilitate greater volumes of bone ingrowth that result in an increased bearing area at the bone-implant interface to resist loads [165]. This relationship is supported by the current results where porous surfaces led to greater fixation than smooth and rough surfaces. These findings are corroborated by previous results that described similar relationships between smooth, rough and porous surfaces on monolithic titanium implants [36]. Interestingly in this study, mean mineralized tissue ingrowth and its correlation with all biomechanics outcomes was not significantly different between porous PEEK and porous titanium. These results provide convincing evidence that osseointegration and implant fixation is primarily governed by surface topography rather than surface material.

In addition to volume, the density of interlocking bone should also influence implant fixation because denser tissue ingrowth provides more mechanical resistance to separatory loads [147, 187]. Indeed, overall ingrowth density was correlated with pullout force and displayed correlation trends with other biomechanics outcomes. Overall ingrowth density was also highly correlated with mineralized tissue ingrowth, BV/PV_{3D}, for all porous surfaces ($r^2 > 0.97$, $p < 0.001$), which is to be expected as mineralized tissue ingrowth volume was defined using mineral density criteria. As before, no differences were detected between porous PEEK and porous titanium regarding tissue ingrowth density or its correlation to biomechanics outcomes, further illustrating the minimal contribution of surface material to the functional fixation of porous implants in this study.

The orientation of interlocking features to apposing bone also influences implant fixation. Simple peaks and valleys and similar surface asperities found on standard roughened surfaces provide mechanical interlock against shear and torsional loads.

However, rough surfaces often lack appreciable undercutting features that are required to protect the implant interface from tensile loads that can occur at the surfaces of total hip stems during normal physiological loading or spinal fusion cages during flexion and extension of the spine [99]. Therefore, the current study subjected implant interfaces to tensile loading as a worst-case loading scenario. As expected, smooth and rough surfaces lacked appreciable undercutting features compared to porous surfaces and resulted in decreased implant fixation. Further, rough surfaces did not improve implant fixation compared to smooth surfaces of the same material, indicating that rough topographies without appreciable undercutting and interlocking features might not sufficiently protect implants from tensile separation loads *in vivo*.

Overall, surface topography accounted for 66% of the total variance in pullout force compared to 7% for surface material. The magnitude of these effects is supported by Hacking et al., who used a similar coating methodology to demonstrate that 80% of the osseointegration response to hydroxyapatite (HA) coated surfaces was attributed to surface topography [171]. A more direct comparison to Hacking et al. using their calculation method (the simple ratio of the PEEK to titanium mean) on the current results demonstrates that 97% of the osseointegration response to porous implants was attributable to surface topography. This percentage decreases as surface topography gets smoother, from 55% on rough surface to 38% on smooth surfaces. This comparison clearly demonstrates the dominant influence of topography on osseointegration and provides evidence that the relative influence of material and topography is not constant across all topographies. These values also are reasonable considering that the HA topography of Hacking et al. likely fell somewhere between the rough and porous topographies of the current study.

The observation that porous PEEK and porous titanium implants achieved similar ingrowth volume, ingrowth density and overall implant fixation while exhibiting distinctly different tissue ingrowth morphologies is intriguing and warrants further study. Bone ingrowth into porous PEEK implants was more centralized within the pores with periodic contact with the pore walls. Conversely, bone ingrowth into porous titanium implants was largely absent from pore centers and exhibited more contact with the pore walls. These results suggest that different surface chemistries may drive different bone (re)modeling processes to achieve similar homeostatic biomechanical states. Similar shelling of bone along pore walls has been clearly noted within porous HA implants [188, 189] and certain porous titanium implants [137], yet a clear explanation for how each morphology is formed is still needed. A potential explanation of these events could relate to titanium's high surface energy leading to a more favorable protein adsorption profile that improved initial cell attachment to the implant surface where they could form bone directly.

An alternative explanation for different ingrowth morphologies relates to early events surrounding fibrin clot interactions with the implant surface. Despite possessing similar topography as porous PEEK, the negatively charged surface of porous titanium implants could have induced formation of a topographically complex mineral layer on the pore walls that served to interlock with the initial fibrin clot that formed shortly after implantation [38, 74, 167, 186]. This fibrin matrix then may have served as a continuous conduit through which cells could migrate to reach the implant surface and lay down bone directly onto the surface. Conversely, porous PEEK surfaces may not have formed a mineral layer upon implantation [38, 190], thereby limiting the fibrin clot's ability to anchor to the pore walls. Thus, cells may have only been able to migrate and form bone up

to the edge of the detached fibrin clot interface, which was separated from the pore wall, yet still interlocked within the macro-scale pores. This reasoning is supported by a recent study demonstrating that the addition of micro-porous interlocking features on the surface of macro-scale pores of porous PEEK implants increased bone apposition to the pore walls compared to porous PEEK without micro-porosity [191]. If these speculated events occurred, then a thin layer of closely apposed bone may have been sufficient to achieve adequate fixation of porous titanium implants; whereas porous PEEK implants may have required more bone ingrowth volume to achieve similar stability. A similar reasoning may also partially explain results on smooth and rough surfaces.

The current results are of particular relevance to the clinical setting due to the recent focus on surface technologies for orthopaedic implants, particularly in spine. First, these results support that adding a titanium surface to conventional smooth PEEK implants may improve their osseointegration and fixation. Indeed, a similar titanium thin film strategy is currently under clinical investigation to improve osseointegration of smooth PEEK implants [192]. However, the results also suggest that coating a porous PEEK implant with titanium will have a marginal effect over the pores themselves. With that said, current implants featuring porous PEEK are not porous throughout and could potentially benefit by having the non-porous surfaces display a titanium material. Applying nanoscale and submicron thick titanium coatings to PEEK implants is also advantageous because the coating does not produce medical imaging artifacts, unlike thicker titanium coatings that are plasma-sprayed.

This study had several limitations. First, XPS analysis suggested that porous PEEK may have possessed a slightly different surface material compared to other PEEK surfaces,

which could have resulted from additional oxygen species formation during porous processing. This effect may have increased the hydrophilicity of porous PEEK surfaces, as evidenced by blood wicking upon implantation, and be akin to similar results on oxygen-plasma and accelerated neutral atom beam treatment of PEEK [41, 139]. However, increased hydrophilicity has also been demonstrated to be influenced by rough surfaces and polymer recrystallization on high energy surfaces, both of which apply to the current porous PEEK surfaces [193, 194]. Further, capillary action likely had a large influence on the observed wicking behavior throughout the porous interface. Thus, several factors in addition to potential surface material modification could have influenced the wicking behavior of porous PEEK surfaces. Nevertheless, the potential for porous PEEK to possess a slightly different surface material may limit the ability to have absolute confidence that material was completely controlled for in this study. However, this technique was reasoned to be the most effective method currently available to independently modulate surface topography and material. In the future these issues may be better addressed through 3D printing techniques where the exact same materials processing method can be used to create well-defined topographies.

A second limitation is that partial volume effects may have prevented detection of finer ingrowth features, particularly for the thin shell morphology of porous titanium implants. Higher resolution scans may have lessened these effects, yet results were still expected to be representative of actual bone morphologies based on the correlations with biomechanical and histological analyses. Third, the smooth group in this study still possessed some surface features from machining which could have overinflated the

response to smooth PEEK and smooth titanium groups if bone interlocked with these features.

CHAPTER 7. CONCLUSIONS, CLINICAL TRANSLATION, AND FUTURE DIRECTIONS

7.1 Primary Conclusions

The overarching conclusion of this work is that PEEK surfaces with macro-porous surface topography exhibited enhanced osseointegration and implant fixation compared to smooth and rough surfaces, regardless of whether they possessed PEEK or titanium surface material. First, this challenges the general perception in the literature that the osseointegration of PEEK implants is inherently limited by its chemically inert and hydrophobic surface properties. Second, these results suggest that PEEK implant fixation was primarily dependent on the volume of bone that was mechanically interlocked with implant surface features. The larger undercutting features of macro-porous topographies facilitated greater volumes of mechanically interlocked bone and led to increased implant fixation compared to smooth and rough surfaces with smaller surface features that lacked appreciable undercuts.

7.1.1 Aim 1

In Aim 1, a unique method of extruding porosity from solid PEEK surfaces was introduced that preserved sufficient mechanical properties for load-bearing orthopaedic applications. *In vitro* studies using mouse pre-osteoblasts demonstrated that porous PEEK surfaces facilitated greater cell proliferation and osteogenic differentiation compared to smooth PEEK and that the cell response was relatively insensitive to pore size between 200 – 500 μm. Preliminary *in vivo* osseointegration studies demonstrated that porous PEEK led to

considerable bone ingrowth in cortical and trabecular environments, which led to increased strength of the bone-implant interface compared to conventional smooth PEEK surfaces. Overall, Aim 1 resulted in promising findings that warranted the continued investigation of porous PEEK and the potential factors that influence its osseointegration.

7.1.2 Aim 2

In Aim 2, porous PEEK was directly compared to plasma-sprayed titanium coatings on PEEK as another clinically relevant surface technology designed to overcome the poor osseointegration of conventional smooth PEEK implants. Porous PEEK surfaces led to enhanced *in vitro* osteogenic differentiation and greater *in vivo* osseointegration compared to both ti-coated PEEK and smooth PEEK surfaces, further demonstrating the potential for porous PEEK as an effective load-bearing orthopaedic biomaterial. This aim also demonstrated medical imaging artifact as being one of the practical disadvantages of ti-coated PEEK devices that prevented μCT analysis on the bone-implant interface. Comparing porous PEEK to ti-coated PEEK provided further insight into the relative influence of surface topography and surface chemistry on osseointegration. Porous PEEK possessed large macro-scale pores, slight micro-roughness, moderate nano-topography and displayed a PEEK surface chemistry. Ti-coated PEEK lacked macro-scale features, but possessed a significantly rougher micro- and nano-scale topography and displayed a titanium surface chemistry. With these surface characteristics in mind, the increased fixation of porous PEEK implants compared to ti-coated implants suggested that the macro-scale pores of porous PEEK surfaces had the greatest influence on osseointegration. This conclusion was further supported considering that these interfaces were biomechanically tested in tension, where the rough ti-coated surfaces did not have

appreciable undercutting features with which to interlock with apposed bone. Although this explanation seemed logical, multiple variables changed between porous PEEK and ti-coated PEEK surfaces, making it difficult to isolate any one variable as being the most influential.

7.1.3 Aim 3

In Aim 3, a more systematic approach was taken to evaluate the relative influence of surface chemistry and surface topography on PEEK implant osseointegration. Nano-scale titanium coatings were applied to smooth, rough, and porous PEEK surface topographies to change surface chemistry while holding surface topography relatively constant. Comparison of these titanium surface chemistries to uncoated PEEK surface chemistries of the same surface topography revealed that topography accounted for 66% of the total variance in implant fixation strength compared to 7% for surface chemistry. The results demonstrated a positive effect of titanium surface chemistry for smooth and rough topographies; however, there was no effect of surface chemistry for porous topographies. Further, porous topographies exhibited the strongest osseointegration response compared to smooth and rough surfaces regardless of surface chemistry, which further supported that macro-scale porosity has the greatest influence on PEEK implant osseointegration.

7.2 Contribution to the Field

This work could have broad impact in the orthopaedic biomaterials community. First, these data clearly demonstrate the dominant effect of macro-porosity on implant osseointegration compared to smooth and rough surface topographies. Second, this work suggests that osseointegration of macro-porous surfaces may be relatively independent of surface

chemistry. Indeed, these results corroborate previous reports in the literature that have demonstrated favorable bone ingrowth and fixation of macro-porous implants that possess vastly different surface chemistries, including metals, polymers, and ceramics [79, 99, 156-164]. Further, this work adds to the smaller subset of studies that have made explicit efforts to decouple the effects of surface topography and surface chemistry on implant osseointegration [140, 171]. Lastly, these results demonstrate that the relative influence of surface chemistry on implant osseointegration is not constant across multiple topographical length scales.

This porous PEEK material could also provide a unique opportunity for early post-surgical assessment of bone ingrowth in a clinical setting. In contrast to porous metal devices that can obscure x-ray, CT and MRI images, porous PEEK's radiolucency could enable surgeons to effectively and non-invasively measure local bone ingrowth into a porous network. This work clearly showed a direct positive correlation between bone ingrowth measured by CT and device fixation. Thus, early indications of implant osseointegration provided by local imaging assessment of osseous ingrowth into a radiolucent, porous implant could serve to better inform a surgeon's management of a patient's post-operative rehabilitation and physical therapy regime to improve overall clinical outcomes.

7.3 Clinical Translation[3]

The results contained in this dissertation have contributed to the successful clinical translation of porous PEEK onto a product line of interbody spinal fusion devices. The following has been adapted from Torstrick et al. where the development of these devices was reviewed [146]. First, the design and testing of the device is discussed, followed by an overview of the surgical technique and two clinical case examples.

7.3.1 Device Design

Given the mechanical and biological performance established in pre-clinical testing, a new interbody fusion device incorporating porous PEEK (COHERE®, Vertera Spine, Atlanta, GA) has been developed for use in anterior cervical discectomy and fusion (ACDF) procedures. The implant is manufactured out of a solid PEEK core with the porous PEEK architecture on the superior and inferior faces (Figure 7.1). This design allows for bony tissue ingrowth from adjacent vertebra while retaining the bulk physical and mechanical properties of PEEK for device structural integrity. The porous architecture also aids in creating more frictional resistance against bone, thereby reducing the risk for expulsion. Like other PEEK devices, the COHERE® device is radiolucent and does not produce imaging artifacts on X-ray and CT, a characteristic observed in the preclinical testing of porous PEEK (Figure 3.8). The device also features a large graft window, a 7 degree lordotic angle, and radiographic markers that run through the entire device on opposite ends.

[3] Modified from F.B. Torstrick, D.L. Safranski, J.K. Burkus, J.L. Chappuis, R.E. Guldberg, K.E. Smith, Getting PEEK to Stick to Bone: The Development of Porous PEEK for Interbody Fusion Devices, Tech Orthop 32(3) (2017) 158-166.

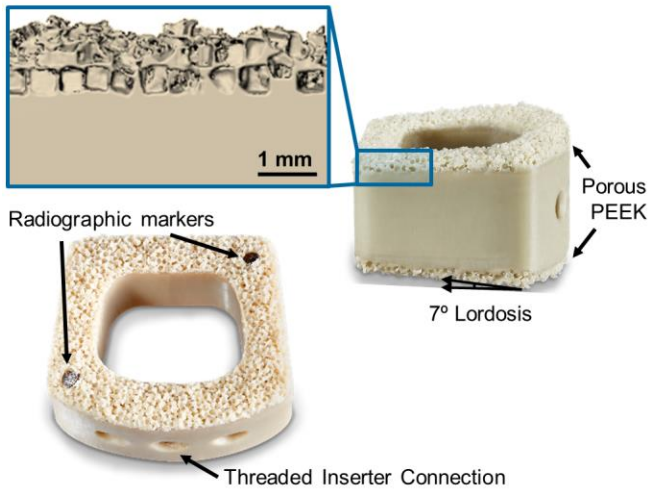

Figure 7.1 - Design and features of the COHERE® implant with porous PEEK on the superior and inferior faces. The inset shows a magnified µCT reconstruction of the porous PEEK three-dimensional structure. Scale bar is 1 mm.

7.3.2 Biomechanical Testing

The porous PEEK device has been subjected to extensive biomechanical testing to evaluate its durability and frictional properties under clinically relevant loading scenarios as part of its FDA 510(k) submission. Tensile adhesion strength testing was performed to determine the adhesive strength of the porous architecture to the solid PEEK base and compared with plasma-sprayed titanium coated PEEK devices (Calix PC, X-Spine Systems, Inc., Miamisburg, OH). Following ASTM F1147-05, porous PEEK devices and ti-coated PEEK devices were mounted with epoxy and pulled in tension at 0.25 cm/min with a mechanical test frame (Instron) until the components separated. Tensile adhesion strength was defined as the failure load normalized by the load-bearing cross-sectional area (n = 4 - 5). Porous PEEK devices had a higher tensile adhesion strength than ti-coated PEEK devices (13.7 ± 0.6 MPa vs. 7.7 ± 3.6 MPa, $p < 0.01$ – Student's t-test), which supports that porous PEEK

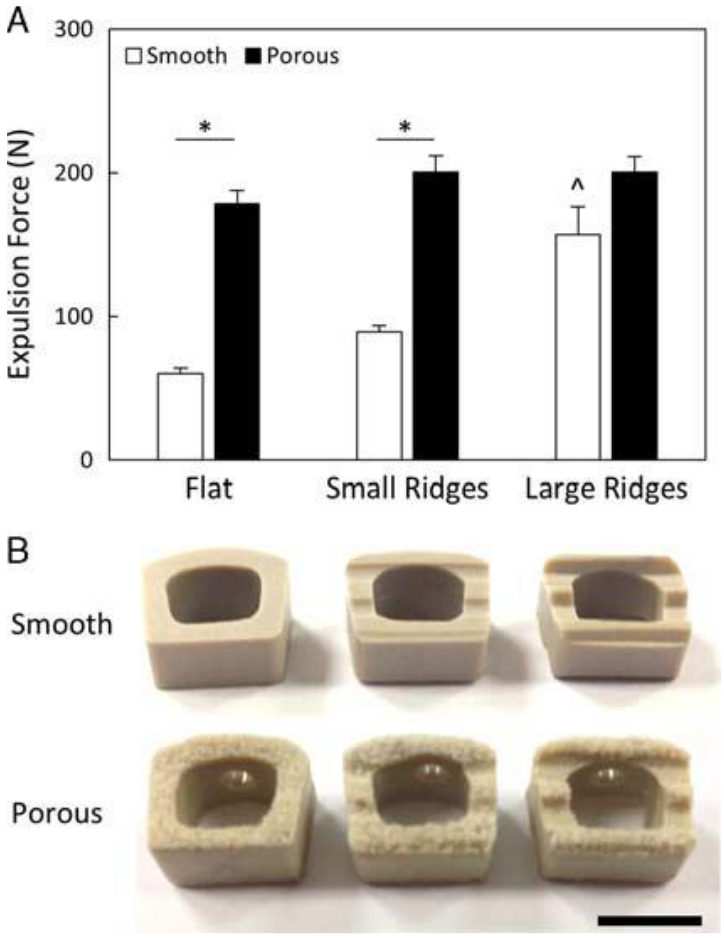

Figure 7.2 - A, Expulsion forces of smooth and porous PEEK devices with and without ridges. All data normalized to smooth cages without ridges. *p< 0.01, ^p<0.01 versus other smooth groups (2-way Analysis of Variance, Tukey) (mean±SE). B, Images depicting cage and ridge geometries. Scale bar is 1 cm.

is more durable than ti-coated PEEK. Notably these values are less than the tensile adhesion strength reported for standard flat 20 mm diameter adhesion cylinders (Porous PEEK: 24.7 ± 0.6 MPa, ti-coated PEEK: 19.3 ± 2.1 MPa). This difference is attributed to the increased edge-to-surface ratio of these fusion devices (0.7 – 1.0 mm^{-1}) compared to the cylindrical test samples (0.2 mm^{-1}).

Next, porous PEEK devices were subjected to implant push-out testing in a benchtop intervertebral model to investigate their resistance to expulsion. Each device was

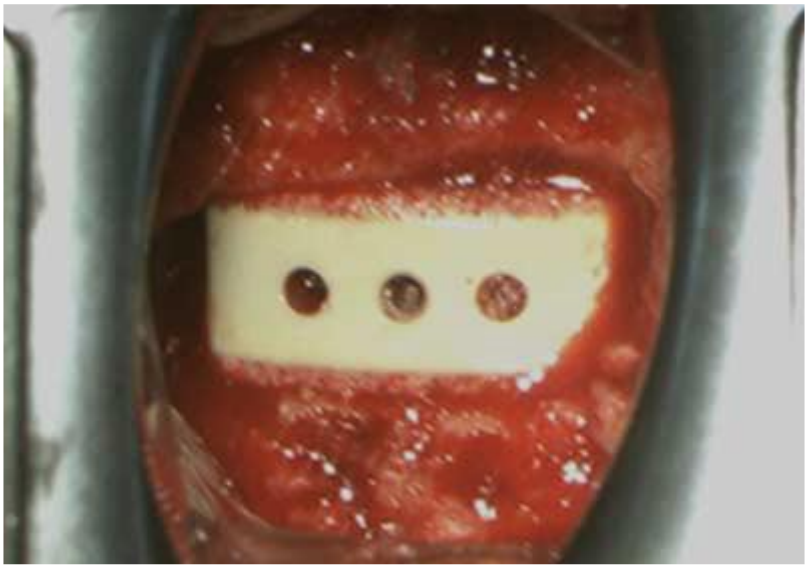

Figure 7.3 - Intraoperative photo showing a porous PEEK device implanted in an anterior cervical discectomy and fusion surgery. Soon after insertion into the disk space, blood could be seen wicking into the porous architecture.

inserted in between two polyurethane foam blocks (Sawbone, 15 PCF) and a 157 N normal force was applied to the blocks to simulate axial compression of the cervical spine. A transverse load was then applied to the posterior implant face at a rate of 0.1mm/s until the implant expulsed. Throughout the design of the COHERE® device it was determined that, in contrast to smooth devices, adding ridges to the porous faces of the implant did not improve expulsion resistance (Figure 7.2). Thus, COHERE® devices feature flat porous faces to provide maximum contact area between bone and porous architecture upon implantation. To ensure adequate expulsion resistance, the final COHERE® device was compared to a clinically available smooth PEEK cage that uses ridges (Crystal Cervical Interbody System, Spinal Elements, Carlsbad, CA) and the COHERE® device was found to have 71% greater expulsion force (466 ± 31 N vs. 271 ± 49 N) ($p < 0.01$, Student's t-test, $n = 5$).

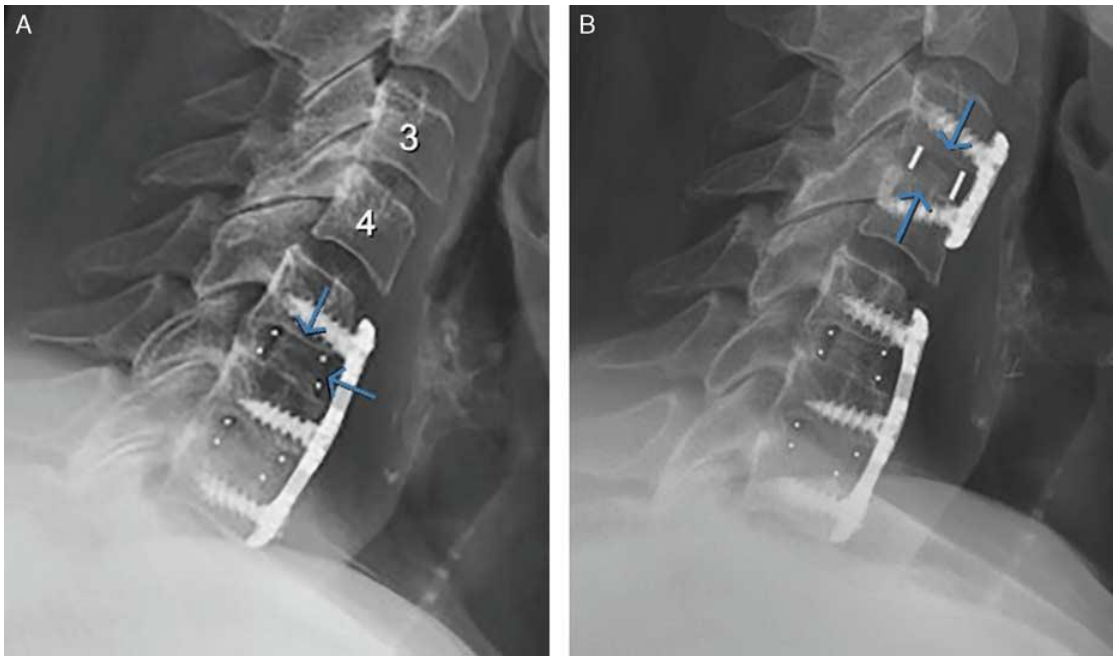

Figure 7.4 - Preoperative (A) and 3-month postoperative (B) lateral radiographs of a patient who underwent anterior cervical discectomy and fusion surgery and received a porous polyether-ether-ketone implant at level C3-C4. The postoperative image showed that disk height and lordosis had been restored and maintained with evidence of bony bridging. Arrows denote interface between vertebral body and implant.

7.3.3 Surgical Technique

The COHERE® device can be implanted into the intervertebral disc space using a standard ACDF surgical technique similar to that used for implanting other cervical cages. The affected disc and adjacent vertebral bodies are exposed via an anterior approach. Once a discectomy is performed per standard procedure and the segment distracted, the endplates can be prepared using rasps, curettes, and/or other instruments of choice. Implant trials matching the footprint and height of each implant size offering are used to determine the appropriate COHERE® implant size. The trial size (footprint x height) accurately matches the same implant footprint and height. Once the appropriate implant size is selected, the

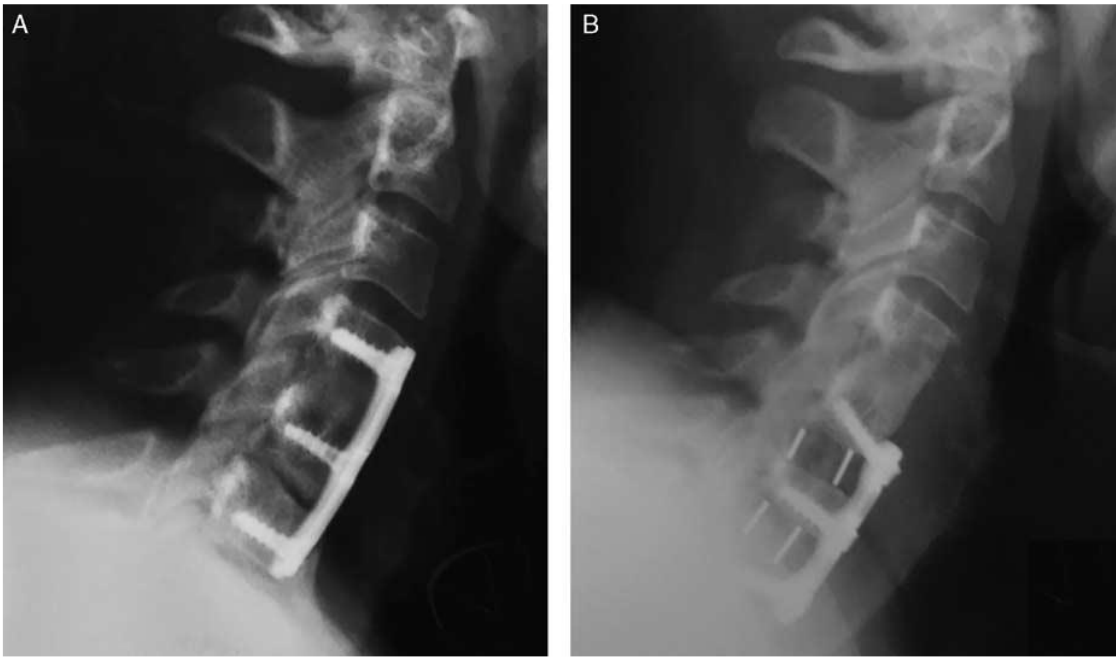

Figure 7.5 - Preoperative (A) and 5-month postoperative (B) lateral radiographs of patient who underwent anterior cervical discectomy and fusion surgery and received 2 porous polyether-ether-ketone implants at C5-C6 and C6-C7 levels. Postoperative image shows bony bridging across disk space.

interior window of the COHERE® cage is then packed with bone graft and placed anteriorly into the disc space using a universal inserter. Of note, one of the authors has described using the high friction porous faces in a rasp-like manner to collect additional autograft from the endplates within the pores to provide an improved healing bed for fusion. Implant location can be verified on fluoroscopy as needed. If further adjustment is needed, a tamp can be used to accurately position the cage into place. Lastly, additional bone graft material can then be packed around the cage, if desired. Usually immediately following implantation, bleeding bone can be seen wicking into the porous architecture on the cage (Figure 7.3).

7.3.4 Clinical Case Example 1

A 64-year-old female, who had undergone two previous cervical fusions in 1982 and 1997, developed adjacent segment degeneration at the C3-C4 cervical level. The patient reported neck pain and arm radiculopathy and had objective neurological signs of weakness, loss of sensation and depressed reflexes. A lateral radiograph showed disc space collapse, radial osteophyte formation, and sagittal plane malalignment (retrolisthesis and kyphosis) at the C3-C4 level (Figure 7.5).

The patient underwent an ACDF and received a porous PEEK COHERE® implant in conjunction with an anterior plate and autogenous iliac crest taken through a minimally invasive approach using only cancellous bone and bone marrow aspirate. At 3 months after surgery, a lateral radiograph showed restoration and maintenance of anatomic disc space height, segmental lordosis, and normal sagittal alignment (Figure 7.5). The patient had excellent relief of neck pain and radiating pain with complete return of neurological status. After surgery and follow-up she was neurologically intact. Importantly, there were no lucencies around the PEEK implant. An uninterrupted, continuous column of bone was seen through the central portion of the COHERE implant with complete integration of the bone graft to the bony endplates of the adjacent vertebra.

7.3.5 Clinical Case Example 2

A 55-year old female patient with a history of diabetes type 2 and BMI greater than 50 presented for evaluation and management after having had a previous multi-level ACDF (C4-C6) with an outside surgeon approximately 7 years prior. The patient presented with persistent neck pain of 7/10 on the pain scale, with 100% neck pain. The patient was

ordered to undergo an EMG and CT Myelogram. The EMG of the upper extremities was unremarkable. The cervical spine CT Myelogram revealed a disc osteophyte complex at C6-C7 cervical level with pseudarthrosis at C5-C6 level (Figure 7.4).

After a year of unsuccessful conservative treatment, the patient underwent surgery for revision ACDF using the porous PEEK COHERE® implant for painful pseudoarthrosis at C5-C6 with microscopic anterior discectomy and decompression of spinal canal stenosis as well as bilateral neuroforaminotomies at C6-C7, with extension of fusion at C6-C7 (Figure 7.4). Demineralized bone matrix (DBM) was used as allograft to fill the interior window of the cage along with plates and screws to provide segmental stabilization.

At 5 months following surgery, the patient was seen for follow-up. Anterior-posterior (A-P) and lateral radiographs were completed showing the COHERE® implant, plate, and screws intact and in good position with solid-appearing interosseous growth at C5-C6 and C6-C7. It was noted that disc height had improved and lordosis had been restored and maintained. The patient reported functional range of motion in all planes of the cervical spine and presented a post-operative pain score of 0/10. The patient had discontinued all opiate use four months post-operatively.

7.4 Future Directions

Throughout this work, several questions and potential projects have been identified that merit future study.

First, further tuning of the porous PEEK pore morphology could lead to improved osseointegration outcomes. Porous networks can assume a multitude of architectures that

vary in pore size, pore shape, porosity, interconnectivity, permeability and strut thickness, among others. In this work, a pore size of ~350 μm was selected based on extensive previous work by others demonstrating this pore size to be favorable towards osseointegration [55]. Further, the overall cell response to porous PEEK networks did not change for pores 200 – 500 μm in size. However, rigorously testing the effect of pore size *in vivo* and extending this size range to include micro-scale pores (20 – 50 μm) and larger macro-pores (800 – 1,000 μm) could confirm these outcomes or result in the discovery that another pore size is more favorable for osseointegration. Additionally, there is evidence that multi-modal pore size could further improve porous PEEK osseointegration [191, 195]. Network porosity also has an influence on implant osseointegration, but was not investigated in this work. Greater porosities typically lead to more bone ingrowth and greater implant fixation; however, the mechanical properties of porous structure can decrease drastically with increased porosity, effectively setting a practical upper threshold on porosity for load-bearing applications. The positive effects of increased porosity may be due to the associated increase in permeability. Permeability of the porous network can influence osseointegration by modulating the degree of nutrient transfer to tissue within the pores. Promising work on non-PEEK materials has demonstrated that porous structures with high permeability (and associated increase in porosity) are favorable for bone regeneration [196]. Lastly, investigating how osseointegration varies as a function of pore depth could be valuable from an implant design perspective. Thinner pore depths are beneficial from a mechanical properties perspective; however, thicker depths offer more bone ingrowth volume and potential for mechanical interlocking. Finding the optimal

balance between of these two factors, in addition to spatial location of porosity on the implant surface, could be a critical factor in porous implant design.

3D printing of porous PEEK scaffolds represents an exciting method to investigate the effect of pore structure discussed above. Indeed, 3D printing of porous PEEK has advanced a great deal in recent years, with feature size resolution ever improving. 3D printing coupled with computational topology design techniques represents a unique method to modulate particular pore parameters while holding others constant to systematically investigate optimal pore network design [197]. 3D printing of porous PEEK (and other materials) also represents a unique method of controlling surface chemistry while holding surface topography constant. All surfaces of 3D printed pore networks would share a similar processing history and therefore would be expected to have the same surface chemistry.

Despite best efforts to independently modify surface chemistry and surface topography in Aim 3, surface characterization suggested that minor variations in nano-topography may have occurred following ALD coating. This could possibly be circumvented by using less ALD cycles to achieve thinner layers. Alternatively, more precise methods to change surface chemistry while minimizing topographical changes could be investigated. Self-assembled monolayers (SAMs) represent one well characterized technique that could be used to change the surface properties of the implant [198, 199]. ALD could also be used to investigate the effect of other chemistries than PEEK or titanium on implant osseointegration. Of most relevance to orthopaedics is perhaps silicon nitride, from which many devices are made. Coating different PEEK topographies

with TiO_2, SiN, and various other chemistries could provide a better understanding of the effect of surface chemistry in relation to surface topography.

Another area that merits future study relates to the use of porous PEEK as a drug delivery vehicle to further stimulate osseointegration. This goal could be accomplished using methods such as bioactive coatings on the pore surface or drug-loaded hydrogels within the pore volume. Bioactive HA mineral coatings on biomedical polymers have demonstrated effective delivery of drugs or growth factors (such as BMP-2 and VEGF) over extended periods of time [190, 200-202]. This process is advantageous over other mineral coatings (i.e. plasma-sprayed hydroxyapatite) in that it is independent of implant geometry and produces a carbonated hydroxyapatite coating that is similar to native bone. Drug-loaded hydrogels, such as alginate or fibrin, have also been used to accelerate osseointegration of porous scaffolds [84, 85, 203].

One particularly interesting set of future studies could be to investigate the role of fibrin clot interactions with implant surfaces of varying surface topography and chemistry. Blood is the first substance to interact with implanted materials. It is the source of the first adsorbed proteins and forms the fibrin matrix through which cells migrate during healing. One theory suggests that fibrin clot retention to the implant surface is critical for bone cells to be able to reach the surface to lay down bone (i.e. osteoconduction). However, previous work has shown that smooth surfaces have reduced fibrin clot retention compared to roughened surfaces (Figure 7.6) [168, 204]. This is thought to be caused by fibrin interlocking with undercutting surface features during the clotting process, which firmly attaches the matrix to the implant surface and provides a continuous conduit for migrating cells to reach the surface. These observations further support investigation of multi-modal

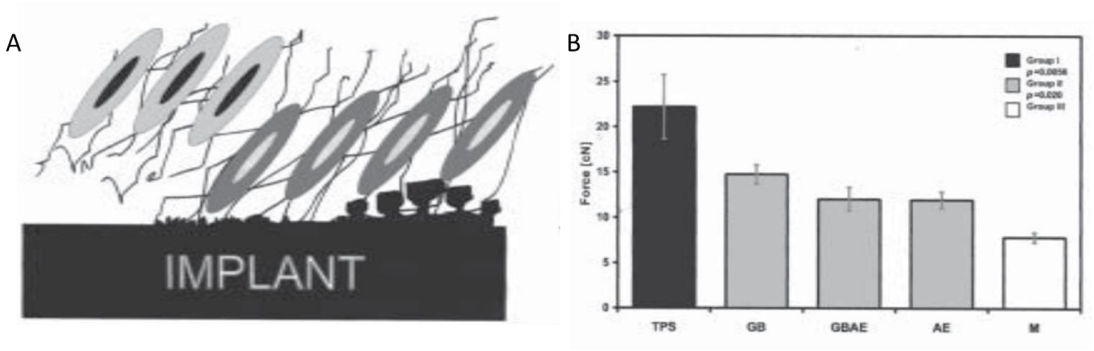

Figure 7.6 – Illustration of the potential effect of surface topography on fibrin retention to implant surfaces. Panel (A) illustrates fibrin detachment from smooth surface regions and interlocking with topographically complex surface regions to keep the fibrin matrix attached to the surface. Panel (B) shows mean peak retention forces of fibrin clots to titanium surfaces of varying topography, but similar surface chemistry. Greater fibrin retention forces were achieved on the roughest titanium plasma-sprayed surfaces due to wrapping of fibrin bundles around the large undercut features. TPS: plasma-sprayed; GB: grit-blasted; GBAE: grit-blasted and dual acid-etched; AE: Dual acid-etched; M: Machined. (Adapted from Davies, 1998).

pore distributions. Indeed, Hieda, et al. reported increased bone apposition to macro-porous PEEK surfaces in the presence of an overlaid micro-porosity [191]. Further, Aim 3 results suggest that surface chemistry may also play a role in fibrin clot retention by demonstrating different bone ingrowth morphologies within porous PEEK and porous titanium surfaces. A potential mechanism for this occurrence is presented in the Aim 3 discussion, yet further study is needed.

Lastly, future work should focus on delineating the role of surface topography and surface chemistry on osseointegration within the context of implant-mediated inflammation and immune response [205, 206]. Most orthopaedic devices are implanted within a tissue environment that is actively responding to iatrogenic injury from surgery. Successful osseointegration of an implant is influenced by its interactions with this early inflammatory stage and its capacity to modulate the long term immune environment

towards an osteogenic rather than fibrotic state. Upon implantation, a material surface is bombarded by a host of biological factors, including blood proteins (namely albumin, immunoglobulins, fibrinogen, vitronectin, and fibronectin), complement components, and their subsequent recognition by neutrophils, macrophages, and other immune cells [205, 206]. Surface topography and chemistry of implanted materials can modulate how these proteins adsorb to the surface and alter their recognition by neighboring immune cells [207]. These initial interactions with the material surface could set in motion a sequence of events contributing to the ultimate success or failure of the implant. It is hypothesized that the probability of reaching a successful osteogenic state could be related to the phenotypic switch pattern of local macrophages from a predominately pro-inflammatory M1 phenotype to a predominately anti-inflammatory M2 phenotype [208]. Further, immune cells are now recognized as being tightly linked with osteoblast and osteoclast function in regulating physiological bone formation and resorption [208, 209]. Thus, a thorough understanding of the inflammatory and immune response to the surface topography and chemistry of orthopaedic biomaterials is essential.

Several studies on PEEK and porous materials further motivate the importance and relevance of understanding the inflammatory and immune response to porous PEEK. Previous *in vitro* work has reported an increased production of inflammatory cytokines by hMSCs in response to smooth PEEK surfaces compared to titanium surfaces [210]. However, it is unclear what the relative influence of surface topography and surface chemistry was on these outcomes. Indeed, 3D porous topographies have been associated with a reduced pro-inflammatory microenvironment compared to 2D surfaces during *in vitro* co-cultures of MSCs and macrophages [211]. Further, higher porosities and larger

pore sizes have been associated with a decreased inflammatory response *in vivo* and a more tissue regenerative M2 phenotype during *in vitro* culture of bone marrow derived macrophages [212-214]. These results motivate further investigation into the inflammatory and immune response to porous PEEK.

REFERENCES

[1] HCUPnet, Healthcare Cost and Utilization Project (HCUP), Agency for Healthcare Research and Quality, Rockville, MD, 1997-2012.

[2] S.S. Rajaee, H.W. Bae, L.E. Kanim, R.B. Delamarter, Spinal fusion in the United States: analysis of trends from 1998 to 2008, Spine (Phila Pa 1976) 37(1) (2012) 67-76.

[3] R.A. Deyo , A. Nachemson , S.K. Mirza Spinal-Fusion Surgery — The Case for Restraint, N. Engl. J. Med. 350(7) (2004) 722-726.

[4] J.C. Wang, P.V. Mummaneni, R.W. Haid, Current treatment strategies for the painful lumbar motion segment: posterolateral fusion versus interbody fusion, Spine (Phila Pa 1976) 30(16 Suppl) (2005) S33-43.

[5] G.W. Smith, R.A. Robinson, The Treatment of Certain Cervical-Spine Disorders by Anterior Removal of the Intervertebral Disc and Interbody Fusion, The Journal of Bone & Joint Surgery 40(3) (1958) 607-624.

[6] I. Millenium Research Group, US Market for Spinal Implants 2010, Toronto, Ontario, 2010.

[7] G. Matgé, A.T. Leclercq, Rationale for Interbody Fusion With Threaded Titanium Cages at Cervical and Lumbar Levels. Results on 357 Cases, Acta Neurochir. (Wien.) 142(4) (2000) 425-434.

[8] P. Fritzell, O. Hägg, P. Wessberg, A. Nordwall, S.L.S.S. Group, 2001 Volvo Award Winner in Clinical Studies: Lumbar Fusion Versus Nonsurgical Treatment for Chronic Low Back Pain: A Multicenter Randomized Controlled Trial From the Swedish Lumbar Spine Study Group, Spine (Phila Pa 1976) 26(23) (2001) 2521-2532.

[9] P. Fritzell, O. Hagg, A. Nordwall, G. Swedish Lumbar Spine Study, Complications in lumbar fusion surgery for chronic low back pain: comparison of three surgical techniques used in a prospective randomized study. A report from the Swedish Lumbar Spine Study Group, Eur. Spine J. 12(2) (2003) 178-89.

[10] S.D. Glassman, L.Y. Carreon, M. Djurasovic, J.R. Dimar, J.R. Johnson, R.M. Puno, M.J. Campbell, Lumbar fusion outcomes stratified by specific diagnostic indication, The Spine Journal 9(1) (2009) 13-21.

[11] B.I. Martin, S.K. Mirza, B.A. Comstock, D.T. Gray, W. Kreuter, R.A. Deyo, Reoperation rates following lumbar spine surgery and the influence of spinal fusion procedures, Spine (Phila Pa 1976) 32(3) (2007) 382-7.

[12] Y.R. Rampersaud, S.J. Lewis, J.R. Davey, R. Gandhi, N.N. Mahomed, Comparative outcomes and cost-utility after surgical treatment of focal lumbar spinal stenosis compared with osteoarthritis of the hip or knee—part 1: long-term change in health-related quality of life, The Spine Journal 14(2) (2014) 234-243.

[13] B.I. Martin, S.K. Mirza, B.A. Comstock, D.T. Gray, W. Kreuter, R.A. Deyo, Are lumbar spine reoperation rates falling with greater use of fusion surgery and new surgical technology?, Spine (Phila Pa 1976) 32(19) (2007) 2119-26.

[14] R.A. Deyo, M.A. Ciol, D.C. Cherkin, J.D. Loeser, S.J. Bigos, Lumbar spinal fusion. A cohort study of complications, reoperations, and resource use in the Medicare population, Spine (Phila Pa 1976) 18(11) (1993) 1463-70.

[15] J.M. Mok, J.M. Cloyd, D.S. Bradford, S.S. Hu, V. Deviren, J.A. Smith, B. Tay, S.H. Berven, Reoperation after primary fusion for adult spinal deformity: rate, reason, and timing, Spine (Phila Pa 1976) 34(8) (2009) 832-9.

[16] P. Park, H.J. Garton, V.C. Gala, J.T. Hoff, J.E. McGillicuddy, Adjacent segment disease after lumbar or lumbosacral fusion: review of the literature, Spine (Phila Pa 1976) 29(17) (2004) 1938-44.

[17] P. Aspenberg, S. Goodman, S. Toksvig-Larsen, L. Ryd, T. Albrektsson, Intermittent micromotion inhibits bone ingrowth. Titanium implants in rabbits, Acta Orthop. Scand. 63(2) (1992) 141-5.

[18] J.W. Duncan, R.A. Bailey, An analysis of fusion cage migration in unilateral and bilateral fixation with transforaminal lumbar interbody fusion, Eur. Spine J. 22(2) (2012) 439-445.

[19] L. Chen, H. Yang, T. Tang, Cage migration in spondylolisthesis treated with posterior lumbar interbody fusion using BAK cages, Spine (Phila Pa 1976) 30(19) (2005) 2171-5.

[20] E.A. Uzi, D. Dabby, E. Tolessa, J.A. Finkelstein, Early Retropulsion of Titanium-Threaded Cages After Posterior Lumbar Interbody Fusion: A Report of Two Cases, Spine (Phila Pa 1976) 26(9) (2001) 1073-1075.

[21] Q.-x. Deng, Y.-s. Ou, Y. Zhu, Z.-h. Zhao, B. Liu, Q. Huang, X. Du, D.-m. Jiang, Clinical outcomes of two types of cages used in transforaminal lumbar interbody fusion for the treatment of degenerative lumbar diseases: n-HA/PA66 cages versus PEEK cages, J. Mater. Sci. Mater. Med. 27(6) (2016) 1-9.

[22] R. Dunn, C. Pretorius, Cervical PEEK cage standalone fusion: the issue of subsidence, SA Orthopaedic Journal 10 (2011) 25-29.

[23] E. Gercek, V. Arlet, J. Delisle, D. Marchesi, Subsidence of stand-alone cervical cages in anterior interbody fusion: warning, Eur. Spine J. 12(5) (2003) 513-516.

[24] T.V. Le, A.A. Baaj, E. Dakwar, C.J. Burkett, G. Murray, D.A. Smith, J.S. Uribe, Subsidence of Polyetheretherketone Intervertebral Cages in Minimally Invasive Lateral Retroperitoneal Transpsoas Lumbar Interbody Fusion, Spine (Phila Pa 1976) 37(14) (2012) 1268-1273.

[25] L. Carlsson, T. Rostlund, B. Albrektsson, T. Albrektsson, P.I. Branemark, Osseointegration of titanium implants, Acta Orthop Scand 57(4) (1986) 285-9.

[26] J. Nagels, M. Stokdijk, P.M. Rozing, Stress shielding and bone resorption in shoulder arthroplasty, J. Shoulder Elbow Surg. 12(1) (2003) 35-9.

[27] S.M. Kurtz, J.N. Devine, PEEK biomaterials in trauma, orthopedic, and spinal implants, Biomaterials 28(32) (2007) 4845-69.

[28] D.M. Devine, J. Hahn, R.G. Richards, H. Gruner, R. Wieling, S.G. Pearce, Coating of carbon fiber-reinforced polyetheretherketone implants with titanium to improve bone apposition, J Biomed Mater Res B Appl Biomater 101(4) (2013) 591-8.

[29] K.A. Jockisch, S.A. Brown, T.W. Bauer, K. Merritt, Biological response to chopped-carbon-fiber-reinforced peek, J. Biomed. Mater. Res. 26(2) (1992) 133-146.

[30] T. Nieminen, I. Kallela, E. Wuolijoki, H. Kainulainen, I. Hiidenheimo, I. Rantala, Amorphous and crystalline polyetheretherketone: Mechanical properties and tissue reactions during a 3-year follow-up, Journal of Biomedical Materials Research Part A 84A(2) (2008) 377-383.

[31] N.A. Athanasou, J. Quinn, C.J. Bulstrode, Resorption of bone by inflammatory cells derived from the joint capsule of hip arthroplasties, The Journal of bone and joint surgery. British volume 74(1) (1992) 57-62.

[32] C. Maniatopoulos, R.M. Pilliar, D.C. Smith, Threaded versus porous-surfaced designs for implant stabilization in bone-endodontic implant model, J. Biomed. Mater. Res. 20(9) (1986) 1309-33.

[33] P. Robotti, G. Zappini, Thermal Plasma Spray Deposition of Titanium and Hydroxyapatite on Polyaryletheretherketone Implants, 2012.

[34] R.A. Gittens, R. Olivares-Navarrete, Z. Schwartz, B.D. Boyan, Implant osseointegration and the role of microroughness and nanostructures: Lessons for spine implants, Acta Biomaterialia 10(8) (2014) 3363-3371.

[35] R.M. Wazen, J.A. Currey, H. Guo, J.B. Brunski, J.A. Helms, A. Nanci, Micromotion-induced strain fields influence early stages of repair at bone–implant interfaces, Acta biomaterialia 9(5) (2013) 6663-6674.

[36] M. Svehla, P. Morberg, B. Zicat, W. Bruce, D. Sonnabend, W.R. Walsh, Morphometric and mechanical evaluation of titanium implant integration: comparison of five surface structures, J Biomed Mater Res 51(1) (2000) 15-22.

[37] W.R. Walsh, N. Bertollo, C. Christou, D. Schaffner, R.J. Mobbs, Plasma-sprayed titanium coating to polyetheretherketone improves the bone-implant interface, Spine J 15(5) (2015) 1041-9.

[38] Y. Zhao, H.M. Wong, W.H. Wang, P.H. Li, Z.S. Xu, E.Y.W. Chong, C.H. Yan, K.W.K. Yeung, P.K. Chu, Cytocompatibility, osseointegration, and bioactivity of three-dimensional porous and nanostructured network on polyetheretherketone, Biomaterials 34(37) (2013) 9264-9277.

[39] M.S. Abu Bakar, M.H.W. Cheng, S.M. Tang, S.C. Yu, K. Liao, C.T. Tan, K.A. Khor, P. Cheang, Tensile properties, tension–tension fatigue and biological response of polyetheretherketone–hydroxyapatite composites for load-bearing orthopedic implants, Biomaterials 24(13) (2003) 2245-2250.

[40] D. Briem, S. Strametz, K. Schröoder, N.M. Meenen, W. Lehmann, W. Linhart, A. Ohl, J.M. Rueger, Response of primary fibroblasts and osteoblasts to plasma treated polyetheretherketone (PEEK) surfaces, J. Mater. Sci. Mater. Med. 16(7) (2005) 671-677.

[41] S.-W. Ha, R. Hauert, K.-H. Ernst, E. Wintermantel, Surface analysis of chemically-etched and plasma-treated polyetheretherketone (PEEK) for biomedical applications, Surface and coatings technology 96(2-3) (1997) 293-299.

[42] S.-W. Ha, M. Kirch, F. Birchler, K.-L. Eckert, J. Mayer, E. Wintermantel, C. Sittig, I. Pfund-Klingenfuss, M. Textor, N. Spencer, Surface activation of polyetheretherketone (PEEK) and formation of calcium phosphate coatings by precipitation, Journal of Materials Science: Materials in Medicine 8(11) (1997) 683-690.

[43] C.-M. Han, E.-J. Lee, H.-E. Kim, Y.-H. Koh, K.N. Kim, Y. Ha, S.-U. Kuh, The electron beam deposition of titanium on polyetheretherketone (PEEK) and the resulting enhanced biological properties, Biomaterials 31(13) (2010) 3465-3470.

[44] A.H. Poulsson, D. Eglin, S. Zeiter, K. Camenisch, C. Sprecher, Y. Agarwal, D. Nehrbass, J. Wilson, R.G. Richards, Osseointegration of machined, injection moulded and oxygen plasma modified PEEK implants in a sheep model, Biomaterials 35(12) (2014) 3717-28.

[45] D. Rymuszka, K. Terpiłowski, P. Borowski, L. Holysz, Time Dependent Changes of Surface Properties of Polyether Ether Ketone Caused by Air Plasma Treatment, Polymer International (2016) n/a-n/a.

[46] G. Zhao, Z. Schwartz, M. Wieland, F. Rupp, J. Geis-Gerstorfer, D.L. Cochran, B.D. Boyan, High surface energy enhances cell response to titanium substrate microstructure, Journal of Biomedical Materials Research Part A 74A(1) (2005) 49-58.

[47] D. Khang, S.Y. Kim, P. Liu-Snyder, G.T.R. Palmore, S.M. Durbin, T.J. Webster, Enhanced fibronectin adsorption on carbon nanotube/poly(carbonate) urethane: Independent role of surface nano-roughness and associated surface energy, Biomaterials 28(32) (2007) 4756-4768.

[48] J.Y. Martin, Z. Schwartz, T.W. Hummert, D.M. Schraub, J. Simpson, J. Lankford, Jr., D.D. Dean, D.L. Cochran, B.D. Boyan, Effect of titanium surface roughness on proliferation, differentiation, and protein synthesis of human osteoblast-like cells (MG63), J. Biomed. Mater. Res. 29(3) (1995) 389-401.

[49] A. Wennerberg, T. Albrektsson, Effects of titanium surface topography on bone integration: a systematic review, Clin. Oral Implants Res. 20 (2009) 172-184.

[50] K. Cai, J. Bossert, K.D. Jandt, Does the nanometre scale topography of titanium influence protein adsorption and cell proliferation?, Colloids and Surfaces B: Biointerfaces 49(2) (2006) 136-144.

[51] R.L. Price, K. Ellison, K.M. Haberstroh, T.J. Webster, Nanometer surface roughness increases select osteoblast adhesion on carbon nanofiber compacts, Journal of Biomedical Materials Research Part A 70A(1) (2004) 129-138.

[52] L. Yang, B.W. Sheldon, T.J. Webster, The impact of diamond nanocrystallinity on osteoblast functions, Biomaterials 30(20) (2009) 3458-3465.

[53] E.M. Lotz, R. Olivares-Navarrete, S. Berner, B.D. Boyan, Z. Schwartz, Osteogenic Response of Human MSCs and Osteoblasts to Hydrophilic and Hydrophobic Nanostructured Titanium Implant Surfaces, Journal of Biomedical Materials Research Part A (2016) n/a-n/a.

[54] G.L. Converse, T.L. Conrad, R.K. Roeder, Mechanical properties of hydroxyapatite whisker reinforced polyetherketoneketone composite scaffolds, J Mech Behav Biomed Mater 2(6) (2009) 627-35.

[55] V. Karageorgiou, D. Kaplan, Porosity of 3D biomaterial scaffolds and osteogenesis, Biomaterials 26(27) (2005) 5474-91.

[56] E.A. Lewallen, S.M. Riester, C.A. Bonin, H.M. Kremers, A. Dudakovic, S. Kakar, R.C. Cohen, J.J. Westendorf, D.G. Lewallen, A.J. van Wijnen, Biological Strategies for Improved Osseointegration and Osteoinduction of Porous Metal Orthopedic Implants, Tissue Engineering Part B: Reviews 21(2) (2014) 218-230.

[57] R.A. Gittens, R. Olivares-Navarrete, T. McLachlan, Y. Cai, S.L. Hyzy, J.M. Schneider, Z. Schwartz, K.H. Sandhage, B.D. Boyan, Differential responses of osteoblast lineage cells to nanotopographically-modified, microroughened titanium-aluminum-vanadium alloy surfaces, Biomaterials 33(35) (2012) 8986-8994.

[58] G. Zhao, A.L. Raines, M. Wieland, Z. Schwartz, B.D. Boyan, Requirement for both micron- and submicron scale structure for synergistic responses of osteoblasts to substrate surface energy and topography, Biomaterials 28(18) (2007) 2821-2829.

[59] X. Wang, Z. Schwartz, R.A. Gittens, A. Cheng, R. Olivares-Navarrete, H. Chen, B.D. Boyan, Role of integrin alpha(2)beta(1) in mediating osteoblastic differentiation on three-

dimensional titanium scaffolds with submicron-scale texture, Journal of Biomedical Materials Research Part A 103(6) (2015) 1907-1918.

[60] S.L. Edwards, J.A. Werkmeister, Mechanical evaluation and cell response of woven polyetheretherketone scaffolds, Journal of Biomedical Materials Research Part A 100A(12) (2012) 3326-3331.

[61] N.T. Evans, C.W. Irvin, D.L. Safranski, K. Gall, Impact of surface porosity and topography on the mechanical behavior of high strength biomedical polymers, J Mech Behav Biomed 59 (2016) 459-473.

[62] N.T. Evans, F.B. Torstrick, C.S.D. Lee, K.M. Dupont, D.L. Safranski, W.A. Chang, A.E. Macedo, A.S.P. Lin, J.M. Boothby, D.C. Whittingslow, R.A. Carson, R.E. Guldberg, K. Gall, High-strength, surface-porous polyether-ether-ketone for load-bearing orthopedic implants, Acta Biomaterialia 13 (2015) 159-167.

[63] N.T. Evans, F.B. Torstrick, D.L. Safranski, R.E. Guldberg, K. Gall, Local deformation behavior of surface porous polyether-ether-ketone, J Mech Behav Biomed 65 (2017) 522-532.

[64] B.C. Landy, S.B. VanGordon, P.S. McFetridge, V.I. Sikavitsas, M. Jarman-Smith, Mechanical and in vitro investigation of a porous PEEK foam for medical device implants, Journal of Applied Biomaterials & Functional Materials 11(1) (2013) 35-44.

[65] M. Roskies, J.O. Jordan, D.D. Fang, M.N. Abdallah, M.P. Hier, A. Mlynarek, F. Tamimi, S.D. Tran, Improving PEEK bioactivity for craniofacial reconstruction using a 3D printed scaffold embedded with mesenchymal stem cells, J. Biomater. Appl. 31(1) (2016) 132-139.

[66] A.R. Siddiq, A.R. Kennedy, Porous poly-ether ether ketone (PEEK) manufactured by a novel powder route using near-spherical salt bead porogens: Characterisation and mechanical properties, Materials Science & Engineering C-Materials for Biological Applications 47 (2015) 180-188.

[67] F.B. Torstrick, N.T. Evans, H.Y. Stevens, K. Gall, R.E. Guldberg, Do Surface Porosity and Pore Size Influence Mechanical Properties and Cellular Response to PEEK?, Clin. Orthop. Relat. R. 474 (2016) 2373-2383.

[68] E.S. Place, N.D. Evans, M.M. Stevens, Complexity in biomaterials for tissue engineering, Nature materials 8(6) (2009) 457-70.

[69] A.L. DiRienzo, C.M. Yakacki, M. Frensemeier, A.S. Schneider, D.L. Safranski, A.J. Hoyt, C.P. Frick, Porous poly(para-phenylene) scaffolds for load-bearing orthopedic applications, Journal of the Mechanical Behavior of Biomedical Materials 30(0) (2014) 347-357.

[70] H.D. Pereira, V. Correlo, J. Silva-Correia, J. Oliveira, R. Reis Ceng, J. Espregueira-Mendes, Migration of "bioabsorbable" screws in ACL repair. How much do we know? A systematic review, Knee Surg Sports Traumatol Arthrosc (2013) 1-9.

[71] S.M. Kurtz, An Overview of PEEK Biomaterials, PEEK Biomaterials Handbook, William Andrew2011, pp. 1-8.

[72] Y. Arima, H. Iwata, Effect of wettability and surface functional groups on protein adsorption and cell adhesion using well-defined mixed self-assembled monolayers, Biomaterials 28(20) (2007) 3074-3082.

[73] D.F. Williams, A. McNamara, R.M. Turner, Potential of polyetheretherketone (PEEK) and carbon-fibre-reinforced PEEK in medical applications, J Mater Sci Lett 6(2) (1987) 188-190.

[74] S.W. Ha, M. Kirch, F. Birchler, K.L. Eckert, J. Mayer, E. Wintermantel, C. Sittig, I. Pfund-Klingenfuss, M. Textor, N.D. Spencer, M. Guecheva, H. Vonmont, Surface activation of polyetheretherketone (PEEK) and formation of calcium phosphate coatings by precipitation, Journal of Materials Science: Materials in Medicine 8(11) (1997) 683-690.

[75] A.H.C. Poulsson, R.G. Richards, Surface Modifications Techniques of Polyaryletheretherketone, Including Plasma Surface Treatment, PEEK Biomaterials Handbook, William Andrew2011, pp. 145-162.

[76] M.J. Shenton, G.C. Stevens, Surface modification of polymer surfaces: atmospheric plasma versus vacuum plasma treatments, Journal of Physics D: Applied Physics 34(18) (2001) 2761.

[77] A. Bakar, M. Cheng, S. Tang, S. Yu, K. Liao, C. Tan, K. Khor, P. Cheang, Tensile properties, tension–tension fatigue and biological response of polyetheretherketone–hydroxyapatite composites for load-bearing orthopedic implants, Biomaterials 24(13) (2003) 2245-2250.

[78] Marcus Jarman-Smith, Mark Brady, Steven M. Kurtz, N.M. Cordara, W.R. Walsh, Porosity in Polyaryletheretherketone, in: S.M. Kurtz (Ed.), PEEK Biomaterials Handbook, Elsevier Science2011, pp. 181-200.

[79] S.K. Sinclair, G.J. Konz, J.M. Dawson, R.T. Epperson, R.D. Bloebaum, Host bone response to polyetheretherketone versus porous tantalum implants for cervical spinal fusion in a goat model, Spine (Phila Pa 1976) 37(10) (2012) E571-80.

[80] U. Muller, T. Imwinkelried, M. Horst, M. Sievers, U. Graf-Hausner, Do human osteoblasts grow into open-porous titanium?, European cells & materials 11 (2006) 8-15.

[81] J. Zhou, H. Lin, T. Fang, X. Li, W. Dai, T. Uemura, J. Dong, The repair of large segmental bone defects in the rabbit with vascularized tissue engineered bone, Biomaterials 31(6) (2010) 1171-9.

[82] T. Hildebrand, A. Laib, R. Muller, J. Dequeker, P. Ruegsegger, Direct three-dimensional morphometric analysis of human cancellous bone: microstructural data from spine, femur, iliac crest, and calcaneus, J Bone Miner Res 14(7) (1999) 1167-74.

[83] A.S. Lin, T.H. Barrows, S.H. Cartmell, R.E. Guldberg, Microarchitectural and mechanical characterization of oriented porous polymer scaffolds, Biomaterials 24(3) (2003) 481-9.

[84] M.E. Oest, K.M. Dupont, H.J. Kong, D.J. Mooney, R.E. Guldberg, Quantitative assessment of scaffold and growth factor-mediated repair of critically sized bone defects, Journal of orthopaedic research : official publication of the Orthopaedic Research Society 25(7) (2007) 941-50.

[85] B. Rai, M.E. Oest, K.M. Dupont, K.H. Ho, S.H. Teoh, R.E. Guldberg, Combination of platelet-rich plasma with polycaprolactone-tricalcium phosphate scaffolds for segmental bone defect repair, Journal of biomedical materials research. Part A 81(4) (2007) 888-99.

[86] K.M. Dupont, K. Sharma, H.Y. Stevens, J.D. Boerckel, A.J. García, R.E. Guldberg, Human stem cell delivery for treatment of large segmental bone defects, Proceedings of the National Academy of Sciences 107(8) (2010) 3305-3310.

[87] A.M. Wojtowicz, A. Shekaran, M.E. Oest, K.M. Dupont, K.L. Templeman, D.W. Hutmacher, R.E. Guldberg, A.J. Garcia, Coating of biomaterial scaffolds with the collagen-mimetic peptide GFOGER for bone defect repair, Biomaterials 31(9) (2010) 2574-82.

[88] J. Van der Stok, O.P. Van der Jagt, S. Amin Yavari, M.F. De Haas, J.H. Waarsing, H. Jahr, E.M. Van Lieshout, P. Patka, J.A. Verhaar, A.A. Zadpoor, H. Weinans, Selective laser melting-produced porous titanium scaffolds regenerate bone in critical size cortical bone defects, J. Orthop. Res. 31(5) (2013) 792-9.

[89] R. Agarwal, C. González-García, B. Torstrick, R.E. Guldberg, M. Salmerón-Sánchez, A.J. García, Simple coating with fibronectin fragment enhances stainless steel screw osseointegration in healthy and osteoporotic rats, Biomaterials 63 (2015) 137-145.

[90] P. Tengvall, B. Skoglund, A. Askendal, P. Aspenberg, Surface immobilized bisphosphonate improves stainless-steel screw fixation in rats, Biomaterials 25(11) (2004) 2133-2138.

[91] Q. He, H.L. Chen, L. Huang, J.J. Dong, D.G. Guo, M.M. Mao, L. Kong, Y. Li, Z.X. Wu, W. Lei, Porous Surface Modified Bioactive Bone Cement for Enhanced Bone Bonding, PLoS One 7(8) (2012).

[92] S. Eshraghi, S. Das, Mechanical and microstructural properties of polycaprolactone scaffolds with one-dimensional, two-dimensional, and three-dimensional orthogonally oriented porous architectures produced by selective laser sintering, Acta Biomater 6(7) (2010) 2467-76.

[93] S.M. Kurtz, A Primer on UHMWPE, UHMWPE Biomaterials Handbook: Ultra High Molecular Weight Polyethylene in Total Joint Replacement and Medical Devices, Elsevier Science2009, pp. 1-6.

[94] D.A. Shimko, V.F. Shimko, E.A. Sander, K.F. Dickson, E.A. Nauman, Effect of porosity on the fluid flow characteristics and mechanical properties of tantalum scaffolds, Journal of Biomedical Materials Research Part B: Applied Biomaterials 73B(2) (2005) 315-324.

[95] J. Suwanprateeb, R. Chumnanklang, Three-dimensional printing of porous polyethylene structure using water-based binders, J Biomed Mater Res B Appl Biomater 78(1) (2006) 138-45.

[96] L. Wang, D.M. Yoon, P.P. Spicer, A.M. Henslee, D.W. Scott, M.E. Wong, F.K. Kasper, A.G. Mikos, Characterization of porous polymethylmethacrylate space maintainers for craniofacial reconstruction, J Biomed Mater Res B Appl Biomater 101(5) (2013) 813-25.

[97] L.D. Zardiackas, D.E. Parsell, L.D. Dillon, D.W. Mitchell, L.A. Nunnery, R. Poggie, Structure, metallurgy, and mechanical properties of a porous tantalum foam, Journal of Biomedical Materials Research 58(2) (2001) 180-187.

[98] E.J. Cheal, M. Spector, W.C. Hayes, Role of loads and prosthesis material properties on the mechanics of the proximal femur after total hip arthroplasty, Journal of orthopaedic research : official publication of the Orthopaedic Research Society 10(3) (1992) 405-22.

[99] J.D. Bobyn, R.M. Pilliar, H.U. Cameron, G.C. Weatherly, G.M. Kent, The effect of porous surface configuration on the tensile strength of fixation of implants by bone ingrowth, Clin. Orthop. Relat. Res. (149) (1980) 291-8.

[100] C. Yao, D. Storey, T.J. Webster, Nanostructured metal coatings on polymers increase osteoblast attachment, International journal of nanomedicine 2(3) (2007) 487-92.

[101] M.J. Dalby, N. Gadegaard, R. Tare, A. Andar, M.O. Riehle, P. Herzyk, C.D.W. Wilkinson, R.O.C. Oreffo, The control of human mesenchymal cell differentiation using nanoscale symmetry and disorder, Nature materials 6(12) (2007) 997-1003.

[102] U. Meyer, A. Buchter, H.P. Wiesmann, U. Joos, D.B. Jones, Basic reactions of osteoblasts on structured material surfaces, European cells & materials 9 (2005) 39-49.

[103] M.M. Shalabi, A. Gortemaker, M.A. Van't Hof, J.A. Jansen, N.H.J. Creugers, Implant surface roughness and bone healing: a systematic review, Journal of Dental Research 85(6) (2006) 496-500.

[104] S.A. Goldstein, The mechanical properties of trabecular bone: dependence on anatomic location and function, J. Biomech. 20(11-12) (1987) 1055-61.

[105] H.E. Götz, M. Müller, A. Emmel, U. Holzwarth, R.G. Erben, R. Stangl, Effect of surface finish on the osseointegration of laser-treated titanium alloy implants, Biomaterials 25(18) (2004) 4057-4064.

[106] R.E. Guldberg, M. Richards, N.J. Caldwell, C.L. Kuelske, S.A. Goldstein, Trabecular bone adaptation to variations in porous-coated implant topology, Journal of biomechanics 30(2) (1997) 147-53.

[107] R. Roeder, S. Smith, T. Conrad, N. Yanchak, C. Merrill, G. Converse, Porous and Bioactive PEEK Implants for Interbody Spinal Fusion, Advanced Materials and Processes 167(10) (2009) 46-48.

[108] K.H. Tan, C.K. Chua, K.F. Leong, M.W. Naing, C.M. Cheah, Fabrication and characterization of three-dimensional poly(ether- ether- ketone)/-hydroxyapatite biocomposite scaffolds using laser sintering, Proc. Inst. Mech. Eng. H 219(3) (2005) 183-94.

[109] J.M. Toth, M. Wang, B.T. Estes, J.L. Scifert, H.B. Seim, 3rd, A.S. Turner, Polyetheretherketone as a biomaterial for spinal applications, Biomaterials 27(3) (2006) 324-34.

[110] N.T. Evans, F.B. Torstrick, C.S. Lee, K.M. Dupont, D.L. Safranski, W.A. Chang, A.E. Macedo, A.S. Lin, J.M. Boothby, D.C. Whittingslow, R.A. Carson, R.E. Guldberg, K. Gall, High-strength, surface-porous polyether-ether-ketone for load-bearing orthopedic implants, Acta Biomater 13 (2015) 159-67.

[111] L.J. Gibson, M.F. Ashby, Cellular solids: structure and properties, Cambridge university press1999.

[112] E.M. Czekanska, M.J. Stoddart, J.R. Ralphs, R.G. Richards, J.S. Hayes, A phenotypic comparison of osteoblast cell lines versus human primary osteoblasts for biomaterials testing, J Biomed Mater Res A 102(8) (2014) 2636-43.

[113] S.-H. Wu, Y. Li, Y.-Q. Zhang, X.-K. Li, C.-F. Yuan, Y.-L. Hao, Z.-Y. Zhang, Z. Guo, Porous Titanium-6 Aluminum-4 Vanadium Cage Has Better Osseointegration and Less Micromotion Than a Poly-Ether-Ether-Ketone Cage in Sheep Vertebral Fusion, Artif. Organs 37(12) (2013) E191-E201.

[114] B.D. Boyan, T.W. Hummert, D.D. Dean, Z. Schwartz, Role of material surfaces in regulating bone and cartilage cell response, Biomaterials 17(2) (1996) 137-146.

[115] S.H. Oh, I.K. Park, J.M. Kim, J.H. Lee, In vitro and in vivo characteristics of PCL scaffolds with pore size gradient fabricated by a centrifugation method, Biomaterials 28(9) (2007) 1664-1671.

[116] M.C. Sobieraj, S.M. Kurtz, C.M. Rimnac, Notch sensitivity of PEEK in monotonic tension, Biomaterials 30(33) (2009) 6485-6494.

[117] M. Takano, L.E. Nielsen, The notch sensitivity of polymeric materials, Journal of Applied Polymer Science 20(8) (1976) 2193-2207.

[118] L.E. Nielsen, FATIGUE BEHAVIOR OF SOME FILLED POLYMERS, Bulletin of the American Physical Society 20(3) (1975) 481-481.

[119] J.A. Sauer, G.C. Richardson, Fatigue of polymers, Int J Fract 16(6) (1980) 499-532.

[120] S.H. Teoh, Fatigue of biomaterials: a review, International Journal of Fatigue 22(10) (2000) 825-837.

[121] S. Ishihara, A. McEvily, T. Goshima, K. Kanekasu, T. Nara, On fatigue lifetimes and fatigue crack growth behavior of bone cement, Journal of Materials Science: Materials in Medicine 11(10) (2000) 661-666.

[122] S.P. James, M. Jasty, J. Davies, H. Piehler, W.H. Harris, A fractographic investigation of PMMA bone cement focusing on the relationship between porosity reduction and increased fatigue life, J Biomed Mater Res 26(5) (1992) 651-62.

[123] A. Nachemson, Lumbar intradiscal pressure. Experimental studies on post-mortem material, Acta Orthop Scand Suppl 43 (1960) 1-104.

[124] A.B. Schultz, G.B. Andersson, Analysis of loads on the lumbar spine, Spine (Phila Pa 1976) 6(1) (1981) 76-82.

[125] H.J. Wilke, P. Neef, M. Caimi, T. Hoogland, L.E. Claes, New in vivo measurements of pressures in the intervertebral disc in daily life, Spine (Phila Pa 1976) 24(8) (1999) 755-62.

[126] J.B. Lian, G.S. Stein, Concepts of osteoblast growth and differentiation: basis for modulation of bone cell development and tissue formation, Crit. Rev. Oral Biol. Med. 3(3) (1992) 269-305.

[127] S.L. Ishaug-Riley, G.M. Crane-Kruger, M.J. Yaszemski, A.G. Mikos, Three-dimensional culture of rat calvarial osteoblasts in porous biodegradable polymers, Biomaterials 19(15) (1998) 1405-1412.

[128] Y.F. Zhou, V. Sae-Lim, A.M. Chou, D.W. Hutmacher, T.M. Lim, Does seeding density affect in vitro mineral nodules formation in novel composite scaffolds?, J Biomed Mater Res A 78(1) (2006) 183-93.

[129] S.H. Cartmell, B.D. Porter, A.J. Garcia, R.E. Guldberg, Effects of medium perfusion rate on cell-seeded three-dimensional bone constructs in vitro, Tissue Eng. 9(6) (2003) 1197-203.

[130] J. Dai, A.B. Rabie, VEGF: an essential mediator of both angiogenesis and endochondral ossification, J. Dent. Res. 86(10) (2007) 937-50.

[131] D.S. Steinbrech, B.J. Mehrara, P.B. Saadeh, J.A. Greenwald, J.A. Spector, G.K. Gittes, M.T. Longaker, VEGF expression in an osteoblast-like cell line is regulated by a hypoxia response mechanism, Am. J. Physiol. Cell Physiol. 278(4) (2000) C853-60.

[132] H. Mayer, H. Bertram, W. Lindenmaier, T. Korff, H. Weber, H. Weich, Vascular endothelial growth factor (VEGF-A) expression in human mesenchymal stem cells: autocrine and paracrine role on osteoblastic and endothelial differentiation, J. Cell. Biochem. 95(4) (2005) 827-39.

[133] T. Albrektsson, C. Johansson, Osteoinduction, osteoconduction and osseointegration, Eur. Spine J. 10 (2001) S96-S101.

[134] J.H. Lee, H.L. Jang, K.M. Lee, H.-R. Baek, K. Jin, J.H. Noh, Cold-spray coating of hydroxyapatite on a three-dimensional polyetheretherketone implant and its biocompatibility evaluated by in vitro and in vivo minipig model, Journal of Biomedical Materials Research Part B: Applied Biomaterials (2015) n/a-n/a.

[135] B.D. Boyan, L.F. Bonewald, E.P. Paschalis, C.H. Lohmann, J. Rosser, D.L. Cochran, D.D. Dean, Z. Schwartz, A.L. Boskey, Osteoblast-mediated mineral deposition in culture is dependent on surface microtopography, Calcif. Tissue Int. 71(6) (2002) 519-529.

[136] A. Cheng, A. Humayun, B.D. Boyan, Z. Schwartz, Enhanced Osteoblast Response to Porosity and Resolution of Additively Manufactured Ti-6Al-4V Constructs with Trabeculae-Inspired Porosity, 3D Printing and Additive Manufacturing 3(1) (2016) 10-21.

[137] L.M.R.d. Vasconcellos, D.O. Leite, F.N.d. Oliveira, Y.R. Carvalho, C.A.A. Cairo, Evaluation of bone ingrowth into porous titanium implant: histomorphometric analysis in rabbits, Brazilian Oral Research 24 (2010) 399-405.

[138] A. Wennerberg, T. Albrektsson, B. Andersson, J.J. Krol, A HISTOMORPHOMETRIC AND REMOVAL TORQUE STUDY OF SCREW-SHAPED TITANIUM IMPLANTS WITH 3 DIFFERENT SURFACE TOPOGRAPHIES, Clin. Oral Implants Res. 6(1) (1995) 24-30.

[139] J. Khoury, M. Maxwell, R.E. Cherian, J. Bachand, A.C. Kurz, M. Walsh, M. Assad, R.C. Svrluga, Enhanced bioactivity and osseointegration of PEEK with accelerated neutral atom beam technology, J Biomed Mater Res B Appl Biomater (2015).

[140] R. Olivares-Navarrete, S.E. Rodil, S.L. Hyzy, G.R. Dunn, A. Almaguer-Flores, Z. Schwartz, B.D. Boyan, Role of integrin subunits in mesenchymal stem cell differentiation and osteoblast maturation on graphitic carbon-coated microstructured surfaces, Biomaterials 51 (2015) 69-79.

[141] M. Franchi, B. Bacchelli, D. Martini, V.D. Pasquale, E. Orsini, V. Ottani, M. Fini, G. Giavaresi, R. Giardino, A. Ruggeri, Early detachment of titanium particles from various different surfaces of endosseous dental implants, Biomaterials 25(12) (2004) 2239-46.

[142] S. Vercaigne, J.G. Wolke, I. Naert, J.A. Jansen, Histomorphometrical and mechanical evaluation of titanium plasma-spray-coated implants placed in the cortical bone of goats, J Biomed Mater Res 41(1) (1998) 41-8.

[143] A. Kienle, N. Graf, H.-J. Wilke, Does impaction of titanium-coated interbody fusion cages into the disc space cause wear debris or delamination?, The Spine Journal 16(2) (2016) 235-242.

[144] R. Roybal, Subtractive versus Additive Manufacturing of Spinal Implants, 11th Annual Castellvi Spine Meeting, Duck Key, FL, 2016.

[145] F.B. Torstrick, B.S. Klosterhoff, L.E. Westerlund, K.T. Foley, J. Gochuico, C.S.D. Lee, K. Gall, D.L. Safranski, Impaction durability of porous PEEK and titanium-coated PEEK interbody fusion devices, (Under Review).

[146] F.B. Torstrick, D.L. Safranski, J.K. Burkus, J.L. Chappuis, R.E. Guldberg, K.E. Smith, Getting PEEK to Stick to Bone: The Development of Porous PEEK for Interbody Fusion Devices, Tech. Orthop. 32(3) (2017) 158-166.

[147] P.L. Leong, E.F. Morgan, Correlations between indentation modulus and mineral density in bone-fracture calluses, Integrative and Comparative Biology 49(1) (2009) 59-68.

[148] E.F. Morgan, Z.D. Mason, K.B. Chien, A.J. Pfeiffer, G.L. Barnes, T.A. Einhorn, L.C. Gerstenfeld, Micro-computed tomography assessment of fracture healing: relationships among callus structure, composition, and mechanical function, Bone 44(2) (2009) 335-44.

[149] D. Vogel, H. Dempwolf, A. Baumann, R. Bader, Characterization of thick titanium plasma spray coatings on PEEK materials used for medical implants and the influence on the mechanical properties, Journal of the Mechanical Behavior of Biomedical Materials (2017).

[150] L.F. Cooper, T. Masuda, S.W. Whitson, P. Yliheikkilä, D.A. Felton, Formation of mineralizing osteoblast cultures on machined, titanium oxide grit-blasted, and plasma-sprayed titanium surfaces, International Journal of Oral & Maxillofacial Implants 14(1) (1999).

[151] D. De Santis, C. Guerriero, P.F. Nocini, A. Ungersbock, G. Richards, P. Gotte, U. Armato, Adult human bone cells from jaw bones cultured on plasma-sprayed or polished surfaces of titanium or hydroxylapatite discs, Journal of Materials Science: Materials in Medicine 7(1) (1996) 21-28.

[152] B.G. Keselowsky, L. Wang, Z. Schwartz, A.J. Garcia, B.D. Boyan, Integrin alpha(5) controls osteoblastic proliferation and differentiation responses to titanium substrates presenting different roughness characteristics in a roughness independent manner, Journal of Biomedical Materials Research Part A 80A(3) (2007) 700-710.

[153] A. Cheng, A. Humayun, D.J. Cohen, B.D. Boyan, Z. Schwartz, Additively manufactured 3D porous Ti-6Al-4V constructs mimic trabecular bone structure and regulate osteoblast proliferation, differentiation and local factor production in a porosity and surface roughness dependent manner, Biofabrication 6(4) (2014) 045007.

[154] K.A. Kilian, B. Bugarija, B.T. Lahn, M. Mrksich, Geometric cues for directing the differentiation of mesenchymal stem cells, Proceedings of the National Academy of Sciences 107(11) (2010) 4872-4877.

[155] M. Werner, S.B.G. Blanquer, S.P. Haimi, G. Korus, J.W.C. Dunlop, G.N. Duda, D.W. Grijpma, A. Petersen, Surface Curvature Differentially Regulates Stem Cell Migration and Differentiation via Altered Attachment Morphology and Nuclear Deformation, Advanced Science 4(2) (2017) 1600347-n/a.

[156] A.J. Clemow, A.M. Weinstein, J.J. Klawitter, J. Koeneman, J. Anderson, Interface mechanics of porous titanium implants, J. Biomed. Mater. Res. 15(1) (1981) 73-82.

[157] J.L. Nilles, J.M. Coletti, C. Wilson, Biomechanical evaluation of bone-porous material interfaces, J. Biomed. Mater. Res. 7(2) (1973) 231-251.

[158] C.A. Engh, J. Bobyn, A.H. Glassman, Porous-coated hip replacement. The factors governing bone ingrowth, stress shielding, and clinical results, Bone & Joint Journal 69(1) (1987) 45-55.

[159] M. Assad, P. Jarzem, M.A. Leroux, C. Coillard, A.V. Chernyshov, S. Charette, C.H. Rivard, Porous titanium-nickel for intervertebral fusion in a sheep model: part 1. Histomorphometric and radiological analysis, J Biomed Mater Res B Appl Biomater 64(2) (2003) 107-20.

[160] M.C. Anderson, R. Olsen, Bone ingrowth into porous silicon nitride, Journal of Biomedical Materials Research Part A 92A(4) (2010) 1598-1605.

[161] H. Ahn, R. Patel, A. Hoyt, A. Lin, F. Torstrick, R. Guldberg, C. Frick, R. Carpenter, C. Yakacki, N. Willett, Biological and Mechanical Evaluation of Porous poly(para-phenylene) for Orthopaedic Implants, Presented at TERMIS-AM Annual Meeting, Charlotte, NC, USA, 2017.

[162] M. Spector, M.J. Michno, W.H. Smarook, G.T. Kwiatkowski, High-Modulus Polymer for Porous Orthopedic Implants - Biomechanical Compatibility of Porous Implants, J. Biomed. Mater. Res. 12(5) (1978) 665-677.

[163] M. Spector, W.R. Flemming, A. Kreutner, B.W. Sauer, Bone-Growth into Porous High-Density Polyethylene, J. Biomed. Mater. Res. 10(4) (1976) 595-603.

[164] M. Spector, S.L. Harmon, A. Kreutner, Characteristics of tissue growth into Proplast and porous polyethylene implants in bone, J. Biomed. Mater. Res. 13(5) (1979) 677-92.

[165] C.M. Yakacki, J. Griffis, M. Poukalova, K. Gall, Bearing area: A new indication for suture anchor pullout strength?, Journal of Orthopaedic Research 27(8) (2009) 1048-1054.

[166] R. Skripitz, P. Aspenberg, Tensile bond between bone and titanium: a reappraisal of osseointegration, Acta Orthop Scand 69(3) (1998) 315-9.

[167] J.E. Davies, Bone bonding at natural and biomaterial surfaces, Biomaterials 28(34) (2007) 5058-67.

[168] J.E. Davies, Mechanisms of endosseous integration, Int. J. Prosthodont. 11(5) (1998) 391-401.

[169] R. Müller, H. Van Campenhout, B. Van Damme, G. Van der Perre, J. Dequeker, T. Hildebrand, P. Rüegsegger, Morphometric Analysis of Human Bone Biopsies: A Quantitative Structural Comparison of Histological Sections and Micro-Computed Tomography, Bone 23(1) (1998) 59-66.

[170] J.S. Thomsen, A. Laib, B. Koller, S. Prohaska, L.I. Mosekilde, W. Gowin, Stereological measures of trabecular bone structure: comparison of 3D micro computed tomography with 2D histological sections in human proximal tibial bone biopsies, Journal of Microscopy 218(2) (2005) 171-179.

[171] S.A. Hacking, M. Tanzer, E.J. Harvey, J.J. Krygier, J.D. Bobyn, Relative contributions of chemistry and topography to the osseointegration of hydroxyapatite coatings, Clinical orthopaedics and related research (405) (2002) 24-38.

[172] S. Choi, X. Yu, L. Jongpaiboonkit, S.J. Hollister, W.L. Murphy, Inorganic coatings for optimized non-viral transfection of stem cells, Scientific Reports 3 (2013) 1567.

[173] F. Hilbrig, R. Freitag, Isolation and purification of recombinant proteins, antibodies and plasmid DNA with hydroxyapatite chromatography, Biotechnology Journal 7(1) (2012) 90-102.

[174] A. Cheng, D.J. Cohen, A. Kahn, R.M. Clohessy, K. Sahingur, J.B. Newton, S.L. Hyzy, B.D. Boyan, Z. Schwartz, Laser Sintered Porous Ti-6Al-4V Implants Stimulate Vertical Bone Growth, Ann. Biomed. Eng. (2017).

[175] R.D. Guyer, J.J. Abitbol, D.D. Ohnmeiss, C. Yao, Evaluating Osseointegration Into a Deeply Porous Titanium Scaffold: A Biomechanical Comparison With PEEK and Allograft, Spine (Phila Pa 1976) 41(19) (2016) E1146-50.

[176] Z. Schwartz, P. Raz, G. Zhao, Y. Barak, M. Tauber, H. Yao, B.D. Boyan, Effect of Micrometer-Scale Roughness of the Surface of Ti6Al4V Pedicle Screws in Vitro and in Vivo, Journal of Bone and Joint Surgery-American Volume 90A(11) (2008) 2485-2498.

[177] F.P. Koch, D. Weng, S. Krämer, S. Biesterfeld, A. Jahn-Eimermacher, W. Wagner, Osseointegration of one-piece zirconia implants compared with a titanium implant of

identical design: a histomorphometric study in the dog, Clin. Oral Implants Res. 21(3) (2010) 350-356.

[178] R. Olivares-Navarrete, R.A. Gittens, J.M. Schneider, S.L. Hyzy, D.A. Haithcock, P.F. Ullrich, Z. Schwartz, B.D. Boyan, Osteoblasts exhibit a more differentiated phenotype and increased bone morphogenetic protein production on titanium alloy substrates than on poly-ether-ether-ketone, Spine Journal 12(3) (2012) 265-272.

[179] K.B. Sagomonyants, M.L. Jarman-Smith, J.N. Devine, M.S. Aronow, G.A. Gronowicz, The in vitro response of human osteoblasts to polyetheretherketone (PEEK) substrates compared to commercially pure titanium, Biomaterials 29(11) (2008) 1563-72.

[180] Y. Deng, X. Liu, A. Xu, L. Wang, Z. Luo, Y. Zheng, F. Deng, J. Wei, Z. Tang, S. Wei, Effect of surface roughness on osteogenesis in vitro and osseointegration in vivo of carbon fiber-reinforced polyetheretherketone-nanohydroxyapatite composite, Int J Nanomedicine 10 (2015) 1425-47.

[181] J.W. Durham, 3rd, M.J. Allen, A. Rabiei, Preparation, characterization and in vitro response of bioactive coatings on polyether ether ketone, J Biomed Mater Res B Appl Biomater (2015).

[182] P.L.J. Gunter, O.L.J. Gijzeman, J.W. Niemantsverdriet, Surface roughness effects in quantitative XPS: magic angle for determining overlayer thickness, Applied Surface Science 115(4) (1997) 342-346.

[183] C.J. Powell, A. Jablonski, Progress in quantitative surface analysis by X-ray photoelectron spectroscopy: Current status and perspectives, Journal of Electron Spectroscopy and Related Phenomena 178 (2010) 331-346.

[184] K.U. Lewandrowski, D.D. Hile, B.M. Thompson, D.L. Wise, W.W. Tomford, D.J. Trantolo, Quantitative measures of osteoinductivity of a porous poly(propylene fumarate) bone graft extender, Tissue engineering 9(1) (2003) 85-93.

[185] U. Diebold, T.E. Madey, TiO2 by XPS, Surface Science Spectra 4(3) (1996) 227-231.

[186] C. Aparicio, J.M. Manero, F. Conde, M. Pegueroles, J.A. Planell, M. Vallet-Regí, F.J. Gil, Acceleration of apatite nucleation on microrough bioactive titanium for bone-replacing implants, Journal of Biomedical Materials Research Part A 82A(3) (2007) 521-529.

[187] Y. Haba, T. Lindner, A. Fritsche, A.-K. Schiebenhöfer, R. Souffrant, D. Kluess, R. Skripitz, W. Mittelmeier, R. Bader, Relationship Between Mechanical Properties and Bone Mineral Density of Human Femoral Bone Retrieved from Patients with Osteoarthritis, The Open Orthopaedics Journal 6 (2012) 458-463.

[188] A.C. Jones, C.H. Arns, A.P. Sheppard, D.W. Hutmacher, B.K. Milthorpe, M.A. Knackstedt, Assessment of bone ingrowth into porous biomaterials using MICRO-CT, Biomaterials 28(15) (2007) 2491-2504.

[189] E. Tsuruga, H. Takita, H. Itoh, Y. Wakisaka, Y. Kuboki, Pore Size of Porous Hydroxyapatite as the Cell-Substratum Controls BMP-Induced Osteogenesis, J. Biochem. 121(2) (1997) 317-324.

[190] S. Yu, K.P. Hariram, R. Kumar, P. Cheang, K.K. Aik, In vitro apatite formation and its growth kinetics on hydroxyapatite/polyetheretherketone biocomposites, Biomaterials 26(15) (2005) 2343-2352.

[191] A. Hieda, N. Uemura, Y. Hashimoto, I. Toda, S. Baba, In vivo bioactivity of porous polyetheretherketone with a foamed surface, Dental Materials Journal 36(2) (2017) 222-229.

[192] W. Walsh, M.H. Pelletier, S. Boden, 119 - Novel Titanium Surface Improves the Osteogenic Response of PEEK Implants in a Sheep Model, The Spine Journal 17(10, Supplement) (2017) S108-S109.

[193] H.J. Busscher, A.W.J. van Pelt, P. de Boer, H.P. de Jong, J. Arends, The effect of surface roughening of polymers on measured contact angles of liquids, Colloids and Surfaces 9(4) (1984) 319-331.

[194] H. Schonhorn, Heterogeneous Nucleation of Polymer Melts on High-Energy Surfaces. II. Effect of Substrate on Morphology and Wettability, Macromolecules 1(2) (1968) 145-151.

[195] J.R. Woodard, A.J. Hilldore, S.K. Lan, C.J. Park, A.W. Morgan, J.A.C. Eurell, S.G. Clark, M.B. Wheeler, R.D. Jamison, A.J. Wagoner Johnson, The mechanical properties and osteoconductivity of hydroxyapatite bone scaffolds with multi-scale porosity, Biomaterials 28(1) (2007) 45-54.

[196] A.G. Mitsak, J.M. Kemppainen, M.T. Harris, S.J. Hollister, Effect of Polycaprolactone Scaffold Permeability on Bone Regeneration In Vivo, Tissue Engineering. Part A 17(13-14) (2011) 1831-1839.

[197] S.J. Hollister, Porous scaffold design for tissue engineering, Nat Mater 4(7) (2005) 518-524.

[198] M.A. Lan, C.A. Gersbach, K.E. Michael, B.G. Keselowsky, A.J. García, Myoblast proliferation and differentiation on fibronectin-coated self assembled monolayers presenting different surface chemistries, Biomaterials 26(22) (2005) 4523-4531.

[199] A. Ulman, Formation and structure of self-assembled monolayers, Chemical reviews 96(4) (1996) 1533-1554.

[200] D. Suárez-González, K. Barnhart, F. Migneco, C. Flanagan, S.J. Hollister, W.L. Murphy, Controllable mineral coatings on PCL scaffolds as carriers for growth factor release, Biomaterials 33(2) (2012) 713-721.

[201] E. Saito, D. Suarez-Gonzalez, W.L. Murphy, S.J. Hollister, Biomineral coating increases bone formation by ex vivo BMP-7 gene therapy in rapid prototyped poly(L-lactic acid) (PLLA) and poly(epsilon-caprolactone) (PCL) porous scaffolds, Adv Healthc Mater 4(4) (2015) 621-32.

[202] W.L. Murphy, D.J. Mooney, Bioinspired growth of crystalline carbonate apatite on biodegradable polymer substrata, Journal of the American Chemical Society 124(9) (2002) 1910-1917.

[203] J. van der Stok, M.K. Koolen, M.P. de Maat, S.A. Yavari, J. Alblas, P. Patka, J.A. Verhaar, E.M. van Lieshout, A.A. Zadpoor, H. Weinans, H. Jahr, Full regeneration of segmental bone defects using porous titanium implants loaded with BMP-2 containing fibrin gels, Eur Cell Mater 29 (2015) 141-53; discussion 153-4.

[204] J.E. Davies, Understanding peri-implant endosseous healing, Journal of dental education 67(8) (2003) 932-49.

[205] S. Franz, S. Rammelt, D. Scharnweber, J.C. Simon, Immune responses to implants - a review of the implications for the design of immunomodulatory biomaterials, Biomaterials 32(28) (2011) 6692-709.

[206] L. Tang, J.W. Eaton, Inflammatory responses to biomaterials, Am. J. Clin. Pathol. 103(4) (1995) 466-71.

[207] W.-J. Hu, J.W. Eaton, T.P. Ugarova, L. Tang, Molecular basis of biomaterial-mediated foreign body reactions, Blood 98(4) (2001) 1231-1238.

[208] Z. Chen, T. Klein, R.Z. Murray, R. Crawford, J. Chang, C. Wu, Y. Xiao, Osteoimmunomodulation for the development of advanced bone biomaterials, Materials Today 19(6) (2016) 304-321.

[209] M.K. Chang, L.-J. Raggatt, K.A. Alexander, J.S. Kuliwaba, N.L. Fazzalari, K. Schroder, E.R. Maylin, V.M. Ripoll, D.A. Hume, A.R. Pettit, Osteal Tissue Macrophages Are Intercalated throughout Human and Mouse Bone Lining Tissues and Regulate Osteoblast Function In Vitro and In Vivo, The Journal of Immunology 181(2) (2008) 1232-1244.

[210] R. Olivares-Navarrete, S.L. Hyzy, P.J. Slosar, J.M. Schneider, Z. Schwartz, B.D. Boyan, Implant Materials Generate Different Peri-implant Inflammatory Factors, Spine (Phila Pa 1976) 40(6) (2015) 399-404.

[211] G. Vallés, F. Bensiamar, L. Crespo, M. Arruebo, N. Vilaboa, L. Saldaña, Topographical cues regulate the crosstalk between MSCs and macrophages, Biomaterials 37(Supplement C) (2015) 124-133.

[212] K. Garg, N.A. Pullen, C.A. Oskeritzian, J.J. Ryan, G.L. Bowlin, Macrophage functional polarization (M1/M2) in response to varying fiber and pore dimensions of electrospun scaffolds, Biomaterials 34(18) (2013) 4439-4451.

[213] U. Klinge, B. Klosterhalfen, V. Birkenhauer, K. Junge, J. Conze, V. Schumpelick, Impact of Polymer Pore Size on the Interface Scar Formation in a Rat Model, Journal of Surgical Research 103(2) (2002) 208-214.

[214] D. Weyhe, I. Schmitz, O. Belyaev, R. Grabs, K.-M. Müller, W. Uhl, V. Zumtobel, Experimental Comparison of Monofile Light and Heavy Polypropylene Meshes: Less Weight Does Not Mean Less Biological Response, World Journal of Surgery 30(8) (2006) 1586-1591.